Photon emitters in hexagonal boron nitride: creating, enhancing, and controlling optically active colour centres

Reza Hekmati

School of Physics and Astronomy

Thesis submitted to Cardiff University
for the degree of Doctor of Philosophy

March 2023

Supervisors:
Prof. Anthony Bennett
Prof. Stephen Lynch

Summary

In this thesis, I study photon emitters in hexagonal boron nitride (hBN) to create and control optically active colour centres. In addition, enhancing the coupling efficiency of a quantum emitter into an objective lens is studied.

I present a step–by–step method for designing a bullseye Bragg grating structure to enhance the collection efficiency and increase the Purcell factor. In my design, I explore the coupling condition between the dipole and the cavity and show that the collection efficiency remains high because of exploiting a gold layer as a reflector layer. I calculate the coupling efficiency between the dipole and the cavity. I apply apodization to the grating in the bullseye structure to achieve higher collection efficiency.

I investigate different approaches, including treatment, local strain using nanostubs, annealing and ion irradiation to generate defect centres in hBN. I use a combination of strain and plasma/annealing treatment to generate reproducible defect centres in hBN. I discovered that consecutive annealings at medium temperature on a single flake could create ensembles of defects, while single annealing at high temperatures could create narrower linewidth defects, that some of them showed power saturation behaviours. I investigate fluence and ion energy for Kr^+ irradiated sample. My studies show that the fluence of 10^{12} cm^{-2} with an ion energy of 150–200 eV can create single defect–like emitters. Subsequent annealing on these samples showed one sign of a narrow linewidth emitter in the highest energy sample.

Moreover, we investigate the electron spin properties of V_B^- centres in ensembles of defects in a C–implanted hBN sample. We report that the dephasing time of the Rabi oscillation and Ramsey interferometry at 90 mT are around 30 and 3 ns, respectively. We apply the spin–echo sequence to the V_B^- centres and achieve a spin–echo coherence time of 100 ns at 90 mT.

Contents

List of Tables

List of Figures

Acronyms

2D two–dimensional.

3D three–dimensional.

AFM atomic force microscope.

AOM acousto–optic modulators.

APD avalanche photodiodes.

AWG arbitrary waveform generator.

CCD charge–coupled device.

CPW co–planar waveguide.

CVD chemical vapor deposition.

CW continuous wave.

DAQ data acquisition.

EPR electron paramagnetic resonance.

ES excited state.

FDTD finite–difference time–domain.

FFT fast Fourier transform.

FWHM full width at half maximum.

GS ground state.

GSLAC ground state level anti–crossing.

hBN hexagonal boron nitride.

HBT Hanbury Brown and Twiss.

HFI hyperfine interaction.

IRF instrument response function.

ISC intersystem crossing.

LLG Landau–Lifshitz–Gilbert.

MBE molecular–beam epitaxy.

MOVPE metal–organic vapour–phase epitaxy.

MW microwave.

NA numerical aperture.

ODMR optically detected magnetic resonance.

PL photoluminescence.

PML perfectly matched layer.

PSB phonon sideband.

QD quantum dot.

RIE reactive ion etching.

RTA rapid thermal annealer.

sccm standard cubic centimetres per minute.

SD standard deviation.

SEM scanning electron microscope.

SiC silicon carbide.

TE transverse electric.

UV ultra–violet.

WS_2 Tungsten disulfide.

WSe_2 Tungsten diselenide.

ZFS zero field splitting.

ZPL zero–phonon line.

CHAPTER 1

Introduction

Point defects in wide bandgap semiconductors are emerging fields with potential applications in quantum computing and information. Hexagonal boron nitride with the single–photon emission typically includes a sharp zero–phonon line with a phonon sideband red–shifted by 165 meV is among these room–temperature defects. In this work, I concentrate on generating defect centres and enhancing their emission by coupling them to the cavity structure. Finally, I control optically addressable spin states in one of the recently found defects in hBN. The outline of this thesis is as follows:

Chapter 2 introduces the bullseye Bragg grating cavity used for two–dimensional (2D) materials. Next, it discussed different approaches to generating defect centres in hBN, including plasma treatment, thermal annealing, strain and ion irradiation. Finally, it highlights recent discoveries of optically addressable spin defects in this material.

Chapter 3 describes the experimental techniques, such as second–order correlation function, spin manipulation setups, and cleanroom recipes to generate defect centres. In addition, numerical methods to simulate the bullseye Bragg grating structure are explained in this chapter.

Chapter 4 focuses on the bullseye Bragg grating structure and presents a methodical approach to increasing the Purcell factor and collection efficiency from a surface–mounted emitter. Next, imperfections in design and coupling are discussed. In addition, the brightness enhancement of the emitter coupled to the cavity under ideal coupling conditions is studied. Finally, coupling directly to a single–mode fibre is investigated for an apodized grating.

Chapter 5 aims to explore different methods to generate defect centres in hBN. It focuses on plasma treatment, nitrogen annealing and strain–induced methods. Moreover, ion irradiation using Kr^+ is presented to create vacancy centres in the crystal.

Chapter 6 is dedicated to spin properties of negatively charged boron vacancy in hBN. It includes Rabi oscillation, spin dephasing time, spin relaxation time, and spin coherence time.

Finally, the conclusions of each technical chapter, followed up with their future work, are presented in chapter 7.

CHAPTER 2

Literature

Nature is probabilistic, and this feature makes it unpredictable. Richard Feynman, in his 1982's article, "Simulating Physics with Computers", proposed the possibility of a computer that works in the same way as nature does. Even though the output of such a computer is not a unique function of the input, repeating the observation (experiment) over and over will give the frequency of a given outcome (final state) proportional to the number of times with approximately the same rate as it happens in nature [1]. To solve questions in such a probabilistic environment, quantum physics proposes the quantum computer; this platform relies on quantum bit (qubit), representing the basis states of 0 and 1 and the superposition of these basis states. This superposition is also a possible quantum state, which leads to exciting consequences when considering multiple qubits. To be precise, a quantum state is defined in a complex space named *Hilbert* space. One aspect of Hilbert space is that for n qubits, it has a dimension of 2^n; for example, 64 qubits represent 18.4×10^{18} possibilities [2].

To realise quantum computation[1], DiVincenzo proposed a set of essential benchmarks [3]:

1. A scalable physical system with well–characterised qubits.
2. The ability to initialise the qubits to a simple standard state.
3. Long relevant decoherence times, much longer than the gate operation time.
4. A universal set of quantum gates.
5. A qubit–specific measurement capability.
6. The ability to interconvert stationary and flying qubits.
7. The ability faithfully to transmit flying qubits between specified locations.

For a platform that meets all the above mentioned benchmarks, at least two types of qubits are needed:

- **local[2] qubits**: They are building blocks of quantum nodes that perform quantum operations [4]. These operations include the state's initialisation, manipulation, and readout, accompanied by the quantum nodes' capability to store

[1] These criteria are specific to a quantum computer. QKD, imaging and sensing do not need most of these.

[2] static, stationary, standing

the state's coherence properties. Among different candidates to realise local qubits as quantum nodes, trapped ions, neutral atoms, rare–earth ions, quantum dots (through excitons, charges and spin), and colour centres (spin defects) are worth mentioning [5, 6]. Even though the optical loss in commercial fibre is $\simeq 0.2\,\mathrm{dB\,km^{-1}}$ at 1550 nm, there is no cut–off for transmission distance [7]; however, for applications such as Quantum Key Distribution, the approximate upper bound for transmission is around 100 km [8]. It is shown for a trapped ion platform (single $^{40}Ca^{+}$), the optical fibre loss at 854 nm is approximately $3\,\mathrm{dB\,km^{-1}}$, which results in 10^{-15} transmission loss; however, converting the operating frequency to telecommunication wavelength would result in 10.4% transmission probability [9]. For the case of the nitrogen–vacancy centre in diamond, the optical fibre loss is around $8\,\mathrm{dB\,km^{-1}}$ at 637 nm, but frequency conversion allows the operation to reach 1.3 km [10, 11]. The coherence time for the abovementioned trapped ion example can reach 2 s at cryogenic temperature, whereas for the diamond, the coherence time is around a few microseconds [12]. The coherence properties of some of these candidates are discussed in Section 2.2. Until now, none of these candidates could satisfy all the above mentioned criteria.

- **flying qubits**: They transport quantum information between the distant quantum nodes [4]. Photon states are good examples of the flying qubit in which the qubit is encoded in the photon's polarisation, frequency, phase or spatial wavefunction [3, 13]. Owing to photons' well–controlled quantum states, negligible photon–photon interaction and low decoherence, low loss transmission through fibre channels at telecommunication wavelengths and high travelling speed, they are a beneficial courier over long distances for quantum information [14]. In addition, photons from separate systems can be transported to a common location to perform entanglement [15]. Antibunched single photon emission and entangled photon–pair generation are the different realisations of photons as flying qubits [16–18]; however, for short–distance applications, it is suggested that the spin of an electron might also serve as a movable qubit [3, 19].

Following the above mentioned discussion, photons should meet some criteria, known as ideal single photon characteristics, to be considered flying qubits. Some of these criteria are [20]:

- **Ability to make a single photon**: The probability of multi–photon emission should be 0 %. This criterion can be characterised by the second-order intensity correlation function ($g^{(2)}(0)$). An ideal single photon source with no

more than one photon leads to $g^{(2)}(0) = 0$. This function is defined as [21]:

$$g^{(2)}(0) = \frac{\langle n_1(t)\, n_2(t)\rangle_t}{\langle n_1(t)\rangle_t \langle n_2(t)\rangle_t} \tag{2.1}$$

where $n_i(t)$ is the number of counts (n) detected at time t. This function will be discussed in detail in Section 3.2.

- **Deterministic**: The probability of generating one photon in a single mode fibre at a given clock time with deterministic photon's degrees of freedom (wavelength, polarisation, spectral mode). This requires a highly efficient source.

- **On–demand**: This means the probability of single photon emission at fixed and arbitrary times defined by the user should be 100 %. For this reason, the probability of a photon emitting at the desired time is crucial.

- **Brightness**: The brightness can be broken down into the quantum efficiency of emitting a photon in the excited state[3] (η_{QE}) and the collection efficiency (η_{lens}). The collection efficiency is the efficiency of collecting the emitted photon in a single mode fibre from the photon source. Besides, the spontaneous emission rate of the target optical mode can be enhanced using cavity structures. This probability is defined as $\beta = \Gamma_{mode}/(\Gamma_{mode} + \Gamma_{other})$, in which Γ_{mode} and Γ_{others} are emission rates into the target and all other modes, respectively. Therefore, the brightness at the first lens is [21]:

$$B_{lens} = \beta\, \eta_{lens}\, p_{state}\, \eta_{QE} \tag{2.2}$$

where p_{state} describes the probability that the quantum system is initialised in a well–defined state. In addition, the excitation efficiency (η_{exc}) is another critical parameter. This is defined as the absorption cross–section of the emitter in which the photon's spectral, mode and polarisation[4] play a crucial role [22, 23].

- **Indistinguishability**: It means the indistinguishability of two single photons from separate sources or from the same source at different times; in other words, the purity of the photons in various degrees of freedom (spectrum, time, polarisation, and space). The overlap between photon wavepackets can be measured by M in Equation (2.4), where T and R are beamsplitter intensity

[3] losses due to non–radiate decay
[4] with respect to the emitter's dipole

transmission and reflectivity coefficients, respectively [21].

$$V_{HOM} = (C_{\perp} - C_{\parallel})/C_{\perp} \tag{2.3}$$

$$M = V_{HOM}((R^2 + T^2)/2RT) \tag{2.4}$$

$$T = 1 - R \tag{2.5}$$

In the above equations, V_{HOM} quantifies the interference visibility measured via Hong–Ou–Mandel experiment. C indicates the coincidence count measured between two detectors located at two outputs. The coincidence count can be maximised ($C_{\perp}$) or minimised ($C_{\parallel}$) by varying the degree of freedom (for instance, polarisation).

- **Fidelity to a fixed qubit in a node**: It measures an experimentally determined state compared to some ideal state. This could be comparing a single photon to an ideal photon or a real entangled (pair) state to a Bell pair. The fidelity of a single photon state might compare the number distribution of photons, i.e. probability of getting one photon number with an ideal $N = 1$ Fock state. However, it is unclear if this definition includes the overlap in frequency, mode, linewidth, etc. Fidelity to a certain Bell state (i.e. HH + VV) is probably only compared to the fidelity on the polarisation basis. It does not tell us about the fidelity in other degrees of freedom, such as photon number, mode, etc.

So far, different benchmarks and criteria for realising quantum computing and information have been introduced. In the last decades, researchers have used these checklists to explore various options in different material systems. Due to their well–isolated electronic states, platforms like neutral atoms and ion traps are among suitable candidates to achieve the above mentioned checklists; however, they are not the only systems that offer well–isolated two–level electronic states. Defect centres in the wide bandgap materials offer a vast range of characteristics that make them a suitable candidate for future quantum computing and quantum communications, including [24]:

- A wide band gap to accommodate highly localised electronic bound states confined to a region on the scale of a single lattice site limits the interference from the other electronic states. It also hosts transitions with strong dipolar interaction with light.

- Paramagnetic and long–lived states with the capability to be optically addressed and manipulated with radio frequency.

- The qubit states can be polarised with an optical pumping cycle involving spin–selective excitation and decay.
- Fourier–transform–limited emission in which they emit photons in a single spectral–temporal mode without drift of the central frequency.
- Host spin bath including naturally occurring isotopes with zero nuclear spins.
- High–quality crystal to avoid imperfections and impurities that could affect spin states.
- Operating at room temperature.

Spin in these defect centres is of particular interest due to the potential of realising quantum entanglement between a confined spin and a propagating photon [25]. However, the coherence of a quantum state prepared by the local qubits can limit the distance in which the flying qubits can interact. In addition, the losses in the transmission channel can be an extra limiting factor. Therefore, the conversion between the local qubit and flying qubit is necessary for maintaining or improving quantum information [26]. In scenarios where the local qubit is encoded in the spin, and the flying qubit is encoded in a photon's degree of freedom, the spin–photon interface will be responsible for the conversion to mediate the interaction between the spin and photon [27]. These interfaces form the basis of essential functions, including sending, receiving, transferring, swapping, and entangling qubits at quantum nodes. To fulfil these capabilities, in addition to spin (local qubit) and photon (flying qubit), photonic structures are needed to facilitate their interactions; the earlier prototype of such a structure includes a cavity and a waveguide [28]. A strong coupling between local qubits and cavity is necessary for deterministic photon emission [29]. A suitable platform for a quantum node should fulfil the following requirements for scalable quantum computation and communications (i.e. quantum network[5]) [30]:

- ☐ The node should be capable of interfacing at least one local qubit with flying qubits.
- ☐ The ability to store quantum states which demands long qubit coherence time.

In the following, I review the published papers aligned with the directions of this thesis. The aim is to cover:

- Single photon sources candidates to be used as local qubits

[5] check the full requirement in [30]

- Spin qubit candidates as a spin–photon interface for future quantum information
- Cavity structures to improve the single photon emission properties

2.1 Single photon sources

A natural source of single photons is a two–level system with an active optical transition between its ground and excited states. In a material with a refractive index of n, the initially excited electron decay back to the ground state by spontaneously emitting a photon with a radiative rate of

$$\gamma = \frac{1}{\tau_{rad}} = \frac{n\,\omega_0^3}{3\,\pi\,\epsilon_0\,\hbar\,c^3}\cdot\mu^2 \tag{2.6}$$

where ϵ_0, $\hbar$, c are vacuum permittivity, reduced Planck's constant, and the speed of light in vacuum, respectively. The transition frequency and the optical transition's dipole moment are represented by ω_0 and μ, respectively. When the decay rate of the two–level system is equal to the inverse of the radiative lifetime (τ_{rad}), it is called "transform limited".

Quantum emitters in solid–state materials have atom–like optical transitions, and for this reason, they are called "artificial atoms". Their capability to integrate with the current fabrication techniques and effortless scalability gives them a unique advantage in quantum computing. Among different candidates, such as rare–earth ions, organic molecules, and dopants in semiconductors, quantum dot (QD) and defects in wide bandgap materials are worth highlighting. In what follows, we illustrate some of the characteristics of these two systems:

- **Quantum dots**: They are manometer–sized islands of smaller bandgap material within a larger bandgap energy material. A QD comprise thousands of atoms; however, it features discrete atomic transitions [31]. In such a system, a bound of a single electron in the conduction band and a single hole in the valence band form an exciton pair. This exciton can be neutral, negatively charged and positively charged, depending on the number of extra electrons or holes that QD is the host of. The transition frequency of QDs can be tuned by applying voltage. Relatively weak coupling to phonons and high radiative efficiency allow QD to consider one of the efficient single–photon sources.

- **Wide bandgap materials**: Point defects in semiconductor and wide bandgap materials (or insulator) can alter the translational symmetry of their host materials, and, as a result, they may create optically addressable bound states within the bandgap. These optically active centres, or colour centres, resembles

atomic energy transitions. Materials like Diamond, silicon carbide and hBN are among the most studied candidates in this category. Defects in these materials may be intrinsic, like vacancy or divacancy complexes, or extrinsic due to wanted or unwanted impurities.

To evaluate the efficiency of single–photon centres, the spectral properties of their emissions are one of the crucial factors. In a two–level system, when an electron relaxes from the excited state to the ground state, the relaxation process happens by emitting precisely one photon and zero phonons. It is therefore said that photon is emitting in zero–phonon line (ZPL). However, if the photon emission accompanies by emitting one or more phonons, that photon would spectrally be in the phonon sideband (PSB). Such a centre's emission spectrum comprises the ZPL and the PSB in a longer wavelength. The probability of an emitted photon being emitted into the ZPL compared to the entire spectrum is the Debye–Waller factor. This factor is used as a figure of merit to compare different single–photon sources.

In the case of spin–addressable optical transitions where more than one excited and ground state exists, the branching ratio (ξ) is defined as the proportion of decay into GS_i among all decays from ES_j, where subscripts i and j are different electronic states. Another factor is quantum efficiency (QE) which is the probability that quantifies how often excited electrons relax radiatively. Another factor relevant to the brightness of the single–photon centre is the excited–state lifetime (τ). This figure of merit characterises how long the electron remains excited before relaxing to the ground state. Therefore, the emission rate into a spin–addressable ZPL transition follows the below relation [32]:

$$\gamma_{ZPL} \propto \frac{\xi}{\tau} QE \tag{2.7}$$

For single two–level system, ξ can be replaced by Debye–Waller factor.

Table 2.1 shows a summary of emitters' properties in different material systems. InAs QDs exhibit high Debye–Waller factor, quantum efficiency and short radiative lifetime. These properties make QDs the best–performing photonic system. NV centre in diamond has relatively high quantum efficiency. However, their most significant obstacle is the poor Debye–Waller factor; i.e. Only 4% of the NV's fluorescence occurs through the ZPL. A promising solution is incorporating the defect centre into the photonic cavity structure to improve the lifetime, radiative quantum efficiency and Debye–Waller factor. V_{Si} is one of the naturally occurring defect points in SiC. This defect has a ZPL at ∼860 nm with an excited state lifetime of around 5.6 ns. In contrast to NV centre in diamond, this defect exhibits a higher debye–waller factor of approximately 40%. Some recently found emitters in hBN (with unknown origin) exhibit higher debye–waller factors than V_{Si} in SiC and NV

Table 2.1: Summary of emitters' properties

Platform	source	ZPL (nm)	DW factor %	Lifetime (ns)	QE %	Ref.
InAs/GaAs	QD	900-1550	>95	∼4	100	[6]
Diamond	NV	637	4	12-14	>72	[6, 33, 34]
SiC	V_{Si}	860	40	5.6		[6, 35]
hBN		580-630	80	2.65-3.2	60	[36, 37]

in diamond (∼ 80%). These emitters have ZPLs in the range of 580–630 nm with few nanoseconds excited state lifetimes and relatively high quantum efficiency (60%). In Section 2.5, I will elaborate on defects in hBN.

2.2 Spin qubits

Two–level systems with spin–addressable optical transitions are considered promising candidates for qubit realisation. Figure 2.1 shows an example of such a system. This system is an approximate level structure of boron vacancy that I will elaborate on more in Section 3.5 and Chapter 6. Paramagnetic defects with their electronic spin states are excellent examples of such systems. In the simplest form, Spin qubits comprise two eigenstates and their superpositions, which can be addressed and controlled by pulses of electromagnetic radiation. The main advantage of this platform is its reproducibility. Eigenstates are equilibrium quantum states, but their superpositions are nonequilibrium, and it relaxes into thermal equilibrium after a time. For quantum information, superposition states are highly interested; therefore, the long process time is highly demanding. Time characteristics of spin qubits are categorised in relaxation and decoherence times.

One mechanism that is linked to the relaxation process is phonon. There are a couple of processes that induce spin decay. In the direct (single-phonon) process, the electron spin emits or absorbs a phonon at the transition frequency. In the

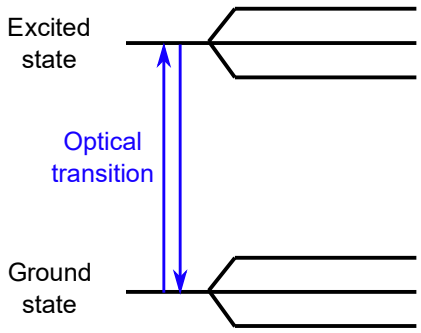

Figure 2.1: Spin–addressable two–level system. This is an approximate level structure of boron vacancy.

Raman process, a lattice phonon scatters off the defect and gains or loses energy corresponding to the spin's energy, resulting in a higher or lower energy photon. In the Orbach process, phonons excite spin to a different orbital state. Spin defects in wide bandgap materials like diamond, SiC and hBN have Debye temperature. High Debye temperature (due to strong chemical bonds) allows the isolated system, like defect centres, to not be interfered with by phonon modes. The ground and excited states splitting of defect systems like NV centre in diamond (similar to V_B^- in hBN) are at GHz frequency; As a result, the phonon's density of states in the direct process is extremely low in the GHz regime ($T \gg D/k_B = 0.05$ for D=1GHz) [38]. On the other hand, two-phonon relaxation in the THz frequency, like Raman and Orbach's processes, comprises thermally occupied phonons. Thermal excitation at room temperature is in the THz regime ($k_BT/\hbar$ =6.25 THz). As a result, two THz phonons scatter, and the energy difference between the two allows spin relaxation in the GHz frequency. It is expected that the effect of thermally occupied phonons will be reduced by lowering the temperature as their relaxation mechanisms are highly temperature dependant. In the relaxation process, the state of the electron spin changes. This mechanism is called "bit flip"; the figure of merit to evaluate the relaxation time of eigenstates is T_1.

In the superposition state, the duration that the phase between eigenstates is maintained refers to the coherence time[6]. However, some mechanisms cause the "phase flip" and result in a shorter time characteristic, refer as dephasing time. The figures of merit to evaluate coherence and dephasing times are T_2 and T_2^*, respectively. The intensity and the angle of the applied magnetic field to the spin qubit (either through static magnetic or electromagnetic pulses) introduce dephasing on individual magnetic moments (nuclei), and over time, their average net results "fan out". In addition, isotopes with different nuclear spin numbers create inhomogeneity in the environment which can affect coherence properties.

Some candidates offer good coherence time to realise spin qubits; however, we only concentrate on systems introduced in Table 2.1. Table 2.2 shows the time characteristics for spin qubits in QD, diamond, SiC, and hBN. Despite their excellent single photon characteristics, QDs exhibit poor coherence properties in nanosecond ranges. In contrast, defects in wide bandgap materials offer higher coherence properties. For example, the neutral divacancy (VV^0) in silicon carbide shows incredible relaxation and coherence times at cryogenic temperatures. This value is more than two orders of magnitude greater than the previous report on this subject, and currently, it is the highest record for the VV^0 centre. NV centre in diamond is the most well-studied defect centre among other candidates in wide bandgap materials. Defect centres in diamonds, in general, show good coherence properties. Lastly,

[6]qubit memory time

Table 2.2: Time characteristic of spin defect

Platform	source	Temp. (° K)	T_1 ms	T_2 (ms)	B–field (mT)	Ref.
InAs/GaAs	QD			3-10 $\times 10^{-3}$	4 $\times 10^3$	[39, 40]
Diamond	NV	4	2800	420	40	[41]
SiC	VV^0	5	103 $\times 10^3$	5.3 $\times 10^3$	1.8	[42]
hBN	V_B^-	300	18 $\times 10^{-3}$	0.1 $\times 10^{-3}$	12	[43, 44]

the recently found boron vacancy in hBN exhibit 18 µs relaxation time and 100 ns coherence time at room temperature.

2.3 Cavity structures

Criteria for an ideal single photon source are stringent enough to make their realisation difficult. Besides discussed checklist, gigahertz repetition rate, tunable emission wavelength, and an electrical trigger are among the very demanding wish lists [45]. In 1946's article "Spontaneous emission probabilities at radio frequencies", Purcell discovered that enhancing the interaction between light and an emitter is possible by engineering the surrounding electromagnetic environment [46]. Since then, to overcome challenges, cavity quantum electrodynamics has offered different platforms to realise the ideal single photon source. In addition, these platforms can enhance the efficiency of spin qubits by increasing the photon emission rates into a well–defined cavity–coupled mode. Therefore, cavity structures interface between optical photons and individual quantum emitters and spin qubits such as single photon sources in semiconductors (excitons in QDs), wide bandgap materials (defects in diamond, Silicon carbide, and hBN), and 2D materials (excitons in transition–metal dichalcogenide family) [32].

The spontaneous emission of a photon from a two–level atom is a property of the atom–vacuum system. Under such circumstances, an infinite number of vacuum states is typically available to the radiated photon [47]. Fermi's Golden rule gives the transition rate for spontaneous emission:

$$\gamma_r = \frac{2\pi}{\hbar^2} |M_{12}|^2 \, g(\omega) \tag{2.8}$$

$$g(\omega) = \frac{\omega^2 V_0}{\pi^2 c^3} \tag{2.9}$$

$$M_{12} = \langle \, p \, . \, \mathcal{E} \, \rangle \tag{2.10}$$

where M_{12} and $g(\omega)$ are the transition matrix element and the density of states, respectively. For the density of state, the standard result for photon modes in free

space is used. For the matrix element, the electric dipole (p) interaction is used. Since there is no external field inside the cavity, $\mathcal{E}$ indicates the vacuum field. The above formulas assume that the emissive atom is in a large cavity with a volume of V_0 with a negligible effect on the properties of the atom. Eventually, the transition rate can be written as Equation (2.6) where $n = 1$, i.e.:

$$\gamma_r = \frac{1}{\tau_r} = \frac{\mu^2\,\omega^3}{3\,\pi\,\epsilon_0\,\hbar\,c^3} \tag{2.11}$$

When the two–level system is placed inside a single–mode[7] cavity with a volume of V_0, one can use Fermi's Golden rule to determine the transition rate. If we consider the same resonance between the atom and the cavity, we have the following:

$$\gamma_{cav} = \frac{2\,Q\,\mu^2}{\hbar\,\epsilon_0 V_0} \tag{2.12}$$

where Q is the quality factor of the cavity at the resonance frequency. Modifying the vacuum state can thus inhibit or enhance spontaneous emission. In the weak coupling regime (low Q), the atomic transition is still irreversible; However, in this regime, the cavity modifies the vacuum states, and these changes manifest as affecting the atom's transition rate. To quantify this rate compared to the case of free space, one can use the Purcell factor [48]:

$$F_P = \frac{\gamma_{cav}}{\gamma_r} = \frac{3Q(\lambda/n)^3}{4\pi^2 V_0} \tag{2.13}$$

This figure of merit is a helpful tool for comparing different cavity structures.

For the case of defect centres in wide bandgap materials, if the spontaneous emission rate of photons within the ZPL is equal to γ_r, we can define the total dephasing rate (γ) of photons as follow:

$$\gamma = \gamma_r + \gamma_d + \gamma_1 \tag{2.14}$$

where γ_d and γ_1 are the pure dephasing rate and dephasing rate from all other pathways, respectively. γ_1 includes the emission rate within the nonradiative path and emission into the PSB. When the defect centre is placed inside the cavity designed at the same resonance frequency as the emitter, its local photonic density of states increases. Enhancement of the spontaneous rate compared to dephasing rates indicates the domination of radiative emission over non-radiative decays. In addition, the radiation pattern of the defect centre coupled to the cavity can also be improved because the cavity efficiently funnels the spontaneously emitted photons in a single

[7] it means that there is only one resonant mode of the cavity that is close to the emission frequency of the atom

direction of space.

Another important figure of merit is the photon collection efficiency (η), which is the fraction of the spontaneous emission collected by the collection optics. Collection optic, in this definition, can be an objective lens or a fibre. In the absence of a cavity, the collection efficiency for an emitter in a material with a refractive index of n_1 is equal to [49]:

$$\eta = \frac{1}{32}\left[15\left(1 - \sqrt{1 - (NA/n_1)^2}\right) + \left(1 - \cos\left(3\arcsin\left(NA/n_1\right)\right)\right)\right] \tag{2.15}$$

In the above formula, the numerical aperture (NA) defines the angle at which the collection optic collects the photons. Placing the emitter in a cavity leads to the fields produced by the source being reflected in the emitter site. The emission will be enhanced if the reflected field is in phase with the source. In other words, the cavity alters the allowed electromagnetic modes near the source. The emission will be enhanced if the emitter is in resonance with the mode. To maximise the efficiency, the best strategy is to ensure the cavity only supports the lowest order more at the emission frequency [49]. In contrast to an emitter in free space which emits in all directions, an emitter in a cavity has limited leakage pathways. In the ideal case, the cavity should only support one leakage path, which guides emission towards the collection. Therefore, cavities can modify the propagating temporal fields of the single photon centre, improve η, and achieve higher brightness. The brightness of single photon sources and spin qubits is critically essential. In addition to the Purcell factor and the collection efficiency, there are other figures of merit, but they are not in the scope of this thesis.

Among different platforms, pillar and bullseye structures offer good Purcell factor and collection efficiency. Table 2.3 shows some studied structures for single photon emitters in QD and diamond. In [50], Gazzano *et al.* experimentally showed a Purcell factor of ~ 3.9 for a QD coupled to a cavity mode of the pillar structure. Their calculation indicated a collection efficiency of $\sim 80\,\%$. In 2019, Wang *et al.* investigated pillar and bullseye cavity structures for QD emitters. They proposed a Purcell factor of ~ 25 and a collection efficiency of $\sim 86\,\%$ for their bullseye structure [51]. Bullseye structure was also investigated for other platforms, including NV centre in diamond. Zheng *et al.* studied NV centre in bulk diamond coupled to a bullseye structure, showing that the collection efficiency could reach $\sim 80\,\%$ [52]. In another study, Komisar *et al.* investigated the NV centre in nanodiamonds and proposed a bullseye structure to increase the collection efficiency to $\sim 80\,\%$ [53]. In both works, the studied structures didn't improve the Purcell factor.

Table 2.3: Comparison between different cavity structure (theoretical results)

Cavity	source	n_{cavity}	NA	η (%)	F_P	Ref.
Pillar	QD	3.5	0.67	> 80	22.5	[50]
Bullseye	QD	3.54	0.65	> 86	< 25	[51]
Bullseye	NV	2.41	1.42	> 80	~ 1	[52]
Bullseye	NV	2.2	0.9	< 80	< 1	[53]

2.4 Bullseye Bragg grating structure

Since the discovery of quantum emitters in 2D materials (check Section 2.5 for the detailed discussion), coupling these emitters to photonic structures has been investigated. Bullseye Bragg grating is among the structures that enhance collection efficiency and the Purcell factor of the emitter coupled to the cavity. In 2011, Davanco *et al.* demonstrated the first circular dielectric grating on suspended GaAs, which exhibited both Purcell enhancement and improved directionality. Bragg grating and Purcell enhancement is discussed in Chapter 4. In 2018, Duong *et al.* transferred a monolayer of Tungsten diselenide (WSe_2) to a circular Bragg grating made from Si_3N_4 and experimentally reported a Purcell factor of 1.7 [54]. Their simulation results showed that the Purcell factor of 16 can be achieved in an ideal coupling condition. In 2019, Mey *et al.* fabricated a bullseye microcavity structure on GaP and reported ten times enhancement of the Tungsten disulfide (WS_2) bandgap photoluminescence emission at room temperature [55]. Later, Chen *et al.* reported 34 and 5 times enhancement of the photoluminescence and second harmonic emissions in WS_2, respectively [56]. In their work, they fabricated circular Bragg gratings on SiN on top of SiO_2. A similar study on hBN was published in the same year by Bernhardt *et al.* in which the authors reported the enhancement of the second harmonic emissions by three factors [57]. In recent work, Iff *et al.* transferred a monolayer of WSe_2 on a bullseye Bragg grating fabricated from AlGaAs on SiO_2 [58, 59]. To induce local strain on the WSe_2 crystal, they used the focused ion beam to grow a 200 nm nanopillar at the centre of the bullseye. This approach allowed them to deterministically create single–excitonic emitters in WSe_2 verified by second–order correlation measurement ($g^{(2)}(0) < 0.5$). They reported the Purcell factor of 14 and 5 based on their simulation and experimental works. It should be noted that they used a gold layer at the bottom of the SiO_2 layer to improve the collection efficiency. Table 2.4 summarises important parameters discussed above.

Table 2.4: Bullseye Bragg grating structure in the literature

Emitter	Substrate	F_P	CE (%)	NA	$n_{grating}$	λ_{exc} (nm)	Ref.
WSe_2	Si_3N_4	16 ($\sim$4)[1]	>45	0.9	2.02	750	[54]
WS_2	Si_3N_4	8 ($\sim$2)		0.9	2.02	$\sim$ 620	[56]
WSe_2	AlGaAs	14 ($\sim$ 10)		0.42		$\sim$ 725	[58, 59]

[1] experimental value

2.5 Defect generations in hBN

One of the building blocks to realise quantum technology is single photon emitters. Colour centres in semiconductors and wide bandgap materials are among the possible candidates to realise single photon emitters. Colour centres are point defects that bind electrons to an extremely localised region on the angstrom scale; therefore, they behave as atoms embedded in the crystal [4]. Solid-state quantum emitters are typically embedded in high refractive index bulk material, which limits the collection efficiency of the quantum emitter. To solve this issue, photonic structures must be fabricated around these quantum emitters, which demand excellent integration ability. The discovery of 2D material opens a new era of studying new physical phenomena. In particular, single photon emitters confined in the 2D geometry of these materials greatly enhance the collection efficiency. In addition, they facilitate integration with photonic structures [60].

With the discovery of single defect centres in hBN in 2016, this wide bandgap 2D material enters the race of single photon sources. The optical, electrical and magnetic properties of defect centres can depend on the methods are being created. Some of the frequently used approaches to generate defect centres in the literature are described below.

2.5.1 Defects types in hBN

Defect centres in hBN can be categorised in two groups; native and non–native defects. Native or intrinsic defects are formed during the growth process of hBN [61]. The simplest vacancy defects are boron vacancy (V_B) and nitrogen vacancy. Abdi *et al.* showed that V_B^- has triplet ground and excited states, and later, Ivady *et al.* calculated the zero–field splitting for the ground and excited states of this defect [62, 63]. In addition, the theoretical calculation predicted the ZPL emission at 1.65 eV [63]. On the other hand, Weston *et al.* reported that the V_B has a paramagnetic state with spin–3/2 [64]. Also, theoretical calculation suggested that the V_N^0 and V_N^+ are doublet and singlet states [64, 65].

Antisite defects could form either in a native way, such as an imperfect growth

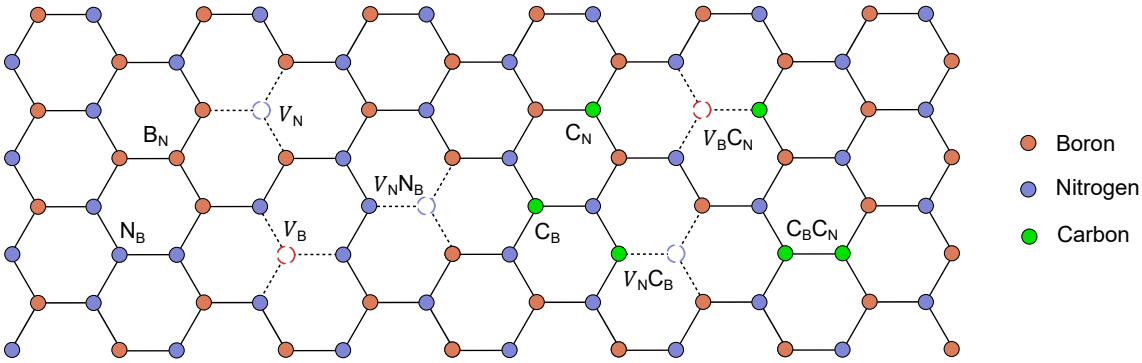

Figure 2.2: Atomistic geometry of some of the common defects in hBN, including B_N, N_B, V_N, V_B, V_NN_B, C_N, C_B, V_NC_B, V_BC_N, and C_BC_N.

condition or a non–native way, including irradiation or annealing in a specific environment. These defects include boron antisite (B_N), nitrogen antisite (N_B) and nitrogen vacancy coupled with nitrogen substitution for boron on adjacent sites (V_NN_B), etc [61]. Weston *et al.* reported that the B_N defect has a nonmagnetic ground state, whereas B_N^+ and B_N^- are spin–1 systems. Similarly, it is reported that the N_B is singlet, but N_B^+ is a spin–1/2 system [64]. Theoretical calculations by Sajid *et al.* indicated that V_NN_B is a spin doublet system, whereas $V_NN_B^+$ and $V_NN_B^-$ are both singlets [66].

Carbon is a common impurity in hBN, and because of that, some carbon-related defect candidates exist. Carbon monomers (C_B, C_N), carbon dimers (C_NC_B), V_NC_B, and V_BC_N, are among these candidates [61]. C_B and C_N are the simplest carbon–based defects. Auburger and Gali reported these two defects to have paramagnetic spin–1/2 ground states with ZPL at 1.695 eV and 2.468 eV, respectively [67]. In contrast, C_NC_B is considered nonparamagnetic (singlet) with single photon emission at 4.1 eV; however, its charged states ($C_NC_B^+$ and $C_NC_B^-$) exhibit paramagnetic doublet [67, 68]. Sajid *et al.* studied V_BC_N and V_NC_B and predicted that the former has triplet ground states, whereas the latter is a singlet state. The ZPL of the V_NC_B is suggested to be around 1.95 eV[69]. Mendelson *et al.* incorporated carbon to create defects in hBN and attributed the defect with the ZPL at 2.12 eV to $V_BC_N^-$ [70].

2.5.2 Naturally occurring

The first report of single photon emission from hBN bulk crystal was published in 2016 [71]. In this paper, Martinez *et al.* reported two emitters with similar spectra appearing at 596 nm and 629 nm, in which both featured first and second phonon replicas. In [72], Xu *et al.* reported various emitters within the range of 550–675 nm in the exfoliated flake. In 2019, Mendelson *et al.* reported the growth of hBN films using low–pressure chemical vapor deposition (CVD) [73]. In this work, the author

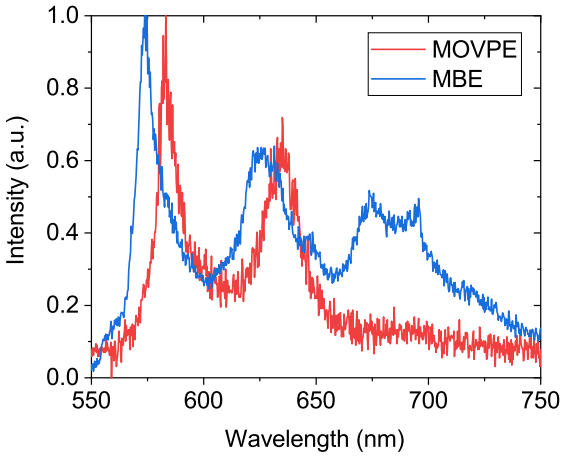

Figure 2.3: Naturally occurring defect centres in hBN. Spectra of defect centres found in MOVPE (red) and MBE (blue) grown samples. Figure adapted from reference [70].

investigated different growth foils, including Ni, Fe and Cu and showed they could create single photon centres with ZPL at 580 ± 10 nm. In the same year, Comtet *et al.* studied single photon emitters in CVD–grown monolayer and multi–layer hBN [74]. This study found two groups of defects at 580 and 625 nm with full width at half maximum (FWHM) of 15 and 50 nm, respectively. In the relevant study in the same year as the two previous reports, Stern *et al.* reported highly reproducible sources in CVD–grown hBN with the emission maxima at 575 ± 15 nm [75]. Later, Mendelson *et al.* studied carbon–doped hBN grown by two different approaches [70]. In the first approach, the hBN was grown by metal–organic vapour–phase epitaxy (MOVPE), and they showed that low carbon flow could create single defects around 580 nm with one phonon replica; however, higher carbon flows resulted in broader emission signature and eventually the creation of ensembles of defects. In the second approach, they utilised molecular–beam epitaxy (MBE) to grow hBN. Under the carbon–doped condition, the hBN hosted single defect centres in a broad range of wavelengths (575–780 nm), which suggests they are different complexes, including $V_B C_N^-$, $V_N C_B$, C_B, and C_N. Figure 2.3 shows the spectra for MOVPE and MBE grown samples.

2.5.3 Plasma/annealing treatment

In 2018, Vogl *et al.* used the plasma etching technique followed by high–temperature annealing to create and stabilise defects, respectively. [76]. Vogl *et al.* claimed that defects are created during the surface interaction of the thick layer of hBN (50 nm) with plasma, and they became optically activated (stabilised) after the annealing process. They observed a ZPL peak around 553 nm with the linewidth about 2.8 nm. Also, the average lifetime and second order correlation function at

zero delay ($g^{(2)}(0)$, check Subsection 3.2.4 for the detailed discussion) were 1.1 ns and 0.3, respectively. However, Vogl claimed that the best single photon emitter in terms of linewidth was seen at 566 nm with the FWHM of 1.3 nm. The $g^{(2)}(0)$ and lifetime were 0.033 and 294 ps, respectively. In addition, they discovered that lower annealing temperature leads to weak ZPL, and the defects are not fully activated; while at higher temperatures or for a more prolonged annealing duration, defects spectrally diffuse too much. Also, they found that annealing under a vacuum reduces the defect yields drastically. A similar study was reported by Xu *et al.* in the same year [72]. Later, Vogl *et al.* suggested that because the negatively charged boron vacancy (V_B^-) is mobile at annealing temperature around 850 °C, it is expected that interlayer interstitial defects are also mobile at this temperature due to their low interlayer bond energies [77]. Upon stability and linewidth of emitters at this temperature, they attributed these effects to the removal of interstitial defects and single V_B^- which improve the charge stability and reduce electrical noise. The year after, Comtet *et al.* used oxygen plasma treatment (100 mW, 30 s) to damage the crystal lattice of exfoliated hBN and reported the generation of defects with emission around 575 nm [74]. In the same year, Li *et al.* showed that the treatment under ultra–violet (UV) ozone condition can create single defect centres with a sharp ZPL at 567 nm [78]. In a recent study, Chen *et al.* showed that exposing exfoliated hBN to two different plasma environment, H_2 and CH_4, but with the same condition (900 W, 10 min) can create narrow linewidth but weak emitters [79]. Next, they utilised UV ozone (2 h) and annealing (850 °C, 30 min) as post–treatment separately and reported that both post–treatment could generate narrow linewidth colour centres.

2.5.4 Strain

In materials like WSe_2, periodic strain via structures like nanopillars creates gradient and strain minima, which can funnel a single exciton to the point of maximally applied strain. As a result, this strain forms a hybrid state with a localised point defect and broken valley symmetry that allows for the radiative decay of the single hybrid exciton [80]. Recently, it has been suggested that local strain is unlikely to be solely the origin of single photon emitters in transition metal dichalcogenide, but, rather, the interplay or combination of local strain with the disorder in the environment and/or crystal defects [81]. It is shown in other platforms like the diamond that the electric dipole moment of the centre can be sensitive to the local strain depending on its symmetry; therefore, by strain engineering, it is possible to tune the polarisation and wavelength of the centre's emission [82]. It is suggested that strain can alter the orbitals of the ground and excited state manifolds [83]. This can modify the optical emission properties [84].

In 2018, Proscia *et al.* reported the first demonstration of creating emitters in hBN using nanopillars to apply local strain on the hBN crystal lattice [85]. In this study, they transferred 20 nm and 40 nm layer thickness of CVD–grown hBN on nanopillars with diameters in the range of 75–2000 nm. Based on the result, the nanopillars with a diameter of 75 nm exhibited emissions with the ZPL at 550 nm. They observed piercing in hBN on top of pillars with heights above 155 nm, but they did not see any piercing at a height less than 155 nm. In a recent study, Li *et al.* studied CVD–grown on four different pillar diameter sizes (250 nm, 450 nm, 650 nm, and 950 nm) with a fixed height (650 nm) [86]. Based on their results, emitters on smaller–diameter nanopillars showed slightly higher count rates. The excited–state lifetime of these emitters is around 4.2 ns. In addition, they reported that 85 % of emitters remained stable over 120 s while 80 % of emitters exhibited $g^{(2)}(0) < 0.5$. Moreover, they showed that transferring exfoliated flake of hBN on nanopillar could not create defect centres in the crystal. It should be mentioned that transferred hBN compared to CVD is likely to have different morphology on nanostubs; for example, transferred hBN will have wrinkles and strain, but CVD will conformally cover the stub.

2.5.5 Annealing

High–temperature annealing on the diamond is shown to repair the diamond lattice. In addition, it is suggested that vacancies mobilised by annealing can bind to a nitrogen atom [87]. Hunt et al. explained that annealing adds energy to the lattice and enables the migration of mobile defect species as well as the formation of new species. Their paper described the potential of annealing alone to increase total defect density in the sample [88]. Annealing was the first reported method to create single defect centres in hBN. In 2016, Tran *et al.* annealed a multilayer drop–cast hBN at 850 °C for 30 min under 1 Torr of Argon in a tube furnace [89]. By this approach, he could create a single photon source with more than 4 million counts per second at 625 nm. This defect with a 3.1 ns excited–state lifetime was attributed to the N_BV_N[8] defects. A later study by the same author revealed that annealing in different environments could create at least two groups of emitters [90]. Tran *et al.* annealed drop–cast hBN in Argon, O_2, H_2 and NH_3 environments with the same condition (500 °C, 30 min) and reported two classes of emitters; the first group consists of emitters in the 576–652 nm range with exhibited a broad and asymmetric ZPL with pronounced doublet PSBs. The second group comprised emitters with narrow and more symmetric ZPL in the 681–762 nm range with weak PSB.

In 2019, Li *et al.* studied annealing at 550 °C and 750 °C (3 h, air) and reported

[8] Anti–site complex defect: Nitrogen occupied the boron side and a missing nitrogen atom

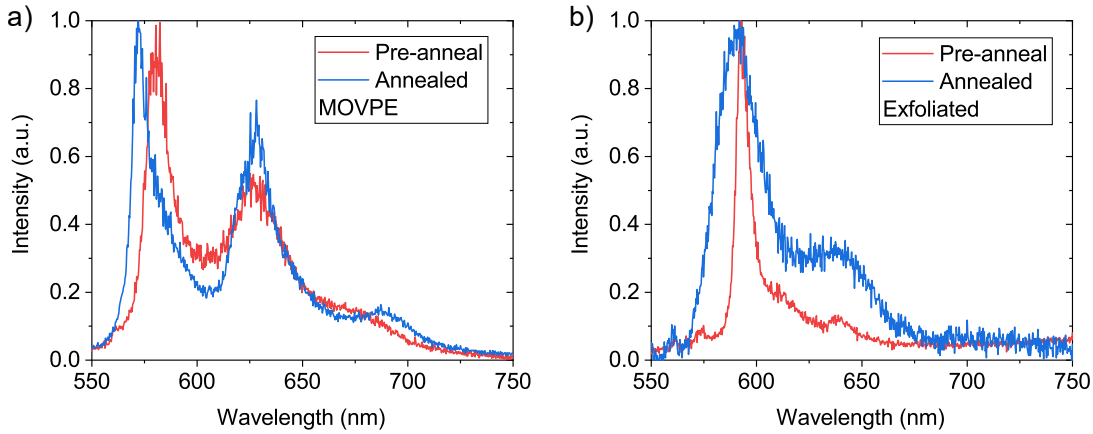

Figure 2.4: Effects of post–annealing on defect centres in hBN. Spectra of defect centres found in a) MOVPE grown and b) exfoliated samples. Post–annealing data (blue) by average is broader than pre–annealing data (red). Figure adapted from reference [70].

improved FWHM (by average 8 nm) and $g^{(2)}(0)$ (by average 0.4 ± 0.2) for samples annealed at 750 °C [78]. In the following year, Mendelson *et al.* annealed carbon implanted exfoliated hBN as well as samples grown by MOVPE and MBE at 1000 °C for 2 h at a high vacuum ($< 10^{-6}$ Torr) and reported that post–annealing helped to form single photon emitters; however, the FWHM of emitters in all samples increased after the annealing steps [70]. Figure 2.4 shows the spectra for MOVPE and exfoliated samples before and after annealing. In the same year, Lyu *et al.* investigated the effect of annealing in a carbon–rich atmosphere on the exfoliated hBN flakes [91]. For this purpose, they annealed samples at 900 °C, 1000 °C, and 1100 °C in the Ar environment (1 Torr) with the supply of CH_4 and compared the results with a sample annealed at 1000 °C in the Ar environment (1 Torr) but without the supply of CH_4. The duration of annealing was 1 h in all cases. According to their results, annealing at 1000 °C created more emitters that appeared in a broad range of wavelengths (520–720 nm).

2.5.6 Irradiation

In 2016, Tran *et al.* studied electron irradiation (15 keV, 1.4 nA, 1 h, low vacuum, H_2O vapour environment) exfoliated hBN and reported the generation of an emitter at 690 nm [90]. A few months later, Chejanovsky *et al.* irradiated exfoliated hBN with two different ion sources (He and N) with similar fluence (2×10^{-7} mbar) but slightly different acceleration energies (2 and 2.5 keV) [92]. After irradiation, samples were annealed in a vacuum at 850 °C. Based on this study, the lower dose of both ions could create single defect centres around 574–581 nm. In the same year, Choi *et al.* investigated samples irradiated with B^-, BN^-, O^-, and Si^- with a similar irradiation profile (50 keV, 10^{10} ions/cm^2) and compared the results with electron beam

irradiated sample (15 keV, 5×10^{18} e/cm^2) [93]. They performed a post–annealing step for the ion–irradiated samples (850 °C, 30 min, 1 Torr Ar), whereas the electron irradiated sample was not annealed. They hypothesised that ion irradiation significantly damages hBN crystal; therefore, post–annealing partially heals it. On the other hand, electron irradiation is a subtler process with minimal damage to the surrounding crystallographic environment. According to their results, all methods can create single defect centres ($g^{(2)}(0) < 0.5$) at 575–600 nm with prolonged stability (> 3 min).

A year later, Grosso *et al.* reported that He^+ irradiated exfoliated hBN (5×10^{15} ions/cm^2) with subsequent annealing (Ar, 1000 °C, 30 min) could host a single photon emitter with 7×10^6 counts per second with $g^{(2)}(0) < 0.5$ [94]. In 2018, Duong *et al.* investigated different hBN samples irradiated with the same irradiation profile (2 MeV, 10^{15} e/cm^2) [95]. In this study, the author studied high–purity, B–enriched and carbon–enriched multilayer samples of hBN. According to their results, all samples can host single emitters around 575–600 nm; however, the B–enriched sample showed higher intensity emitters (10^5 count rates) with better stability (200 s) compared to the carbon–enriched sample. In addition, high–purity samples exhibit more emitters per flake ($\sim$9).

In 2020, Mendelson *et al.* reported an extensive study on the implantation method to generate emitters in exfoliated and MOVPE–grown hBN [70]. This work used carbon, oxygen and silicon as implantation sources. For Carbon implantation, they first studied different fluences (10^{11}–10^{14} ions/cm^2) on MOVPE and exfoliated hBN (ion energies remained constant; 10 keV). According to their work, higher fluences resulted in a higher density of single photon sources with smaller FWHM. In the next step, they studied MOVPE and exfoliated hBN under carbon implantation with the fluence of 10^{13} ions/cm^2 and 10 keV energy. They observed that the FWHM of ZPLs improved from 20 nm to 5 nm (by average) for emitters that appeared at the wavelength range of 575–592 nm compared to the reference sample. Upon annealing (1000 °C, 1 Torr, Ar environment), they observed that the wavelength of the emitter barely changed, but the FWHM increased. Their theoretical calculation suggested that the generated defects are V_BC_N- defects. On the other side, oxygen and silicon implantation studies on MOVPE–grown hBN showed that the V_B^- centres at 800 nm were created; however, after the annealing (1000 °C, 1 Torr Ar environment), the only spectral feature observed is a broad peak at 630 nm. Figure 2.5 shows the carbon implanted spectra for MOVPE and exfoliated samples before and after annealing.

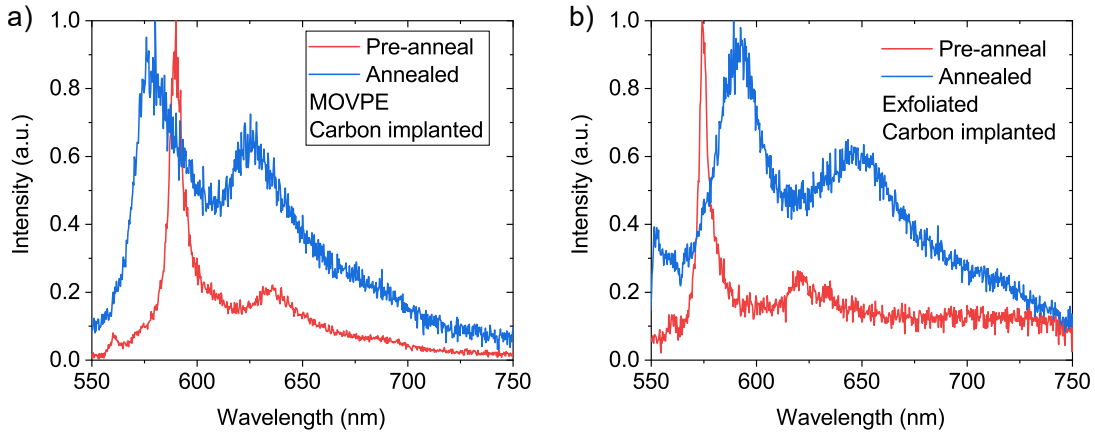

Figure 2.5: Effects of carbon implantation and annealing on defect centres in hBN. Spectra of defect centres found in carbon implanted a) MOVPE grown and b) exfoliated samples. Post–annealing data (blue) by average is broader than pre–annealing data (red). Figure adapted from reference [70].

2.6 Spin defects in hBN

In 2019, Exarhos *et al.* were the first group to report single photon emitters in hBN with magnetic field–dependent emission at room temperature. This single emitter featured a peak at 730 nm with bunching behaviour in the second–order correlation, which suggested the emitter is a three–level system; however, the origin of this defect remained unknown. Next year, Gottscholl *et al.* reported the first optically detected magnetic resonance (ODMR) study on a defect with a broad emission wavelength of around 830 nm [96]. ODMR is a spectroscopy technique that combines optical excitation and magnetic resonance to detect signal contrast due to spin selective optical pumping of the magnetic states. In this work, they used neutron irradiation (2.3×10^{18} n/cm^2) to generate defects in the crystal lattice of exfoliated hBN. This photoluminescence (PL) contrast of this defect exhibited an ODMR signal with zero field splitting (ZFS) at 3.48 GHz at zero magnetic field perpendicular to the sample. electron paramagnetic resonance (EPR) study revealed that this defect has a triplet ground state (GS) with a splitting constant around 47 MHz, known as hyperfine interaction (HFI). EPR is a spectroscopy technique to study atoms with an unpaired electron. This study, alongside the angular dependence EPR spectra, suggested that the defect system is V_B^-. In addition, they reported that the ion implantation using Lithium and Gallium could create V_B^- centres. A few months later, Chejanovsky *et al.* reported a new type of spin defect in hBN that exhibited single photon emission at around 700–800 nm [97]. They measured the excited–state lifetime of these centres to be around 2.5 µs. In addition, they extracted spin-lattice relaxation times (T_1) of $\sim$ 13–17 µs. Finally, the spin lifetime estimated from the power dependence measurement of the ODMR contrast revealed that the T_2^* is

$\sim$ 40–60 ns. In the same year, Kianinia *et al.* reported the generation of V_B^- centres using different irradiation sources[98]. In this study, the authors investigated N, Ar and Xe as three different ion sources and showed that all sources could create V_B^- centres; however, with a fix fluence at 3×10^{16} ions/cm^2, N–implanted samples exhibited emitters with higher intensity. In addition, Xe–implanted samples showed good stability over 30 s. The same month, Mendelson *et al.* reported a new type of spin addressable defects in hBN [70]. They studied carbon incorporated hBN grown by MOVPE and characterised single emitters with ZPL emission around 580 nm. Next, they measured the PL contrast and showed that these centres featured positive ODMR contrast in the magnetic field around 19–29 mT with microwave frequency around 500–900 MHz. In 2021, Gottscholl *et al.* investigated the coherent control of V_B^-. First, they studied Rabi oscillation and reported Rabi frequencies in the range of a few MHz [43]. Then, their studies on T_1 showed that it is around 18 µs at the ambient condition, but the temperature–dependent study revealed that the T_1 could reach 10 ms at 20 K. The spin–echo study in their work indicated that the T_2^* is around 1.5 µs and is temperature–independent. Finally, they implemented the hole–burning technique and increased the T_1 to 25 µs. This technique can determine the sample's dominant source of inhomogeneous broadening. A narrower ODMR spectrum and higher spin coherence time can be achieved by removing this source of broadening from its initial state [99]. In the same year, Baber *et al.* irradiated hBN with carbon (10 keV, 10^{14} ions/cm^2) and studied the spin properties of excited state (ES) in V_B^- [100]. They reported the ZFS value of ES to be 2.09 GHz. In addition, they reported another transition that appeared in the ODMR frequency versus the magnetic field and attributed it to their sample's impurity. Moreover, they demonstrated that the contrast in the ODMR study could be enhanced using a time–gated detection scheme.

2.7 Discussion

This chapter discussed the benchmarks and criteria for realising quantum computing and communication. Then, I discussed the characteristics of defect centres in wide band gap materials as promising candidates for future applications. Next, I reviewed recently published papers to address the progress in bullseye Bragg grating structure for enhancing photon emission in 2D materials, defect generation in hBN, and spin defects in hBN. In the following chapters, I will elaborate on my works in this thesis; in particular, I designed a cavity for surface–mounted emitters. Then, I investigate various approaches to create defect centres in hBN. Finally, I elaborate on the spin qubit work in hBN.

CHAPTER 3

Methods

3.1 Introduction

In this thesis, I utilised different experimental tools and computational methods to study defect centres in hBN and design cavity structures. Before elaborating on the results, I discuss the tools and methods I used in this chapter. This chapter comprises three main sections; in the first section, I present the optical system and the Hanbury Brown and Twiss (HBT) technique used to characterise single photon emission in the defect generation chapter. The second section is related to the concept of finite–difference time–domain (FDTD) and critical criteria for evaluating photon–cavity coupling. Finally, I illustrate optical and electronic systems exploited in the ODMR chapter.

3.2 Single photon characterisation

As part of this PhD, I studied defect centres in hBN. To locate these centres, it is essential to use a high–resolution scanning confocal microscope with sub–micron spot size. After finding these centres, I characterised them with a spectrometer and measured the second–order correlation function using the HBT interferometry technique. In what follows, I elaborate on the setups I used for these purposes.

3.2.1 Optical setup

I characterised samples using a home–built confocal PL microscopy setup shown in Figure 3.1.a for the emitters generation chapter. hBN emitters studied in this thesis are around 550–900 nm which fit well in the characterisation window on this setup. A temperature–controlled diode laser with an emission wavelength of 520 nm (LTC56B, Thorlabs) was used as the excitation source. Broadband dielectric mirrors and dichroic beamsplitter were used to redirect the excitation beam toward the galvo mirror (GVS002, Thorlabs). A galvo mirror consists of dual–axis galvanometer–based scanning servo motors with optical mirrors mounted on them. To control applied voltage to these mirrors, a LabVIEW program is written to create digital signals, which then is sent to a data acquisition (DAQ) card to drive servo motors. Next, the beam was passed through two achromatic doublet lenses where the distance between galvo, two achromatic doublets and the objective par-

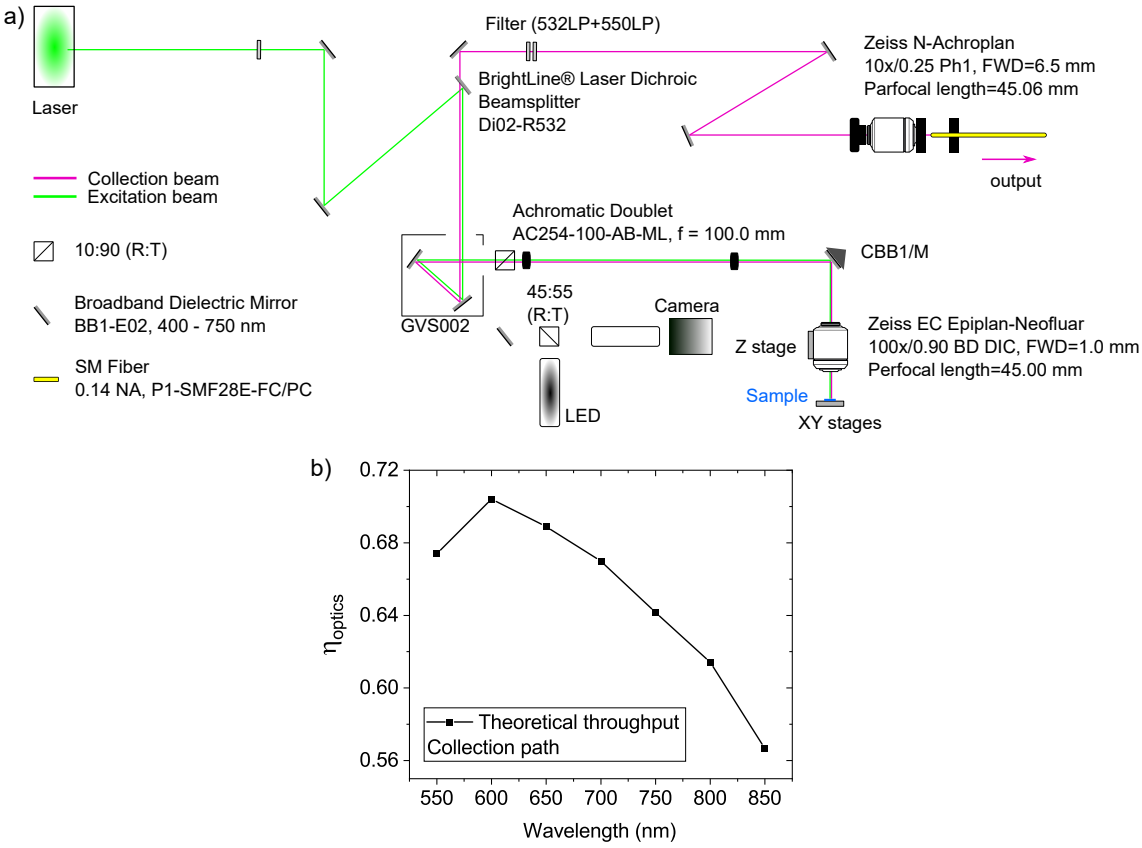

Figure 3.1: Room temperature $4f$ confocal microscopy. a) The Green and pink lines depict the optical paths of the excitation and collection beams, respectively. In this setup, two objective lenses are utilised; a 100× objective lens with NA = 0.9 is used to focus the laser light and collect emitted photons from the sample. The second objective lens with NA = 0.25 is used to couple free space emission light to the fibre in the collection path. To scan the sample, a galvo mirror with two achromatic doublet lenses in an equal distance in between was placed $4 \times f$ apart from the objective lens. I used a dichroic beamsplitter to separate the excitation and emission optical path. b) Estimate of the theoretical throughput of the collection path of the system between two objective lenses.

focal plane was fixed at the focal plane of the lens (i.e. f). This configuration is the so–called $4f$ [94]. The objective lens used in the 3rd chapter was 100× with NA = 0.9 (Zeiss). The laser beam excites the sample, which was mounted in an XY–translational stage.

The emission from the sample was then collected with the same objective lens and optics in the $4f$ setup and transmitted through a dichroic beamsplitter. I used laser BrightLine single–edge laser–flat (DiO2–R532, Semrock) as the dichroic beamsplitter to reflect the laser beam in the excitation path (R > 94% 514 – 532 nm) and transmit the emission beam at wavelengths longer than 532 nm in the collection path (T > 93% 541.6 – 1200 nm). I used optical filters to clean the collection beam from unwanted wavelengths (R > 90%). Finally, the PL emission was focused on a single mode fibre using a 10× objective lens with NA = 0.25 (Zeiss). I also

used the white light source for illuminating the sample and a camera to observe the sample's surface with the 100× objective lens. Figure 3.1.b illustrates the theoretical throughput of the collection path of the system between two objective lenses.

3.2.2 Spectroscopy and photon correlation setups

The PL spectra of defect centres were measured using a fibre–coupled spectrometer with a cooled charge–coupled device (CCD) array. For this purpose, I utilised two different spectrometers; for Section 5.3, Section 5.4, and Section 5.5, I used Shamrock 750 equipped with iDus 420 (Andor) and Kymera 328i with iKon–M 934 (Andor) for Section 5.6 and Section 5.7. The former has a resolution of ∼0.09 nm and a throughput of $\gtrsim$ 90%, whereas the latter has a resolution of ∼0.6 nm and a throughput of $\gtrsim$ 80%.

To detect and count single photons, a single photon detector can be used; however, photon detectors need a period to detect the next arriving photon efficiently. This period is known as dead time and limits the detection efficiency of single photons (check subsection 3.2.3). To circumvent this problem, the collection path is split into two identical paths in the HBT setup. The photon arrival times are tagged and post–processed. In this way, the coincidence rate between two detectors is measured. This setup is depicted in Figure 3.2. I exploited the second–order correlation function ($g^{(2)}(t)$) to verify the single–emitter characteristic of defect centres. This function quantifies the intensity–intensity correlation between pairs of photons, which can be used to calculate the probability of generating single or more photons. This parameter is discussed in more detail in Subsection 3.2.4. In my experiment, I mainly used the start–stop scheme (or histogram mode) of the time controller (ID900, ID Quantique), which measures the time delay between two detection events on both detectors which consist of silicon avalanche photodiodes (APD)s (SPCM–AQRH, Excelitas). Second–order correlation function is discussed in Subsection 3.2.4.

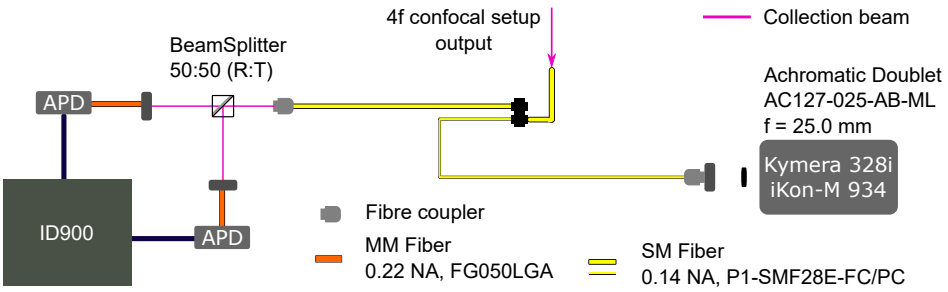

Figure 3.2: Spectroscopy and photon correlation setups. The fluorescence photons are directed either to a spectrometer equipped with a CCD camera or to a HBT setup to record the second order intensity correlation function.

3.2.3 Electronic setup

Figure 3.3 shows the electronic setup for the single–photon characterisation used in this work. A typical instrument response function (IRF) of an APD can be considered a Gaussian distribution in which the standard deviation is governed by its timing resolution. If the timing resolution of the APD is in the range of the lifetime of the emitter, the IRF can increase the value of $g^{(2)}(0)$ and broaden the anti–bunching dip (check subsection 3.2.4). I used two APDs with a minimum dead time of 25 ns and a single photon timing resolution of 350 ps (at 825 nm). The lifetime of emitters in hBN is a few nanoseconds, so the APDs resolution is enough to capture the single photon emission in my experiment. The intrinsic noise level of the detector, which corresponds to detection events with no photon present, known as dark count, can also increase the value of $g^{(2)}(0)$. The dark count of each APD is around 1500 counts/s. These APDs are connected to the time tagging device via SMA connectors. I mainly used the "high speed" mode of this equipment with a minimum of binning of 100 ps. To connect the time controller to the PC, I used a DAQ (USB–6210, National Instruments). Galvo's mirrors were controlled by another DAQ (USB–231, MCCDAQ) by applying ±10 V in the differential mode. LabVIEW was used to control the entire experiment, including applying analogue voltages to the galvo mirrors, controlling the sampling rate of acquired data by the time controller, etc. The spectrometer is connected to the PC with a USB connection to acquire the spectrum.

3.2.4 Single photon

As explained, the second–order correlation function measures the probability of observing the next photon after detecting the first photon at a delay time (τ) [101].

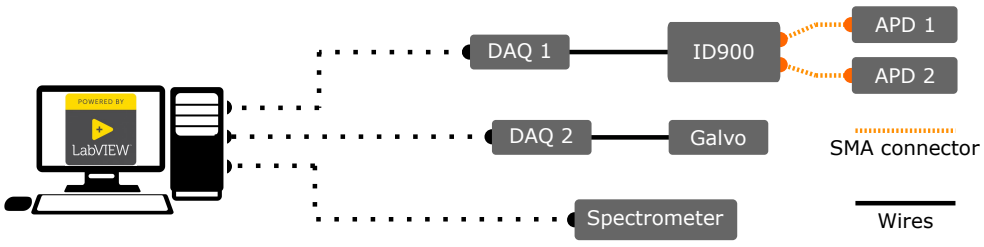

Figure 3.3: Electronic setup for the single photon characterisation at room temperature. LabVIEW controls the entire experiment. Two APDs are connected to the time controller, and the DAQ 1 (USB–6210) connects it to the PC. I used DAQ 2 (USB–231) to apply analogue voltages to the galvo's mirrors for scanning the sample. The spectrometer is connected to the PC with a USB connection to acquire the spectrum.

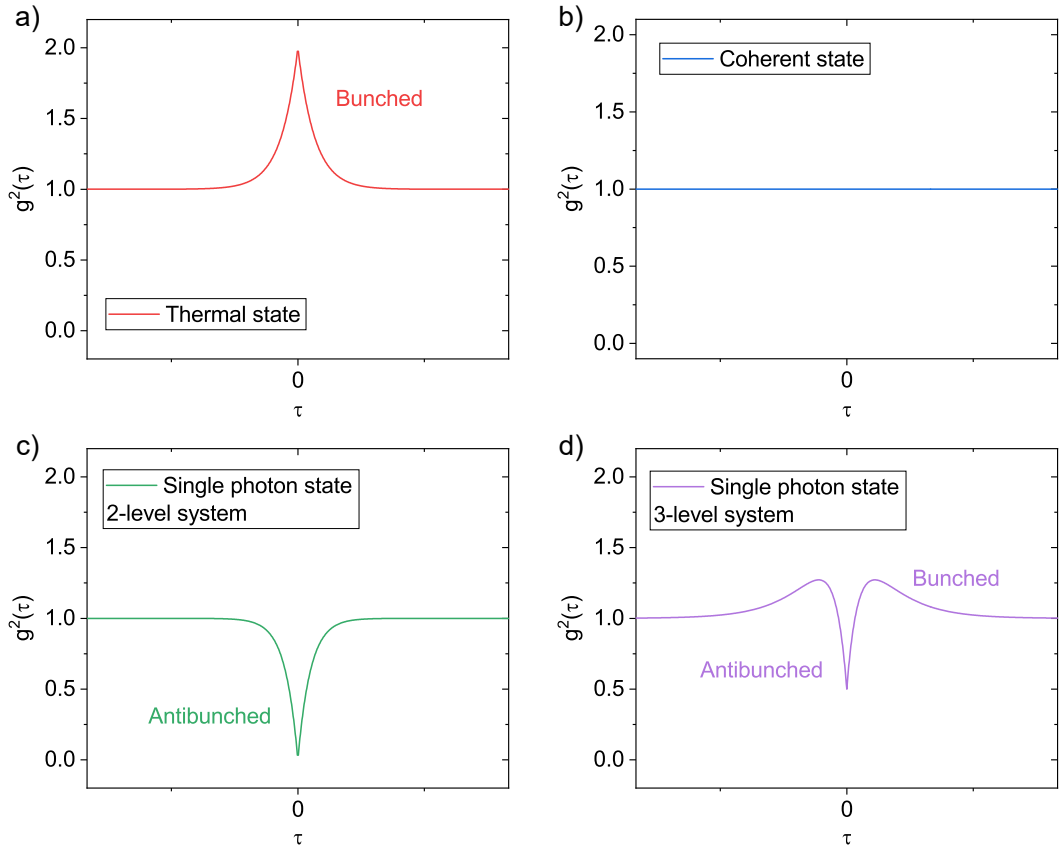

Figure 3.4: Second–order correlation function for three states as a function of the delay (τ). a) A thermal state, b) coherent state, and c,d) single photon state.

This function can be expressed by:

$$g^{(2)}(\tau) = \frac{\langle I(t)I(t+\tau)\rangle}{\langle I(t)\rangle\langle I(t+\tau)\rangle} \tag{3.1}$$

where $I(t)$ is the intensity of the detected light as a function of time. For a thermal source, such as lamps, the probability of detecting the subsequent photons at a small time delay is greater than 1. However, for a coherent source (like a laser), $g^{(2)}(t)$ always remains 1. These conditions are depicted in Figure 3.4.a and Figure 3.4.b, respectively. In contrast, for a single photon source, the second photons can be detected at longer delay times. Therefore, the $g^{(2)}(t)$ is less than 1 at a small time delay. This behaviour is known as "antibunching". A two–level system is the simplest example of a single photon source in which, after emitting the first photon, the electron returns to the ground state and needs to be excited again. Another example of a single photon source is a three–level system. Both these systems show antibunching behaviour at a small delay; the three–level system also shows bunching behaviour.

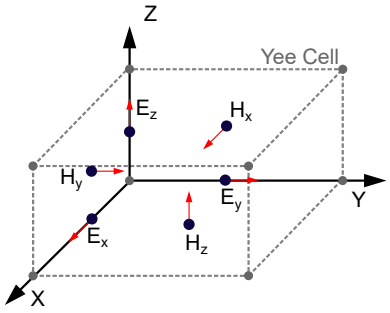

Figure 3.5: Yee Cell. This computational cell is the building block of the FDTD simulations, which represent spatial and temporal grids of electric and magnetic fields in three dimensions.

3.3 Simulation techniques

In Chapter 4, I primarily use Lumerical (Ansys) for FDTD simulation and MATLAB (MathWorks) for post–calculations. Due to the size of the simulations, I exploited the HAWK supercomputer. I acknowledge the support of the Supercomputing Wales project, which is part–funded by the European Regional Development Fund (ERDF) via the Welsh Government. In what follows, I discuss the methods used in the simulation chapter.

3.3.1 Finite–difference time–domain (FDTD)

Lumerical FDTD solution is an FDTD–based software that solves Maxwell's curl equations in non–magnetic materials, which include:

$$\frac{\partial \overrightarrow{D}}{\partial t} = \nabla \times \overrightarrow{H} \tag{3.2}$$

$$\overrightarrow{D}(\omega) = \varepsilon_0 \varepsilon_r(\omega) \overrightarrow{E}(\omega) \tag{3.3}$$

$$\frac{\partial \overrightarrow{H}}{\partial t} = -\frac{1}{\mu_0} \nabla \times \overrightarrow{E} \tag{3.4}$$

Where E, H and D are the electric, magnetic, and displacement fields, respectively. In addition, ε_0, μ_0 and ε_r are the vacuum permittivity, vacuum permeability, and relative permittivity. In a three–dimensional (3D) space, Maxwell equations have six electromagnetic field components: (E_x, E_y, E_z) and (H_x, H_y, H_z). To solve these equations, the FDTD method comprises computational arrays of three–dimensional units known as "Yee cells", which represent spatial and temporal grids at field components (electric and magnetic fields in three dimensions) that need to be solved [102]. Figure 3.5 depicts the Yee cell. The size of the Yee cell can be defined by the rectangular and cartesian style mesh size. In all simulations, I discretised the entire simulation region with auto non–uniform mesh size. I also used the mesh override

option to define new mesh settings for areas requiring fine mesh steps.

Figure 3.6 illustrates a 3D view of the structure with snapshots of three cross sections. In this figure, the simulation region (i.e. FDTD region) can be seen by the orange colour box, whose size sets as 30×30×2 µm^3. Simulation memory and time scale up with $1/dx^3$ and $1/dx^4$ ratios, respectively. To minimise allocated resources in each simulation, boundary conditions must be set correctly. Symmetries in geometry, mesh, monitors, and source are critical factors for choosing the correct settings for boundary conditions. Bullseye cavity structure defined in Chapter 4 and mesh are symmetric along XY–plane. I modelled a single quantum emitter as an in–plane dipole with an emission wavelength of around λ =750 nm. Because the monitors I used in these simulations are all 2D monitors, the dipole direction is the only critical factor in determining boundary conditions. According to the XZ–cross section in Figure 3.6, the electric field (blue double arrow) is symmetric along the x–axis; therefore, I set the x–axis boundary condition as "symmetric". However, the dipole is asymmetric along the y–axis based on the YZ–cross section in Figure 3.6. So, I selected the y–axis boundary condition as "Asymmetric". Symmetric and asymmetric axes boundary conditions are shown as blue and red, respectively.

Except for the bottom boundary condition (i.e. Z–min), all boundary conditions are set as perfectly matched layer (PML). PML is an absorbing and impedance–matched layer that absorbs incident lights without minimal reflections. For the Z–min, metal was selected as a boundary condition. Because my design

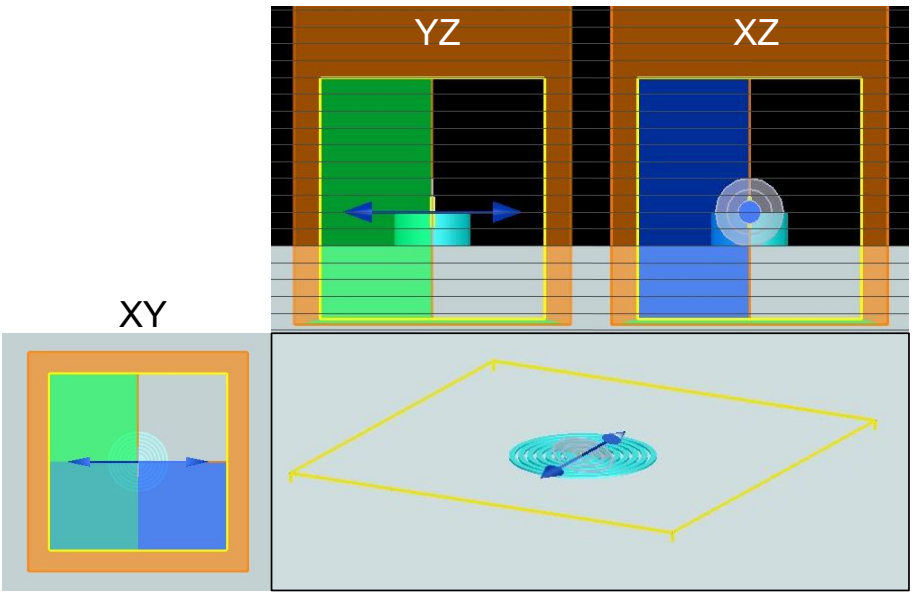

Figure 3.6: Simulation region. A 3D view of the simulation region with XY, YZ, and XZ cross sections. The bullseye Bragg cavity structure is at the centre of this region. The blue double arrow indicates the dipole, which represents the quantum emitter. Symmetric and asymmetric axes boundary conditions are shown as blue and red, respectively.

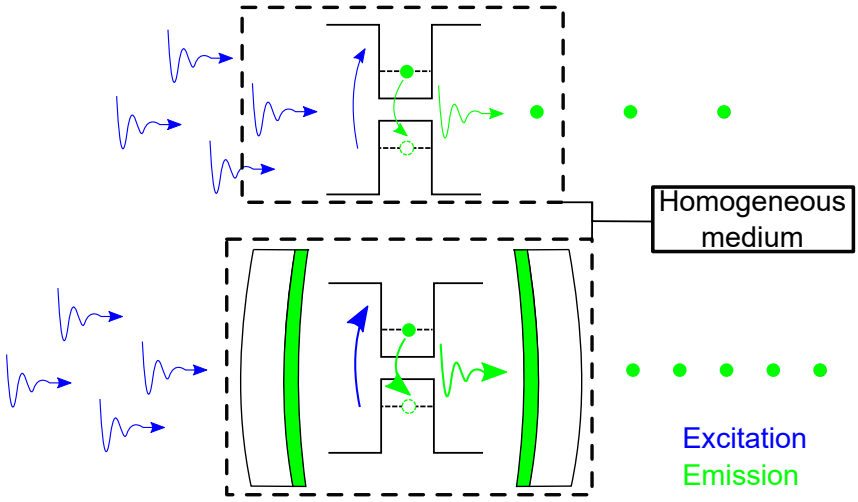

Figure 3.7: Purcell factor. The top image shows a two–level system inside a homogeneous medium. When the two–level system is placed inside a cavity, the radiative decay rate of the system increases. This situation is depicted in the bottom image. The blue wavy arrows illustrate excitation photons, and the green circles show emission photons. The bigger size of arrows inside the cavity shows a higher intensity of excitation and emission. In a lossless and homogeneous medium, the radiative decay rate enhancement is equivalent to the Purcell factor.

consists of a gold layer as a reflecting material, choosing a metal boundary condition guarantees the same performance but with less simulation run time. Using this principle, I reduced the simulation volume and time by a factor of 4.

3.3.2 Purcell factor

The Purcell factor is defined as the emission rate enhancement of a spontaneous emitter inside a cavity. The formula that explains this relationship is given by [103]:

$$F = \frac{\tau_{free}}{\tau_{cavity}} \tag{3.5}$$

In a lossless material, the Purcell factor is equivalent to the radiative decay rate enhancement, defined as the ratio between the power injected into the simulation region by the dipole source and the power of the dipole source would radiate in a homogeneous medium. Because I used fine mesh around the dipole, I defined a small box of transmission monitors surrounding the dipole source to calculate the power injected into the simulation region. The refractive index of TiO_2 at 750 nm only has a real component ($n_{TiO_2} = 2.268$); therefore, the above definition can be applied to the Purcell factor. For other materials, the refractive indices are taken from the software's built–in material database. Purcell factor is depicted in Figure 3.7.

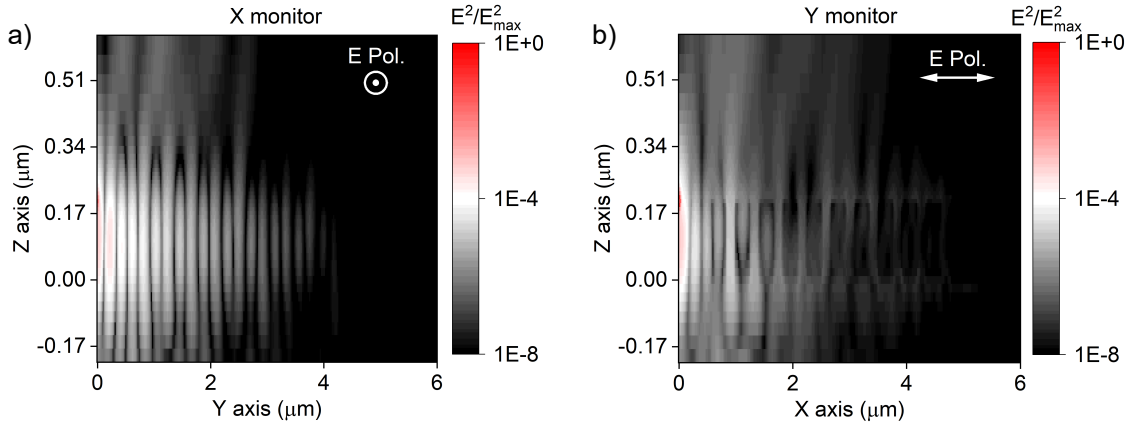

Figure 3.8: The normalised electric field intensity for the bullseye structure. a) In this near–field cross–section, the dipole is normal to the YZ plane and located 1 nm above the bullseye surface. b) The XZ plane near–field cross–section for the same structure as described in (a)

3.3.3 Collection efficiency

In this work, I defined the collection efficiency as the fraction of the optical power generated in the cavity that escaped into the air above the cavity and coupled to an objective lens. To achieve this, I first calculated the power emitted to a monitor that captures near–field emission; then, I calculated the near–field to far–field projection. Finally, I integrated the far–field power over the collection window defined by the NA of the objective lens in the system (= 0.68). In this work, I studied the bullseye Bragg grating structure. A Bullseye structure with periodic gratings improves the collection efficiency of a dipole into the objective lens. In Figure 3.8, a near–field cross–section of the normalised electric field intensity for the studied structure is shown. The dipole is located 1 nm above the bullseye surface in this figure. This structure will be discussed in Chapter 4.

3.4 Defect generation techniques

In the section, I discuss the methods used in Chapter 5. In what follows, I first describe the exfoliation of hBN flakes on substrates. Next, I elaborate on the techniques I utilised to generate defect centres in hBN. These consist of plasma/annealing treatment, annealing and irradiation approaches.

3.4.1 Exfoliating of hBN flakes on substrates

Since discovering monolayers of 2D materials, the mechanical exfoliation method is still the primary method in academia [104]. By using scotch tape, it is possible to peel off these layers, which attach by van der Waal forces one by one and finally

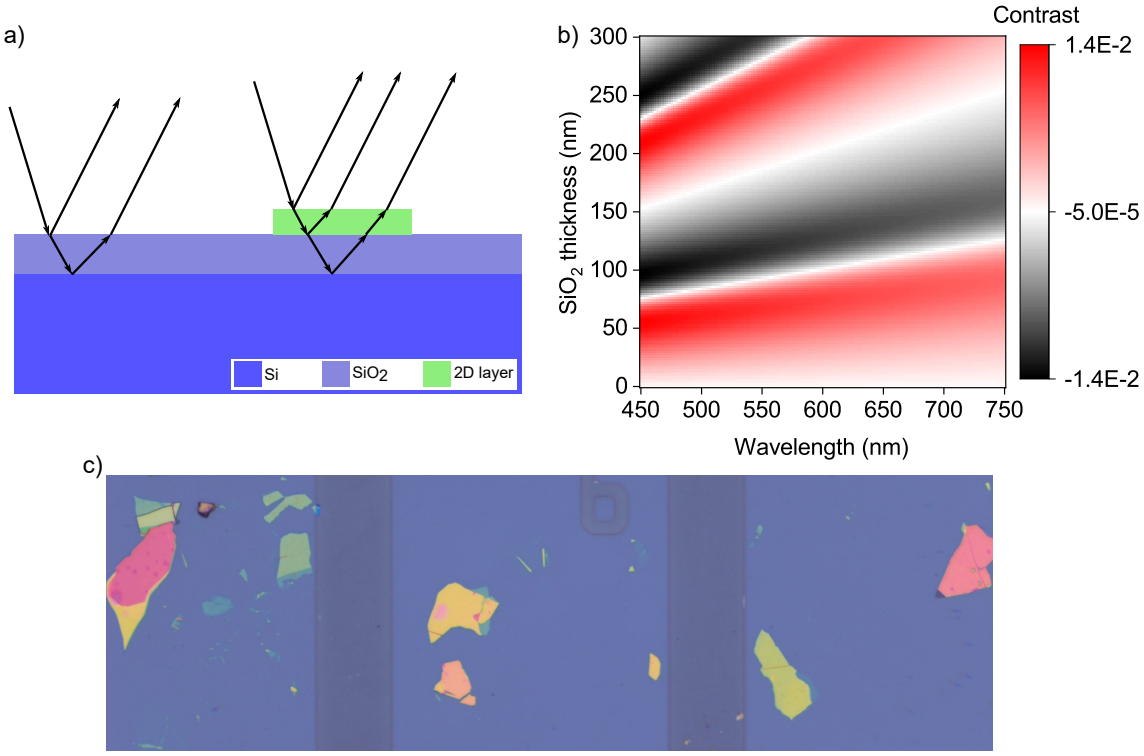

Figure 3.9: Visibility of layered materials. a) Schematic depiction of optical reflection and transmission for nanolayer. b) Colour plot of calculated contrast as a function of incident light wavelength and SiO_2 layer thickness for hBN. c) An optical microscopy image of exfoliated hBN flakes on SiO_2

achieve a single layer of the material with a thickness of atoms called 2D material [104]. This method has some benefits, such as being quick and low cost; however, it has some disadvantages, including small flakes and low reproducibility. To exfoliate a monolayer of 2D material, blue scotch tape (Plastic Film, SPS Europe) was utilised. Two hBN crystals were used in this work; the first one was purchased from HQ Graphene, and Prof's Takashi Taniguchi and Kenji Watanabe (National Institute for Materials Science) provided the second one. Before exfoliating the hBN crystal, the surface of the substrates was cleaned in the O_2 plasma ash (50 W, 1 min). SiO_2/Si wafers (Ossila) were used as substrates.

To start, a piece of clean tape was cut. Then this piece was attached to the bulk 2D crystal. After detaching the bulk crystal from scotch tape, both sides of the tape (the one with the 2D flakes and the clean one) were brought together. In the next step, using a cotton swab, a slight pressure was uniformly applied to the scotch tape. Then, the two sides of the scotch tape were pulled away from each other. Finally, the tape were attached to the SiO_2/Si sample and detached slowly. After making the sample, the next step is to find the desired flake.

As flakes with various thicknesses have different optical contrast, they have distinct colours under the microscope. The contrast between 2D layers and the un-

derlying layer (in this work, mainly 300 nm SiO_2) is due to the phase shift of the interference colour and the material opacity. Figure 3.9.a shows a schematic depiction of optical reflection and transmission for nanolayer structures on top of the SiO_2/Si substrate [105]. The angle of incident and reflected light in Figure 3.9.a is exaggerated. By considering the nanolayer as a thin homogeneous 2D film and a normal light incident, it is possible to derive the formula for the intensity of reflected light and calculate the contrast, which is the relative intensity of reflected light in the presence and absence of nanolayers [105, 106]. Figure 3.9.b illustrates the relation between the wavelength and thickness of SiO_2 for hBN. To calculate this, the refractive indices of hBN, SiO_2 and Si are considered to be constant [105–107]. In this work, I am using 300 nm SiO_2. Figure 3.9.c shows an optical microscopy image of exfoliated hBN flakes on SiO_2. To facilitate finding flakes, I etched SiO_2 to fabricate a 90 nm grid structure.

3.4.2 Plasma and annealing involved method

I utilised cleanroom facilities in the institute for compound semiconductors (ICS) to generate defect centres in the hBN crystal lattice. For the following studies, I elaborated recipes I used:

- **Plasma/annealing treatment** approach: Samples were treated in O_2 reactive ion etching (RIE), N_2 rapid thermal annealer (RTA) and O_2 plasma ash in order. hBN flakes were etched at 225 mTorr for 1 min under 100 W plasma power, with 100 standard cubic centimetres per minute (sccm) oxygen in PlasmaPro 80 RIE (Oxford Instruments). Following that step, samples were annealed for 30 min in the environment filled with N_2 in Jipelec Jetfirst 300 (ECM). The annealing temperature and time were set to 600 °C and 30 min, respectively. Finally, the O_2 plasma ash was used to clean the sample's surface. Plasma ash is typically used to clean the surface of samples from contaminants and resist leftovers during the fabrication steps; however, it was observed that the plasma ash helps to reduce background fluorescence from the samples. For this step, 100 W plasma power for 10 min under 40 sccm oxygen flow was used in Plasma Etch PE–75 (Plasmaetch).
- **Annealing** approach: In the consecutive annealings at medium temperature (check subsection 5.6.1), the recipe and the equipment are the same as the treatment approach; however, I tested three different temperatures on one sample, 400 °C, 500 °C, and 600 °C, to compare their impacts on a single flake. For the single annealing at high temperatures (check subsection 5.6.2), I used Jipelec Jetfirst 100 (ECM) due to its capability to reach higher temperatures. In this study, I annealed different samples at 875 °C, and 1000 °C, both for

8 min.

- **Fluence study** in irradiation approach: After studying irradiated samples with different fluences, first, I annealed these samples at 875 °C for 8 min in the N_2 environment. Next, I used Plasma Etch PE–75 for 3 min at 30 W to clean the samples, and more importantly, decrease the fluorescence background from the substrate.
- **Energy study** in irradiation approach: After studying irradiated samples with different energies, I only annealed these samples at 800 °C for 30 min in the N_2 environment.

3.4.3 Kr irradiation method

Samples in Section 5.7 were irradiated with an ultra–low energy Kr ion implantation system [108]. Before irradiation, samples were annealed at 220 °C for 30 min in an ultra–high vacuum environment (around 10^{-7} mbar). For the subsequent studies, different settings were used:

- **Fluence study**: For this study, all samples were irradiated with identical ion energy (25 eV) but with different fluences, including 10^{11} cm^{-2}, 10^{12} cm^{-2}, 10^{13} cm^{-2}, and 10^{14} cm^{-2}. In addition, a reference sample without any irradiation was fabricated to facilitate comparing results.
- **Energy study**: After selecting a suitable fluence based on the previous study (10^{12} cm^{-2}), samples were irradiated at different energies. These energies were 50 eV, 100 eV, 150 eV, and 200 eV. Likewise, a reference sample without irradiation was fabricated to facilitate comparing results.

3.5 ODMR experiment

To characterise the spin qubit and unravel its spin properties, we performed the ODMR experiment. In what follows, I elaborate on the tools we used to implement this experiment.

3.5.1 Sample

The sample in this work was fabricated in Isaac Luxmoore's group at Exeter University and implanted at the University of Surrey Ion Beam Centre. The sample consists of a chromium/gold (20/100 nm thick) co–planar waveguide (CPW), with a 10 µm wide central conductor, on a sapphire substrate. An hBN flake, approximately 100 nm thick, obtained by mechanical exfoliation from bulk crystal, is placed on top of the CPW using the Polydimethylsiloxane standard dry transfer method.

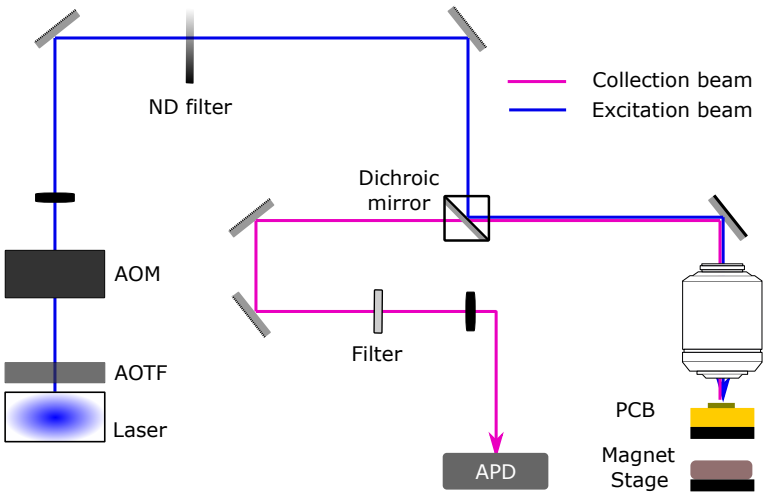

Figure 3.10: Room temperature optical setup to study ODMR. Laser excitation, after passing through the pinhole, is redirected toward the objective lens via broadband dielectric mirrors and a dichroic mirror. An neutral–density filter is used to limit the excitation power. A long working distance objective lens with NA=0.8 was used to focus light to a diffraction–limited spot. The output beam is redirected toward fibre–coupled APD by passing through broadband dielectric mirrors and a pinhole. A long–pass filter is used to limit the wavelength range of the output beam.

Boron vacancies are generated/activated using C–ion implantation with an energy of 10 keV and a dose of 1×10^{14} cm^{-2} [100].

3.5.2 Optical setup

As depicted in Figure 3.10, the optical setup consists of a home–built confocal microscope located at Exeter university. A Nikon objective lens with a long working distance with NA= 0.8 is used to focus coupled laser light to a diffraction–limited spot (1 µm in diameter). The sample is mounted on an XY–piezoelectric stage in the microscope's focal plane. The piezoelectric stage is controlled by its company–developed software (Physik Instrumente). Different laser sources were used depending on the study to excite the ensemble of V_B^- centres; for the continuous wave (CW) experiment, diode–pumped solid–state lasers at 488 nm (LP488–SF20, Thorlabs) or 532 nm (LDC200C series, Thorlabs) wavelengths were used. For pulsed ODMR, I utilised broadband super–continuum laser that an acousto–optic tunable filter has filtered to give a ∼1 nm bandwidth, 80 MHz repetition rate, and a pulse width of ∼5 ps. To make the CW laser on and off during pulsed ODMR or adjust the repetition rate (i.e. on/off) of a pulsed laser, an acousto–optic modulators (AOM) switch was used. The AOM works as a pulse–picker. By blocking the laser, I am allowed to apply the microwave (MW) signal. V_B^- centres emitted fluorescence (∼ [690–950] nm) collected from the same objective lens and isolated from the excitation laser by a dichroic mirror. An additional 750 nm long–pass

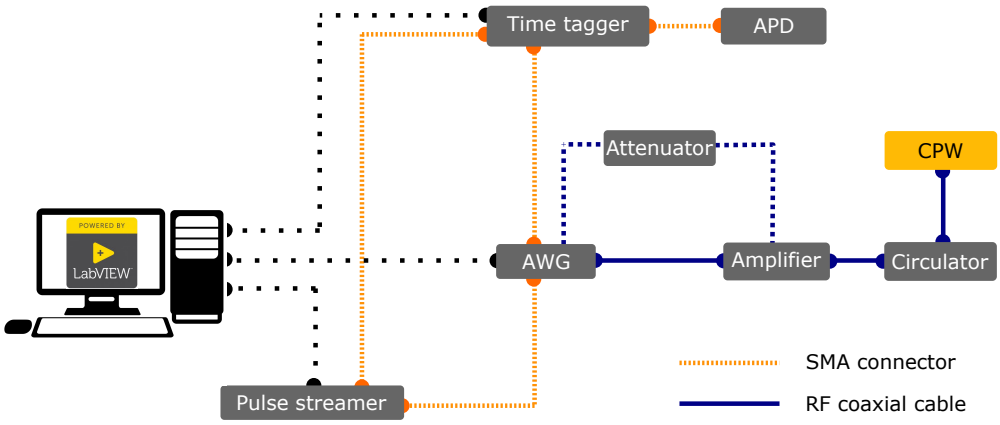

Figure 3.11: Room temperature MW and electronic setup. MW signals generated by AWG are sent to CPW through an amplifier and circulator. An attenuator is used when it is needed to attenuate signals to avoid damaging the amplifier. PL intensity detected by APD is counted in the time tagger. Pulse streamer synchronises AWG and time tagger. All equipment is controlled by programmes written in LabVIEW.

filter is used to suppress unwanted signals further. The output beam was fibre coupled to time–correlated single–photon avalanche diode (SPCM–AQRH, Excelitas) through the output pinhole. This allows us to count photons and perform time–resolved spectroscopy with a time–tagging module (Time tagger 20, Swabian instruments).

3.5.3 Microwave and magnet setup

Coherent control of the electron spins in V_B^- demands applying the MW field to the sample. An in–plane AC magnetic field is generated through an impedance–matched CPW using a microwave waveform generated by arbitrary waveform generator (AWG). The highest sampling rate of AWG was 65 GSa/s to obtain the highest possible resolution (M8195A, Keysight). Digital waveforms are built in LabVIEW and generated in the AWG. Output analogue signals get the following form:

$$V_{MW} \cos\left(\omega_{MW} t + \delta_{MW}\right) \tag{3.6}$$

where V_{MW} ($0 \leq V_{MW} \leq 1$ V), ω_{MW}, and δ_{MW} identify MW amplitude, frequency and phase, respectively. Generated signals are amplified (30 dB amplification, maximum output power 30 dBm) and applied to the CPW on the sample. A circulator was used to isolate the amplifier from unwanted reflection noise from the sample (Pasternack). Due to the limited working frequency of the amplifier, in some experiments, I used an attenuator (10 dB, Pasternack) between AWG and the amplifier to avoid damaging the amplifier.

To apply an out–of–plane DC magnetic field, a permanent magnet is mounted on

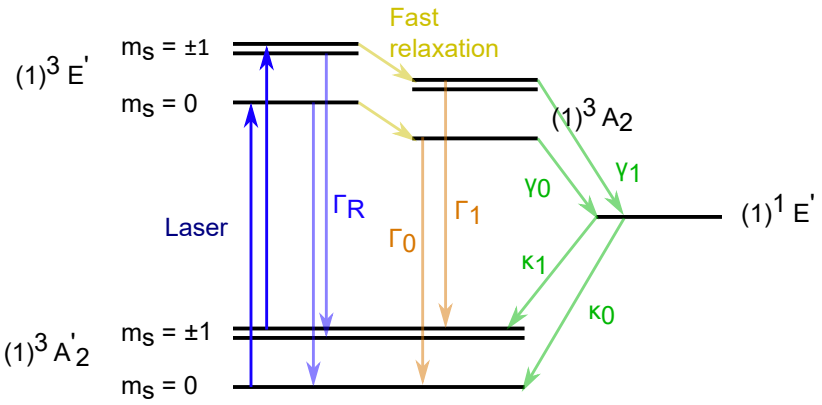

Figure 3.12: The ladder diagram for the V_B^-. Energy level diagram of the defect. (Re–plotted from ref. [100, 110])

a dual–axis manual goniometer (THORLABS) on top of a z–directional stage below the sample. By moving the translational stage in the z direction, I tune the static magnetic field from 0 and 200 mT. Goniometers were used to rotate the static magnetic field with respect to the defect–sample normal plane. A pulse streamer is used to synchronise optical, MW excitation, and photon collection (Pulse Streamer 8/2, SWABIAN INSTRUMENTS). By triggering from the pulse streamer, the AWG is synchronised to the rest of the experiment. Also, there is a dedicated hardware connection between the PC and AWG. LabVIEW was used to control transistor–transistor logic pulses (generated by a pulse streamer), create digital waveforms in AWG, and enable the readout and count mechanism in the time tagger. Figure 3.11 illustrates a schematic of the MW and electronic connection of this setup.

3.5.4 Spin initialisation

While optical excitation excites optical transitions, MW frequency under a magnetic field addresses electron spin transitions. The fluorescence from a spin defect under such conditions differs from that without MW excitation. The fluorescence difference is known as ODMR contrast, which is the basis of optically detected magnetic resonance. Unpolarised non–resonant light excites both $m_s = 0$ and $m_s = \pm 1$ optical transitions. However, optically excited electrons in these states undergo two possible decay mechanisms:

- Bright transition: they radiatively decay into spin–triplet GS. This spin–conserving mechanism is higher for the $m_s = 0$ spin sublevel.
- Dark transition: they are the non–radiatively shelved into the metastable singlet state through intersystem crossing (ISC). This will happen possibly due to spin–orbit coupling like NV centre. This mechanism is a higher likelihood for electrons with $m_s = \pm 1$ spin sublevels [109].

These mechanisms are shown in Figure 3.12. After a few optical cycles, more electrons will polarise back into the $m_s = 0$ spin state. This includes ISC from the singlet to the ground triplet state that occurs via coupling to phonons; this is a spin–dependent but non–spin preserving relaxation process. Because of this mechanism, the $m_s = \pm 1$ state produces, on average less PL than the $m_s = 0$ state [63, 100, 111]. This behaviour resembles what happens in SiC and NV centres in Diamond [112, 113].

At thermal equilibrium and when the laser is off, or it has been off after an experiment for a long time (much longer than T_1), electron spin is in a mixed state. When the laser is illuminating the defect centre, the electron spin is pumped preferentially into one state, resulting in (partial) spin preparation. It is shown experimentally that the electron spin initialisation time is around 100 ns for the V_B^- centre at high laser power (200 µW), but at low laser power, it is higher than this value; the spin initialisation time can be reduced at low laser power if the defect centre is close to metal contact/waveguide [114]. Notably, a spatially extended ensemble of defects requires longer initialisation times than single defects typically [113]; that is because, at the rim of the Gaussian illumination profile, the intensity of the laser is about 1/10 of what is in the centre of the beam, which results in the non–uniformity in optical intensity [115]. In this work, to prepare electron spin in the $m_s = 0$ state as a reference, I apply a 2000 ns laser pulse close to what was used in other works [114, 116].

3.5.5 Bloch sphere and Bloch vector

Each state of a microscopic system is represented by a vector in an abstract Hilbert space. The Hilbert space of a two–level system is mirrored onto the Bloch unit–sphere, each of its points representing a possible superposition of states (for example, $|0\rangle$ and $|1\rangle$) [117]. The $|0\rangle$ and $|1\rangle$ states correspond to the south and north poles, respectively. A representation of the Bloch sphere is shown in Figure 3.13. The vector that locates points on the Bloch sphere is called the Bloch vector, and it is defined:

$$\mathbf{S} = (\cos\varphi \sin\theta, \sin\varphi \sin\theta, \cos\theta) \tag{3.7}$$

Using the Bloch vector, an arbitrary state in the two–level system can be written as a superposition of $|0\rangle$ and $|1\rangle$ states:

$$|\psi\rangle = c_{|0\rangle}(t)\,|0\rangle + c_{|1\rangle}(t)\,|1\rangle \tag{3.8}$$

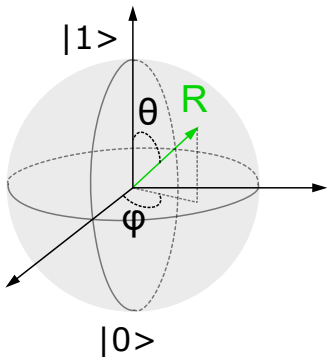

Figure 3.13: Bloch sphere. The Hilbert space of a two–level system is mirrored onto the Bloch unit–sphere, each of its points representing a possible superposition of states (basis states are $|0\rangle$ and $|1\rangle$).

where $c_{|0\rangle}$ and $c_{|1\rangle}$ are the probability amplitude of state $|0\rangle$ and $|1\rangle$ at the time t, respectively. To have a pure quantum state, below condition should be met:

$$c^2_{|0\rangle}(t) + c^2_{|1\rangle}(t) = 1 \tag{3.9}$$

Therefore, I can simplify the state vector to (neglecting global phase):

$$|\psi\rangle = \sin\frac{\theta}{2}|0\rangle + e^{i\varphi}\cos\frac{\theta}{2}|1\rangle \tag{3.10}$$

In above formula, the polar angle θ defines the relative probability amplitude between two state $|0\rangle$ and $|1\rangle$. In contrast, the azimuthal angle ϕ reveals the phase difference between $|0\rangle$ and $|1\rangle$ states.

In this work, V_B^- centres were studied under a static magnetic field with sufficiently high magnitude to selectively address the $m_s = |0\rangle \leftrightarrow |1\rangle$ transition. Therefore, V_B^- centres can be considered as an effective two–level system. In addition, I utilised a microwave source to apply an oscillating magnetic field to the system for manipulating the spin. The frequency difference between the microwave source and the two–level system controls the polar angle of spin's rotation axis ($\theta = 90°$ for no detuning). Furthermore, the phase of microwave source determine the azimuthal angle of the rotation axis ($\phi = 0°$ for no phase). In Chapter 6, I will discuss how the pulse area can be used to rotate the spin vector on the Bloch sphere.

3.6 Discussion

In this chapter, I discuss the experimental tools and computational methods that I used in this work. In Chapter 4, I use computational methods described in Section 3.3 to design a bullseye cavity structure. In Chapter 5, I use recipes explained in Section 3.4 to create defect centres in hBN and utilise experimental methods

illustrated in Section 3.2 to characterise them. Finally, we use tools and concepts discussed in Section 3.5 to study V_B^- in Chapter 6.

CHAPTER 4

Bullseye dielectric cavity for optimised photon collection from point sources

4.1 Introduction to Bullseye dielectric cavities

Controlling the emission characteristics of an emitter in a solid–state system is a crucial case in quantum computing and quantum communication [49, 118]. Characteristics of the source, such as the photon collection efficiency and the emitter decay rate, are two vital parameters. Various approaches have been utilised in different systems to enhance these parameters during the past few decades. Bullseye–shaped circular Bragg grating micro–cavities attract considerable attention due to their unique properties [52, 54, 119, 120]. Due to its rotational symmetry around the z–axis, the structure is not sensitive to the orientation of the in–plane emitter. The structures are proposed based on the second–order Bragg condition that allows efficient directionality of light, resulting in higher light extraction [121]. So far, cavities in reported bullseye structures are mainly dielectric–based and lossless. It is an essential advantage over other systems such as plasmonic cavities as it results in near–unity quantum efficiency (apart from the emitter intrinsic quantum efficiency) [122–124]. Recently, a hybrid structure based on bullseye structure has been reported in which high Purcell factor over a broad range of wavelengths with high collection efficiency is achieved [125]. Inspired by the bullseye pattern, defects in photonic crystals in the bullseye arrangement were recently proposed as a new platform for extremely high Purcell factor with high collection efficiency [126]. Bullseyes have been utilised for quantum dots [127], defect centres in diamond [128, 129], and in two dimensional (2D) materials [54, 58]. In recent reports [51], collection efficiency near unity is achieved by utilising a low refractive–index dielectric (SiO_2) layer and a layer of gold as the mirror at the bottom of the structure.

In this chapter, I demonstrate an approach to designing a bullseye structure to study the enhancement of optical properties of WSe_2 on this structure. The structure features high collection efficiency ($> 80\,\%$) and high Purcell factor (> 22.5) at the wavelength of resonance ($\sim 750\,\mathrm{nm}$). After designing the structure, the coupling condition between the emitter and the cavity is discussed. This analysis signifies the importance of positioning in emitter–cavity systems. In the next step, the efficiency of the coupling is studied. Finally, I applied the concept of apodization to the structure to achieve higher collection efficiency into the fibre.

4.2 Theoretical background

The whole structure in this work consists of a gold–coated silicon wafer (5 nm chromium, 150 nm gold), which has a spacer layer of SiO_2 (435 nm thick) and a TiO_2 layer. We received these samples from our collaborator, Alex Clark. There are a couple of considerations for choosing the number of layers and materials; For grating structure, dielectric materials with high refractive index offer better cavity and reflectivity (or, in the case of grating, mirror strength) at visible wavelength. In addition, a layer of gold can provide extra directionality. From a fabrication perspective, an intermediate membrane is needed to act as a spacer between these two layers (a grating layer made of a dielectric and gold layer). Also, the spacer prohibits horizontal emission from quenching (in case of interfering with the gold layer) [53]. To have constructive interference between vertical emission and its reflections, the initial thickness of this spacer layer can be considered $\lambda_{eff}/2$, where λ_{eff} is the effective wavelength inside the spacer layer [130]. The thickness of the spacer layer (SiO_2) is defined as h_{SiO_2}.

The circular Bragg grating consists of a series of concentric rings centred around a disk with a radius of R_{TiO_2} all made from TiO_2. The width of each ring is W_{TiO_2} and the distance between two consecutive rings is W_{Air}. Because of the inherent rotational symmetry of the structure to its normal, it is easier to consider a 2D model of the structure. Figure 4.1.a shows a cross–section of the structure. In this respect, the 2D lateral unit cell in the real space (or periodicity of the structure) can be defined as the sum of the width of each ring and the gap between two consecutive rings. Therefore, I have:

$$\Lambda = W_{TiO_2} + W_{air} \tag{4.1}$$

In order to satisfy the second–order Bragg condition for efficient vertical light extraction, the grating period is $\Lambda = m\lambda/2n_{TE}$ [121, 131]. This condition guarantees that vertical emission and reflected out–coupled light interfere constructively (phase–matched). As a result, higher intensity mode can be collected in the far field. In this formula, m, λ and n_{TE} are integer constant ($m = 1$), the resonance wavelength and the effective transverse electric (TE) mode index propagating inside the slab, respectively. This formula is valid when grating's etch depth (h_{Air}) is not considerable compared to grating height ($h_{TiO_2} = \lambda/2$). As explained in [131], a fully etched grating provides better overlap of the guided field inside the slab and the etched region, higher guided wave reflectivity, and higher quality factor, which the last item guarantees higher Purcell factor. Therefore, $\Lambda = \lambda/n_{TE}$ is considered as the initial value for the grating period.

To limit the mode inside the slab, the initial thickness of the slab-grating is set

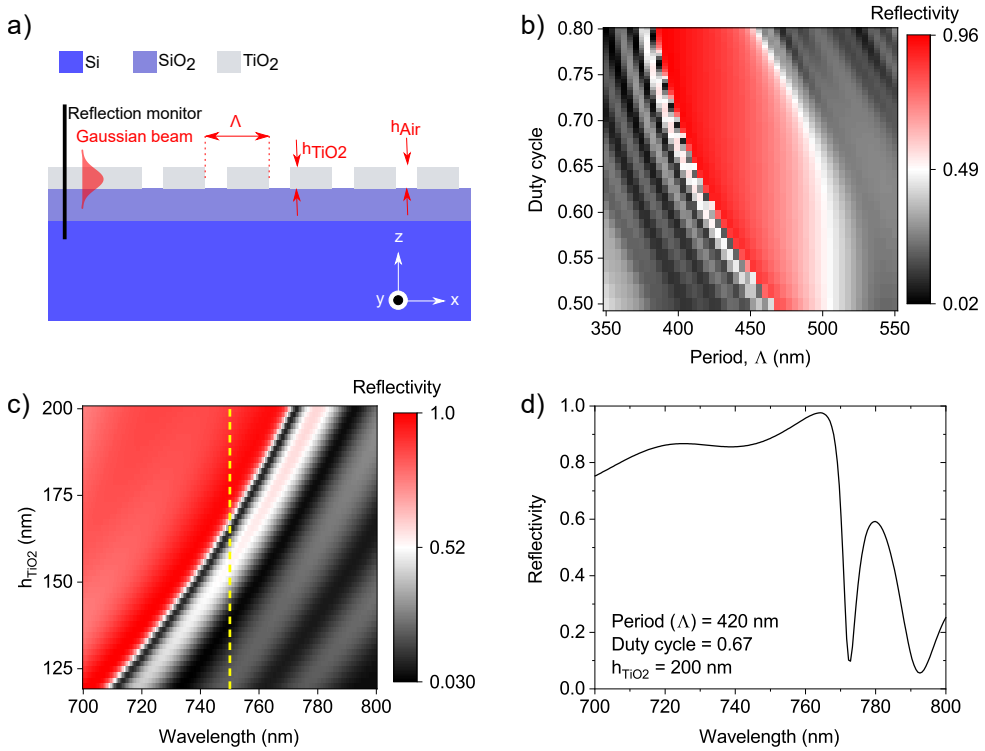

Figure 4.1: 2D simulation of periodic structure approximating the cross–section of the Bullseye. (a) cross–section of the bullseye structure. (b) The reflectivity for a fixed a wavelength (750 nm) as a function of the period of the structure and the duty cycle. (c) The reflectivity as a function of thickness and the wavelength of the excitation for $\Lambda = 420\,\text{nm}$ and $W_{TiO_2}/W_{Air} = 2$ (d) The reflectivity as a function of the wavelength of the excitation for $\Lambda = 420\,\text{nm}$, $W_{TiO_2}/W_{Air} = 2$, and $h_{TiO_2} = 200\,\text{nm}$.

to $h_{TiO_2} = \lambda/2$. The grating effectively acts as a mirror, and each component has a unique mirror strength. Thus, the band edge was studied to find the geometries for designing a 2D Bragg grating structure. In this study, a TE Gaussian mode was injected from the slab side to the structure, and the reflection of the grating was studied via a transmission monitor behind the excitation source (Figure 4.1.a). The reflectivity for a fixed a wavelength (750 nm) as a function of the period of the structure and the duty cycle is plotted in the Figure 4.1.b. Duty cycle is defined as W_{TiO_2}/Λ. I chose period and the duty cycle as 420 nm and 0.67, respectively, based on this result.

The thickness of the top layer, i.e. h_{TiO_2}, is the next parameter to study. Figure 4.1.c illustrates the reflectivity as a function of thickness and the excitation wavelength. I select the thickness only to allow single TE mode to propagate inside the slab (or later cavity). Depending on the actual position of the emitter, h_{TiO_2} should be chosen carefully. If the emitter is located inside the layer, for instance, a QD or a defect in a wide bandgap material, the thickness should be selected in a way to support TE_0 (or TE_1) mode; however, if the emitter is located close to

the boundary of the top layer, like emitters in 2D material, TE_2 mode is a better option [58]. On the other hand, allowing more than one mode to be guided (Like TE_2, above sentence) reduces the spontaneous emission factor. I will discuss this parameter later. Figure 4.1.d depicts the reflectivity for $\Lambda = 420\,\text{nm}$, $W_{TiO_2}/W_{Air} = 2$, and $h_{TiO_2} = 200\,\text{nm}$. I consider these values as initial values in the next step.

4.3 Cavity design

A 3D view of the structure is depicted in Figure 4.2.a. The emitter is considered to be 1 nm above the surface of the bullseye at its centre. In the simulation, the emitter is modelled as a dipole. This type of structure features high directionality of the emitted light from an emitter positioned in the centre of the structure or, in this case, 1 nm above the surface of the bullseye at its centre. To quantify the directionality, collection efficiency can be defined, and it is the fraction of the total dipole power that the collection optics can collect. In the simulation, collection optics are modelled as an objective centred on the cavity with NA = 0.68. The gold layer acts like a mirror that helps to redirect back-lobe emission toward the +z direction.

Reported values for spontaneous emission rate enhancement in the literature for the bullseye structures are between 1 and 56 [52, 132]. In the proximity of dielectric cavities, the loss is considered to be negligible; therefore, the spontaneous emission rate enhancement is equal to the Purcell factor [133]. From the experimental point of view, the Purcell factor quantifies the reduction of the excited state's lifetime [134]; however, in simulation, the ratio of the total radiated power of the dipole inside the cavity is divided by the same parameter for the dipole in an uniform dielectric (homogeneous medium, reference) is considered to calculate the Purcell factor.

At this step, a couple of considerations must be taken into account; first, to increase the spontaneous emission rate enhancement, it is necessary to maximise the total electric field in the area of the structure where the emitter is positioned. This part can be achieved primarily by designing the disk dimensions in the emission wavelength of the emitter. For the initial guess, I started with $2R_{TiO_2} = n_{TiO_2}\lambda_{res}$. In order to achieve higher collection efficiency, I can use parameters derived from the 2D design analysis. Therefore, I can consider $\Lambda = 420\,\text{nm}$, $W_{TiO_2}/W_{Air} = 2$, and $h_{TiO_2} = 200\,\text{nm}$ as my initial guess for these parameters. By sweeping the central disk parameter and the duty cycle as a function of the wavelength, I can optimise the structure geometry to achieve higher Purcell factor and collection efficiency.

Figure 4.2.b and Figure 4.2.c (Figure 4.2.d and Figure 4.2.e) show the Purcell factor (the collection efficiency) as a function of duty cycle and central disk as x–axis and wavelength as y–axis, respectively. The structure is designed for approximately

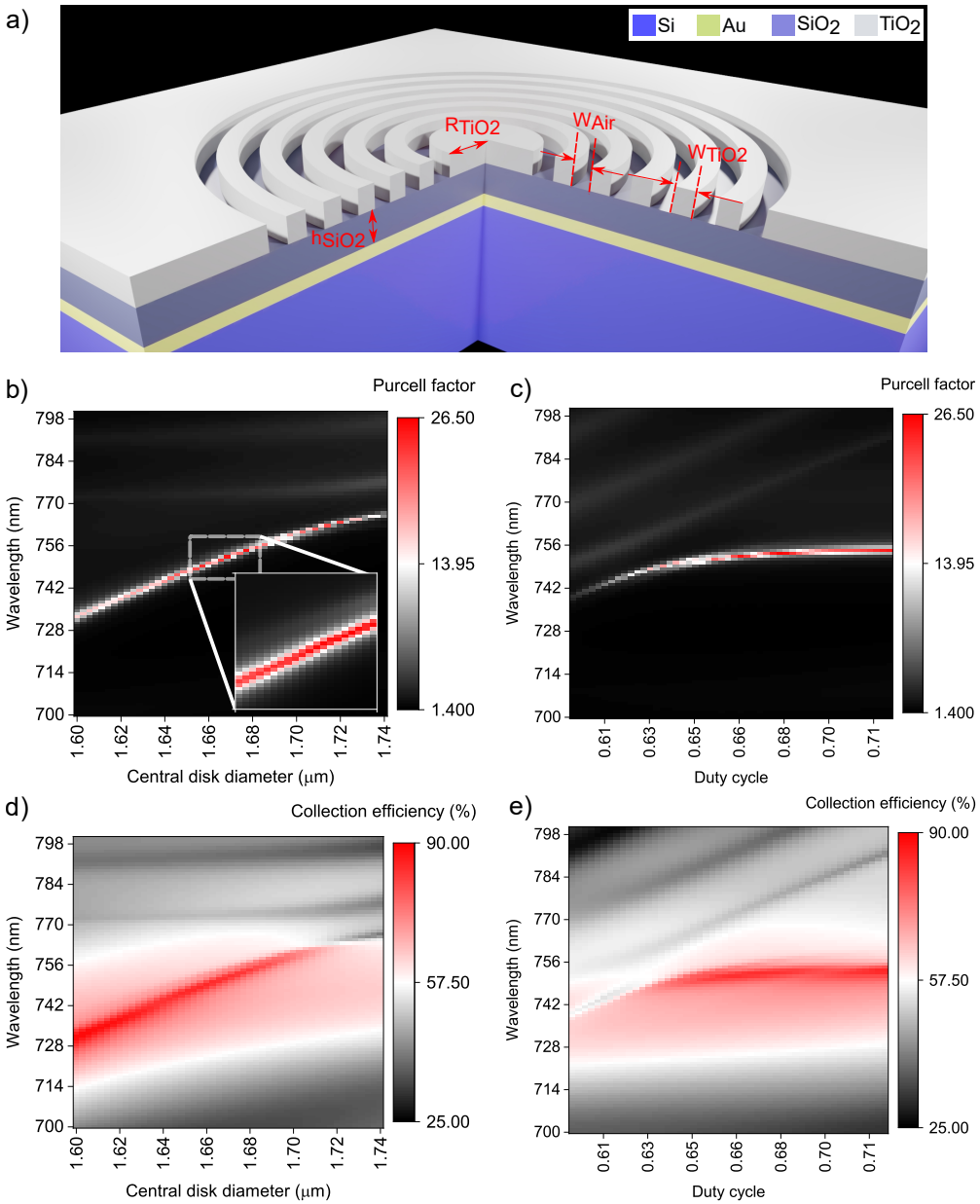

Figure 4.2: Bullseye structure design. (a) 3D representation of the structure. The structure consists of three layers of TiO_2, SiO_2 and gold on top of Si substrate. The width of the each ring and the gap between them are W_{TiO_2} and W_{Air}, respectively. The radius of the central disk is R_{TiO_2}. The emitter is placed 1 nm on top of the centre. The height of the TiO_2 and SiO_2 are h_{TiO_2} and h_{SiO_2}. (b,c) Purcell factor as a function of the central disk diameter (b) and the duty cycle (c), and wavelength. (d,e) Collection efficiency for NA= 0.68 as a function of the central disk diameter (d), and the duty cycle (e) and wavelength. The structure is designed for approximately 750 nm, and the value for central disk and duty cycle is calculated as 1.67 μm and 0.67, respectively. Number of rings in all above simulations is 10.

750 nm, and for this wavelength, the optimum R_{TiO_2} and duty cycle are calculated as 835 nm and 0.66, respectively. In all calculations, the objective lens NA is 0.68. According to Figure 4.2.b and Figure 4.2.c, the resonance wavelength can be tuned

by changing either the central disk or the duty cycle. Moreover, the resonance in the Purcell factor is narrower than in the collection efficiency; it means the Purcell factor is highly sensitive to the designed wavelength. This explanation highlights the importance of fabrication in these structures. This condition is less severe in the case of the collection efficiency (Figure 4.2.d and Figure 4.2.e) because of the gold mirror layer and its broadband reflection, as it is possible to have high collection efficiency for a broad range of wavelengths.

4.4 Dipole–cavity coupling condition

Now that the dimensions are calculated, I can explore the coupling relationship between the dipole emitter and the bullseye structure as the cavity. I will start with the formula presented in Chapter 3:

$$F = \frac{\tau_{free}}{\tau_{cavity}} = f(\Delta).(\frac{\overrightarrow{d}.\overrightarrow{\epsilon}}{|\overrightarrow{d}||\overrightarrow{\epsilon}|})^2.\frac{|\overrightarrow{\epsilon}(\overrightarrow{r})|^2}{|\overrightarrow{\epsilon}_{max}|^2}.F_P \tag{4.2}$$

As discussed earlier, F is considered as the full expression for the Purcell factor [134], and it is defined as the enhancement in the spontaneous emission rate due to the cavity compared to an identical infinite dielectric medium. In the following, each term in Equation (4.2) is discussed.

The first condition that needs to be matched is the wavelength of the resonance. The first term in Equation (4.2) represents this condition, and it is a function of the emitter–field spectral detuning (Δ). The dipole–cavity relation in terms of the wavelength is depicted in Figure 4.3.a. When the dipole and the cavity are wavelength–matched, the Purcell factor of 22.5 and the collection efficiency of 80 % can be achieved. According to the Figure 4.3.a, this structure can obtain high collection efficiency in a broader range of wavelengths (for CE $\geqslant$ 70 %, FWHM=4 $\pm$ 2.1 nm; for CE $\geqslant$ 60 %, FWHM= 25.4 $\pm$ 4.5 nm). The cavity and the dipole must be wavelength–matched to have a high Purcell factor. Only 1 % wavelength mismatch (FWHM=1.4 nm) can result in Purcell factor close to unity which means no enhancement in the radiative decay rate.

The second term in Equation (4.2) is to quantify how well different dipole polarisations work in the cavity. In Equation (4.2), $\overrightarrow{d}$ and $\overrightarrow{\epsilon}$ are the electric dipole moment of the emitter and the cavity mode electric field [48]. This structure is designed for in–plane dipole, $\theta = 90°$, in which θ is defined as the polar angle between the z–axis and the direction of the dipole. Collection efficiency and the Purcell factor are shown as blue and red in Figure 4.3.b. In this figure, two cases are studied; if the dipole is placed 1 nm above the TiO_2 layer (solid lines) and the case where

the dipole is in the centre ($z = 100\,\text{nm}$) of the TiO_2 disk (dashed lines). The dipole is in the centre of the central disk. According to the result, the higher the angle of θ, the better the value of the collection efficiency and the Purcell factor. As the cavity electric field is much more intense in the centre of the bullseye, it is expected to achieve a higher Purcell factor.

The last condition to study is the dipole displacement. According to the third term in Equation (4.2), the spatial detuning of the emitter with respect to the cavity can be explained by the ratio of the electric intensity of the emitter (ϵ) at the spatial position of r relative to the maximum of the electric field amplitude (ϵ_{max}). Figure 4.4.a and Figure 4.4.b show the collection efficiency and the Purcell factor as a function of the displacement in x and y directions, respectively. Based on Figure 4.4.b, the Purcell factor value can drop to almost half of the maximum value (at x=0) only by displacing the dipole 70 nm away from the centre. This result highlights the importance of positioning in the emitter–cavity systems. It should be noted that x and y displacement are not the same because the dipole is oriented only along the x axis.

The collection efficiency (red) and the relative Purcell factor (blue) are plotted as a function of the dipole displacement in the z–direction in Figure 4.4.c. In this figure, it is assumed that the dipole is positioned at x=y=0. Purcell factors are normalised to the Purcell factor at z= 201 nm to highlight the displacement effect better. As discussed earlier, the Purcell factor is maximum at the centre of the TiO_2 disk (z= 100 nm), and according to this plot, it is 50 % more enhanced than the value at z= 201 nm. Displacement in the z–direction severely affects the Purcell factor when the dipole is placed in the air rather than the case it is positioned in the dielectric. This is because the dielectric higher refractive index results in a confined

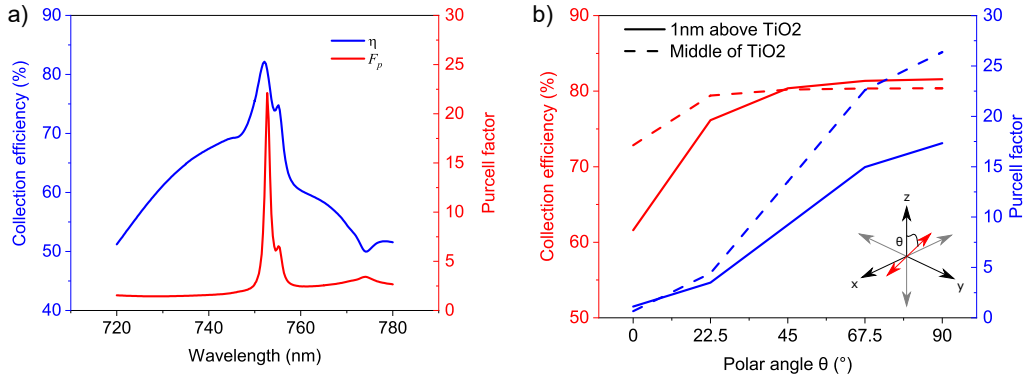

Figure 4.3: Dipole–cavity coupling condition. (a) Collection efficiency (left y–axis) and the Purcell factor (right y–axis) as a function of the wavelength. The system resonates at $\sim$ 752 nm. (b) Collection efficiency (left y–axis) and the Purcell factor (right y–axis) as a function of the polar angle of the dipole. 0° and 90° in axis represents out–of–plane and in–plane dipoles, respectively. Number of rings in both simulations is 10.

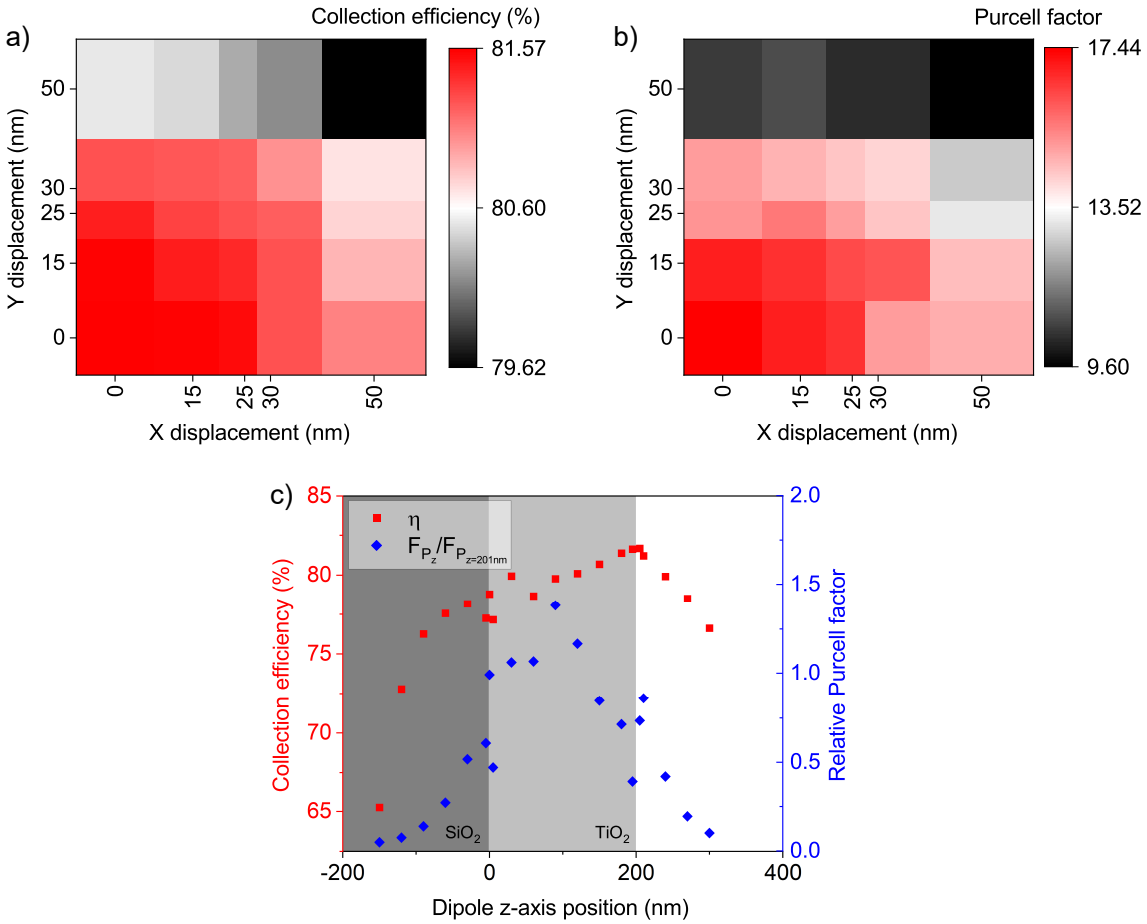

Figure 4.4: Dipole– displacement in cavity. (a) Collection efficiency as a function of the dipole displacement in x and y-direction. The system resonates at $\sim 752\,\text{nm}$. (b) Purcell factor as a function of the dipole displacement in x and y-direction. (c) Collection efficiency (left y–axis) and the relative Purcell factor (right y–axis) as a function of the dipole position in the z–axis (x=y=0). Collection efficiency has a fairly high value regardless of the position of the dipole. In contrast, the relative Purcell factor change dramatically in comparison to the case where the dipole is positioned in the middle of the TiO_2 layer.

electric field inside the disk.

When all conditions are achieved (ideal emitter–cavity coupling [135]), the maximum coupling between the emitter and the cavity can be expressed by the last term in equation (F_P). In my design, $F_P = 22.5$. This term is known as the ideal Purcell factor, and it defines as $F_P = 3Q(\lambda_{cav}/n)^3/4\pi^2 V_{eff}$, where Q and V_{eff} are the quality factor and the effective mode volume of the cavity, respectively. The quality factor is the cavity's FWHM relative to its resonance wavelength. In simulations, it can be derived by measuring the decay of the time–dependent electric field in the cavity. In this work, the quality factor is $1000 < Q < 2000$. From the quality factor perspective, photonic crystal structures offer much higher quality factors in the range of 10^6 - 10^8 [136, 137]. The mode volume is inversely proportional to the coupling strength between the emitter (dipole) and the cavity. The mode volume

can be obtained by integrating energy density over the cavity's volume and normalising it to its maximum value. In this work, I considered the mode volume defined as:

$$V = \frac{\int \epsilon E^2 dV}{max(\epsilon E^2)} \tag{4.3}$$

and according to my calculation, $V = 0.076\ \mu m^3$. From the mode volume perspective, plasmonic structures offer much lower mode volume in the range of 10^{-6} - 10^{-8} μm^3 [138].

4.5 Dipole–cavity coupling efficiency

To measure the efficiency of the coupling, few parameters can be defined. One important parameter is the effective enhancement factor [139] (or the brightness enhancement [125]) and it is defined as:

$$\langle EF \rangle_{eff} \propto \frac{\gamma_{exc}(\lambda_{exc})}{\gamma^0_{exc}(\lambda_{exc})} \times \frac{QE(\lambda_{em})}{QE^0(\lambda_{em})} \times \frac{\eta(\lambda_{em})}{\eta^0(\lambda_{em})} \tag{4.4}$$

where γ_{exc}, QE, and η are the excitation rate, quantum efficiency, and collection efficiency, respectively. Also, λ_{exc} and λ_{em} represent the excitation and emission wavelengths, respectively. In the above equation, the parameters with "0" in the superscript indicate the reference structure which is defined as the planar layer of TiO_2 on SiO_2/Au/Si substrate. The first term in that equation is the enhancement of the excitation at the resonance wavelength for the bullseye structure compared to the reference structure. Figure 4.5.a depicts this term in the above equation. The x–axis is the number of rings in the bullseye structure. The left (right) y–axis plotted in red (blue) illustrates the excitation enhancement for a dipole positioned in the centre of the disk (z= 201 nm on top of the disk). In this plot, two wavelengths of excitation are investigated; one for the 532 nm wavelength (known as off–resonance excitation) and the other for the 752.485 nm which is the resonance wavelength of the structure (resonance excitation). In both cases, by increasing the number of rings, higher excitation enhancement can be achieved; however, for the case, that dipole is placed 1 nm on top of the disk, resonance excitation enhances by a factor of 3.45 in comparison to off–resonance excitation. For the dipole placed in the disk's centre, this ratio is 15.87.

The second term in Equation (4.4) quantifies the ratio of the quantum efficiency (yield) enhancement at the wavelength of the emission. Quantum efficiency in the emitter–cavity system is defined as $QE = \gamma_{rad}/(\gamma_{rad} + \gamma_{nrad} + \gamma_{loss})$ in which γ_{rad}, γ_{nrad}, and γ_{loss} are radiative decay rate, non–radiative decay rate, and loss, respectively. In dielectric cavity systems, the loss is negligible. For emitters with a

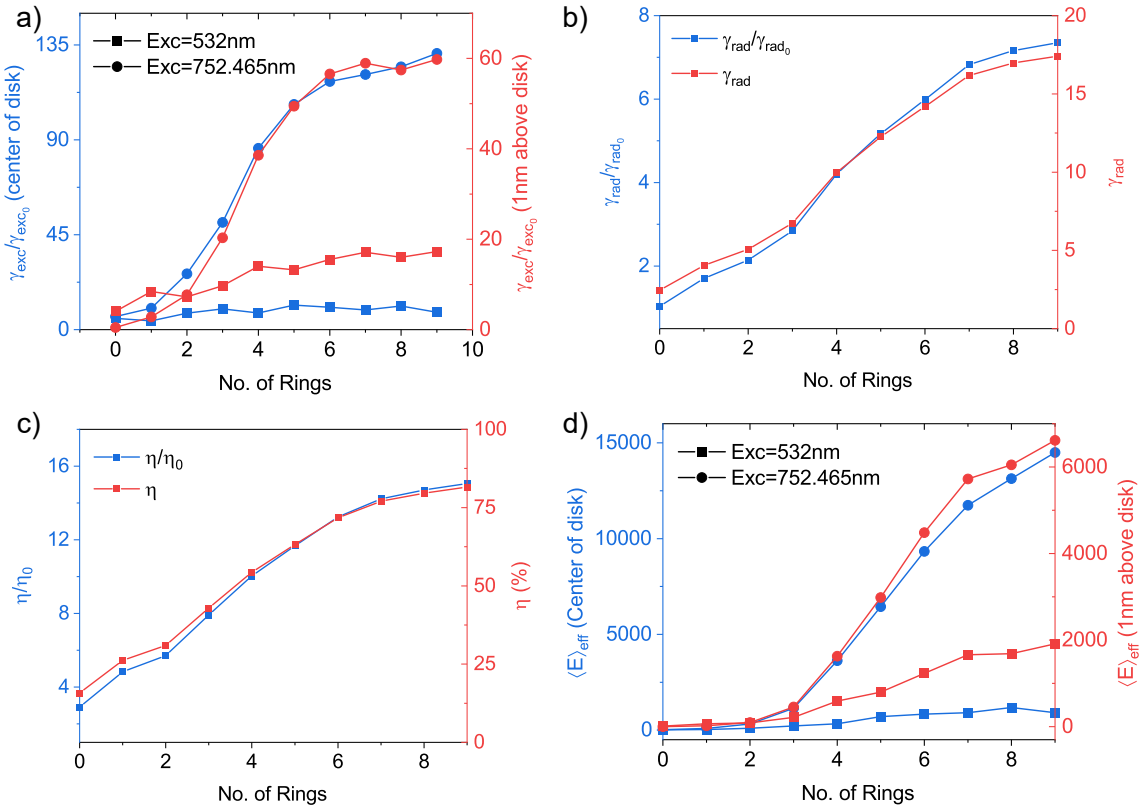

Figure 4.5: Dipole–cavity coupling efficiency. (a) Excitation enhancement rate for a dipole in the centre of the cavity (red) and a dipole 1 nm above the disk (blue) as a function of the number of rings. Square and diamond shapes illustrate off–resonance (532 nm) and on–resonance (752.5 nm) excitation, respectively. (b) The radiative decay rate enhancement (blue) and the radiative decay rate (red) as a function of the number of rings. (c) The collection efficiency enhancement (blue) and the collection efficiency (red) as a function of the number of rings. In all plots, it is clearly shown that the increasing number of rings can achieve better results. (d) Coupling efficiency for a dipole positioned at the centre of disk (blue) and a dipole positioned 1 nm above the disk (red).

poor intrinsic quantum yield like emitters in exfoliated 2D materials [140], I can assume that $\gamma_{nrad} \gg \gamma^0_{rad}, \gamma_{rad}$; therefore, the quantum efficiency is simplified to $QE/QE_0 = \gamma_{rad}/\gamma^0_{rad}$. This result is shown in Figure 4.5.b. The left (right) y–axis indicates relative decay rate enhancement (relative decay rate) in blue (red) as a function of the number of rings.

The final term in the effective enhancement factor (Equation (4.4)) is the relative collection efficiency. The collection efficiency (η) and the collection efficiency enhancement (η/η_0) are illustrated in right (red) and left (blue) axes in Figure 4.5.c, respectively.

It is obvious in all calculations that by increasing the number of rings, higher figures of merit can be achieved. The product of these terms results in the fluorescent count rate extracted from the emitter [141]. For on–resonant (off–resonant)

excitation, the effective enhancement factor is calculated approximately as 15000 (2000) for nine rings in the bullseye structure compared to the reference structure. It should be noted that the y–axes in Figure 4.5.d are unitless.

4.6 Characteristics evaluation

To evaluate bullseye characteristics designed in this work, its Purcell factor and collection efficiency are compared with the relevant works in different systems. This comparison is depicted in Table 4.1. An overview of the comparison is listed as follows:

- **Purcell factor**: Only two works have better F_P; in [132], the cavity is made of GaAs, with a refractive index of $n_{GaAs} = 3.4$. This is high compared to TiO_2, where I considered $n_{TiO_2} = 2.268$. This is possibly the main reason behind the higher value in their report. In [125], the author claimed that the structure is a hybrid design, but both antenna (bullseye) and resonator (nanocone at the centre of bullseye) are made from gold. In contrast, my work is based on only a dielectric cavity with a gold reflector.

- **Collection efficiency**: The difference between this work and other works is negligible (less than 5 %); the only work with a slightly better result is [132]. In line with what was suggested for the previous point, higher collection efficiency may result from a higher refractive index of grating, which results in diffracting light more efficiently.

As shown above, the Purcell factor and collection efficiency derived from this work

Table 4.1: Characteristics comparison between different bullseye works

Emitter	F_P	CE (%)	NA	n_{Cavity}[2,3] λ_{exc} (nm)		Ref.
NV (bulk)	1.2	82	1.42	2.41	650	[52]
NV (nanodiamond)	18	<80	0.9	1[4]	675	[119]
WSe_2	16	>45	0.9	2.02	750	[54]
InGaAs QD	56	>95	0.8	3.4	1340	[132]
AlGaAs QD	17	>90	0.65	3.4	780	[142]
InGaAs QD	18	>87	0.65	3.4	882	[120]
InGaAs QD	16	90	0.75	3.4	900	[143]
Colloidal QD	40	80	0.5	1[1]	650	[125]
InAs/InP QD	15	<90	0.65	3.4	1540	[130]
Multipurpose	22.5	>80	0.68	2.268	∼750	This work

[1] $n_{grating} = 0.14$, $\kappa_{grating} = 3.4$ [2] For QDs, values derived from [131, 144]
[3] $n_{Cavity} = n_{Grating}$ [4] $n_{grating} = 2.23$

are higher than in most published works. If I only consider dielectric cavities operating in the visible wavelength, this design outperforms other published results.

The quantum efficiency of the quantum dot is nearly one and remains intact when coupled to the bullseye cavity structure, whereas the quantum efficiency of single–photon centres in 2D materials is often low. While the nonradiative decay term of total decay remains unchanged in the presence of cavity structure, the radiative decay term alters due to the modification of the local density of states. Consequently, the quantum efficiency of single–photon centres in 2D material can be improved thanks to the Purcell factor of the cavity structure [34]. The strength of this improvement is related to the spatial distribution of the cavity mode. For emitters located at the surface of cavity geometry, the TE_2 slab mode waveguide provides a longer evanescent tail which results in higher intensity above the slab [58].

4.7 Increasing collection efficiency in direct coupling

For quantum light sources with fast radiative decay rates, collection efficiency becomes a crucial parameter compared to the Purcell factor. For this reason, emission from fibre–coupled is efficient and beneficial. To investigate this, I considered a commercially available single–mode fibre, 630HP (Thorlabs), with a core radius of 1750 nm and refractive indices of 1.46 ($=n_{core}$) and 1.45 ($=n_{cladding}$) for core and cladding, respectively. All simulations were carried out in the air (same as in previous sections). In addition, I assumed the distance between the fibre and the cavity is fixed to 2 µm.

The apodization[1] technique is employed on the grating to increase collection efficiency further. Apodization is essential in designing other photonic structures that involve periodic geometries, such as grating couplers and distributed Bragg reflectors. Apodization helps to redirect more light in specific directions. In the case of Bragg grating structures, like Bullseye in this work, changing the periodicity of reflective components results in altering the mirror strength of each element (rings), and higher collection can be achieved. There are different methods to apodize a periodic structure; in this work, I optimise grating geometry ring by ring to achieve higher collection efficiency. Figure 4.6.a depicts collection efficiency as a function of ring period and duty cycle for the first ring (k=1); disk dimensions remained unchanged in all simulations for apodization. In this figure, three areas are highlighted with circles; the yellow circle shows the collection efficiency of $\sim 2.2\,\%$ for

[1] chirp, taper

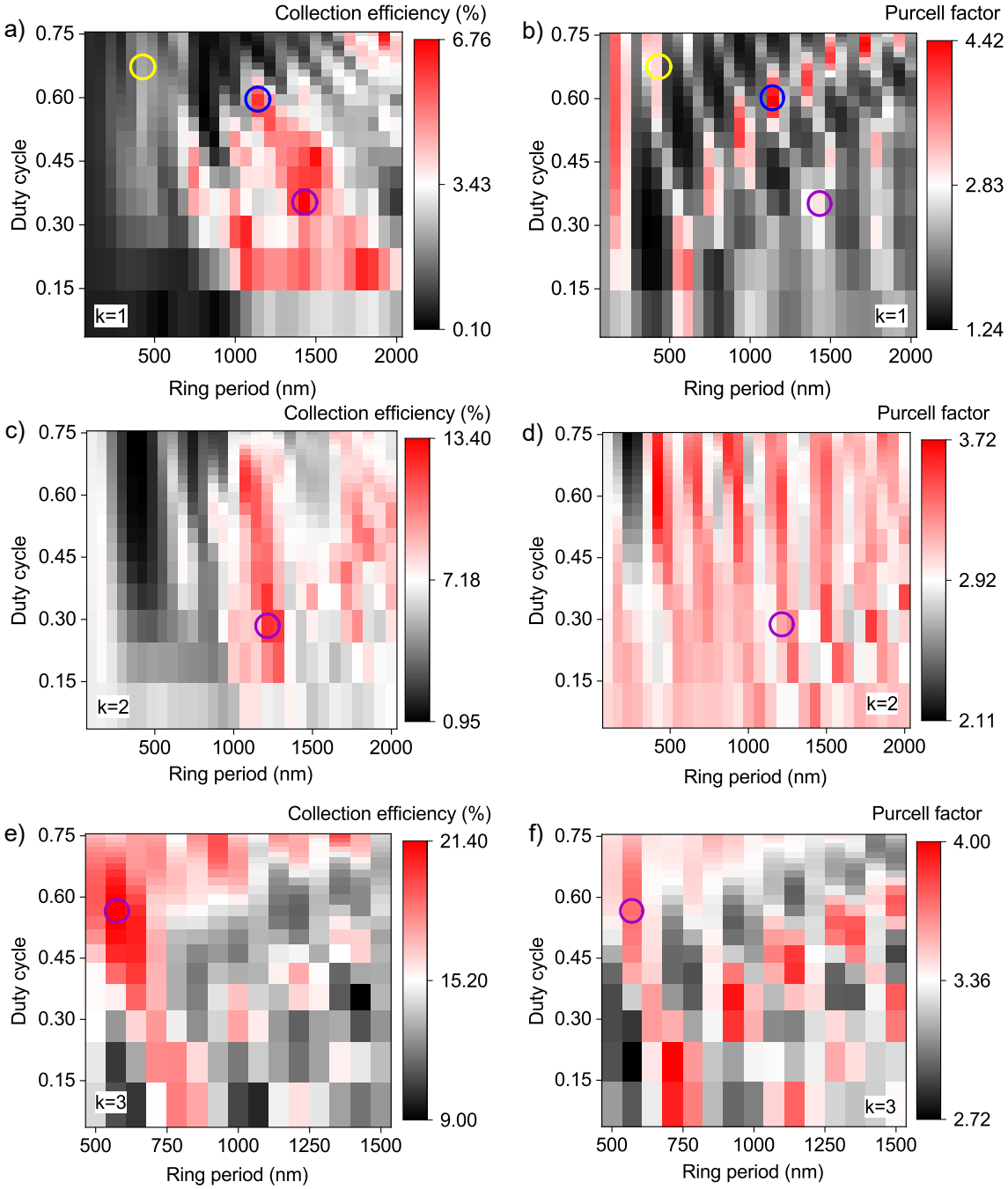

Figure 4.6: Results of apodization steps for the bullseye structure. (a,c,e) Collection efficiency and (b,d,f) Purcell factor as a function of ring period and duty cycle for the first ring (k=1), the second ring (k=2), and the third first ring (k=3), respectively.

a non–apodized ring (ring period = 420 nm, duty cycle ∼ 0.67). The pink circle shows the collection efficiency of 6.74 %, which is the highest value in the sweep (ring period ∼ 1428 nm, duty cycle ∼ 0.36). Finally, the blue circle indicates the highest achieved Purcell factor (4.41, see Figure 4.6.b). The collection efficiency for the blue circle is ∼ 6.0 %, and the Purcell factor for the pink circle is 3. Because I aim to achieve higher collection efficiency, I selected ring period ∼ 1428 nm and

duty cycle ~ 0.36.

Next, the ring period and the duty cycle of the second ring were swept to obtain higher collection efficiency. Results of the sweeping ring period and duty cycle for the collection efficiency and the Purcell factor are shown in Figure 4.6.c and Figure 4.6.d, respectively. In these figures, the pink circle indicates the highest collection efficiency of 13.38 % for the ring period and duty cycle of ~ 1214 nm and ~ 0.28, respectively. Figure 4.6.e and Figure 4.6.f illustrate the apodization results for the collection efficiency and the Purcell factor for the third ring, respectively. The derived optimised values for the ring period and the duty cycle are ~ 571 nm and ~ 0.57, respectively.

The result of apodization is shown in Figure 4.7.a for the collection efficiency. The blue and red lines indicate the collection efficiency of the bullseye structure without and with apodization, respectively. Due to extremely high simulation time, I limited the optimisation to only five rings (k=5). It is clear that by applying apodization, it is possible to achieve higher collection efficiency; however, the collection efficiency's increasing trend as a function of the number of rings starts to saturate at higher rings (k$\geqslant$5). This behaviour possibly can be influenced by three parameters:

- **Numerical aperture**: The fibre simulated in this work has a NA=0.13. Higher NA results in higher collection efficiency.
- **Fibre core diameter**: Core diameter affects the acceptance angle of light and allows the higher photon to be collected by fibre.
- **Distance between fibre and the cavity**: This parameter also can affect the acceptance angle of light.

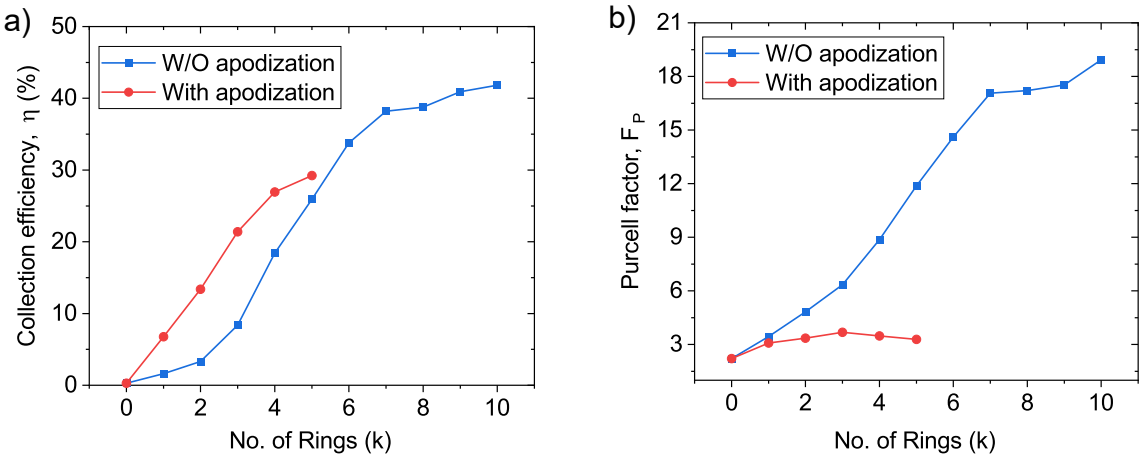

Figure 4.7: Apodization results for the bullseye structure. (a) Collection efficiency and (b) Purcell factor as a function of the number of rings (k). In all simulations, the distance between the fibre and the bullseye structure was constant (2 µm).

Figure 4.7.b shows the Purcell factor for apodized and non–apodized structures. Because I apply apodization to achieve higher collection efficiency, observing no increment in the Purcell factor is reasonable. Collection efficiency can be improved further by replacing air with a medium with a higher refractive index. Practical designs include adhesives between fibre and the photonic structure to improve fibre alignment and stability[132]. In addition, by introducing non–uniform etch between rings, higher collection efficiency (and Purcell factor) can be achieved [131].

4.8 Discussion

In this study, I have shown the different steps to designing a photonic bullseye structure to enhance the emission of a point light source. The key parameters to design a structure to obtain high collection efficiency and the Purcell factor were investigated. After this step, the coupling condition between the dipole and the cavity is studied. The dipole and the cavity must match spatially, spectrally and angularly. A slight variation in each of these conditions will result in a dramatic reduction in the Purcell enhancement. In the next step, the efficiency of the coupling is discussed. Higher efficiency can be obtained by including rings in the structure. Also, it is worth noting that a higher NA objective lens will give a better result. Finally, achieving higher collection efficiency into fibre was studied for non–apodized and apodized geometries. To fix the fibre on the sample, one can use glue. In the simulation, we assumed that the refractive index between the fibre and the structure is 1; however, if the refractive index of the glue is chosen to match the refractive index of the fibre's core, higher collection efficiency can be achieved.

CHAPTER 5

Generating emitters in hBN

5.1 Introduction

In the previous chapter, I presented an approach to design a bullseye cavity for surface–mounted emitters. Although the cavity resonant frequency was 750 nm, the cavity can be designed for another wavelength with the same approach. In the next step, I need to address single photon sources. To achieve that, I discuss different approaches to generating defect centres in hBN in this chapter. These studies aim to create colour centres in a controllable and deterministic manner. First, I present an example of colour centres in hBN. Next, I exploit different cleanroom techniques such as plasma ash, annealing, and strain induced by nanostubs. Finally, I investigate the ion irradiation technique.

5.2 Overview of Defects in hBN

Before proceeding in this chapter, it is essential to understand different emitters in hBN better. Figure 5.1 aims to address this purpose. Since the discovery of quantum emitters in hBN, several theoretical papers have studied different combinations of defects in the hBN crystal lattice [145, 146]. Depending on different calculations, different transition frequencies have been reported for some defects. It is worth mentioning that other conditions like strains can shift the transition frequencies reported in Figure 5.1. Exfoliation is one of the first steps to applying non–uniform strain to the crystal. This initial strain might play a role in following up on other approaches (for example, annealing). Discussing all these defects is not the scope of this research; however, in the following sections, I show that different approaches can create various forms of colour centres in hBN; therefore, I use Figure 5.1 to predict the origin of these defects.

5.3 Unprocessed hBN

Before I studied different techniques to generate defect centres, I explored defect centres on unprocessed hBN. I used the method described in subsection Section 3.4.1 to exfoliate a thin layer from the hBN crystal. For this experiment, I used HQ Graphene crystal. Figure 5.2.a indicates the PL spectrum of the only defect on

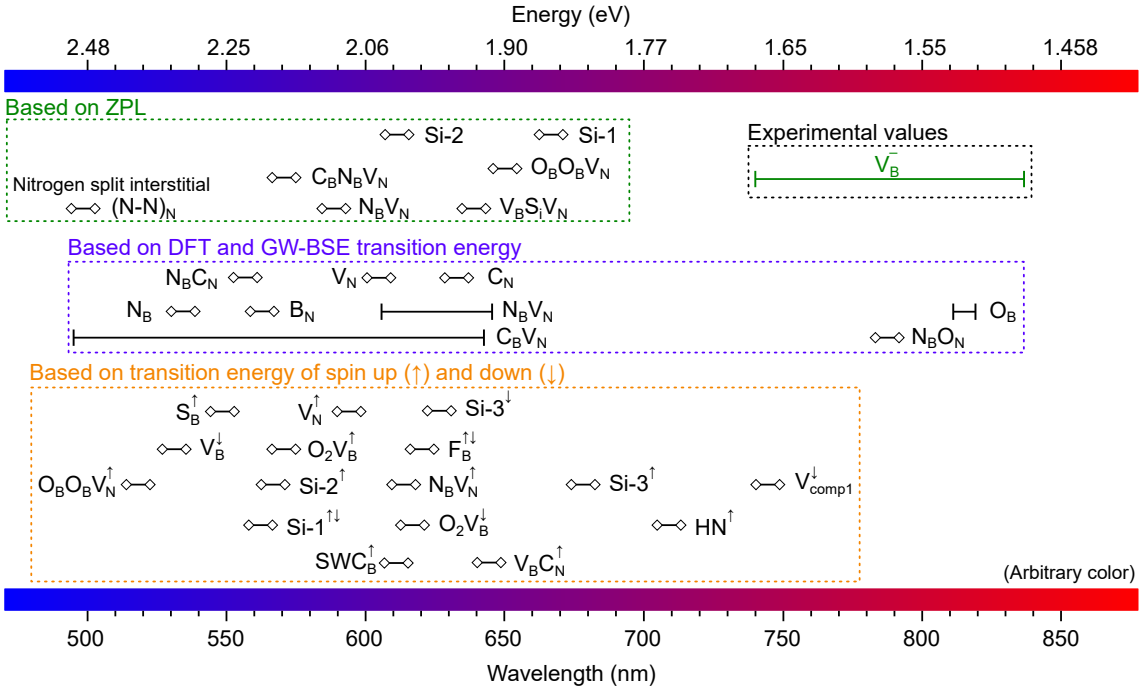

Figure 5.1: Theoretical and experimental defects in hBN. Green, purple and orange dashed boxes show the theoretical defect in hBN, whereas the black dashed box indicates the experimental defect in hBN. The up and down arrows in the orange box specify the spin up and down, respectively. All data is derived from [145–147]

the exfoliated flake on the SiO_2/Si sample. Peaks at 594 nm (2.08 eV), 643 nm (1.92 eV), and 701 nm (1.76 eV) are separated by 160 meV, and peaks at 656 nm (1.89 eV) and 715 nm (1.73 eV) are separated by 160 meV. This value is very close to the experimentally and theoretically reported value of the phonon energy in hBN (165 ± 10 meV) [90, 148]. The single photon emissions from the defect at 593 nm may relax via a phonon–assisted transition with the one (643 nm) and two (701 nm) optical phonon sidebands [149]. The theoretical calculation by Tran et al. suggests that these peaks originally come from point defects caused by boron and nitrogen vacancies as well as anti–site nitrogen vacancies [89]. A second–order correlation experiment was carried out to check single–photon characteristics at this centre. For this purpose, I exploit the HBT setup described in subsection 3.2.2. I used optical filter (tilted 650 nm short–pass) to block other emissions. The result of this experiment is shown in Figure 5.2.b. The following fitting formula was used to fit the data:

$$1 - (1 + g^{(2)}(0))e^{-\frac{t}{\tau}} \tag{5.1}$$

Based on the result, $g^{(2)}(0)$ is calculated as 0.56 with a lifetime of 4.9 ns. This result suggests that the peak at 593 nm can be a single colour centre with antibunched emission with a two–level system.

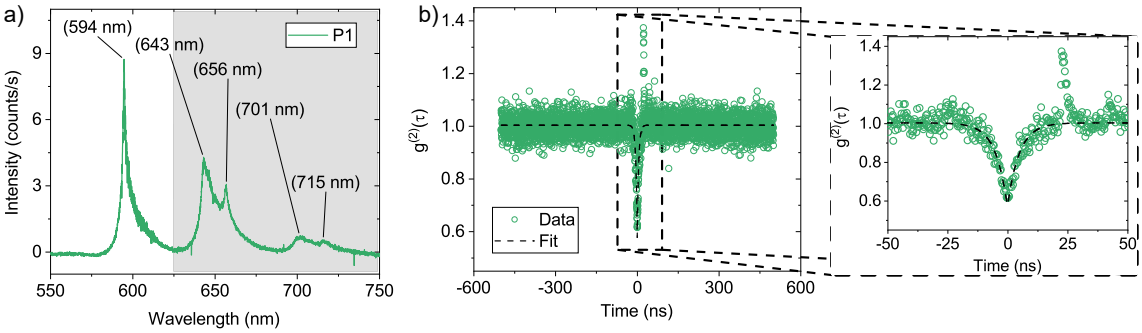

Figure 5.2: Single defect centre in unprocessed hBN. a) PL spectra of multiple defect centres in unprocessed hBN. b) second–order correlation function of the defect around 594 nm. The grey area in (a) shows the range of the PL spectrum that has been filtered. The black line represents the fitting model. Based on the fitting curve, $g^{(2)}(0)$ is 0.56.

5.4 Plasma-annealing treatment approach

The first approach I investigated was the Plasma–annealing treatment whose recipe is discussed in subsection 3.4.2. As discussed in subsection 2.5.3, plasma and annealing can create stabilised optically active defect centres in hBN. The plasma etching step damages the crystal of hBN and creates unstable defect centres. Subsequent annealing helps to (partially) heal the crystal lattice. After this step, the remaining defect centres show more stable optical emissions. Figure 5.3 shows the results of this study where spectra taken from the same flake. First, I characterised the flake before treatment. I could only find one spot with a bright PL spectrum which is shown in Figure 5.3.a. Next, I treated the sample, which consisted of one step of etching at 225 mTorr for 1 min under 100 W plasma power with 100 sccm oxygen (Figure 5.3.b) and one step of annealing and plasma ashing (Figure 5.3.c). The "1st treatment" in Figure 5.3 stands for the "Etch-Anneal-Ash" steps. After each step, I characterised the same flake to check the impact of treatment on the flake. Because the origin of generated defects is unclear to me and to facilitate comparison, I categorised spectra into four groups in which I only considered similarity in the spectrum as the main criteria for group spectra. In what follows, I elaborate on these groups:

- **Group I**: illustrates a group of emitters with a peak of around 600 nm. Some emitters do not have a sharp peak, but their spectra are similar to those with a sharp peak. According to Figure 5.1, N_BV_N, V_N, $C_BN_BV_N$, and O_2V_B are among the few candidates with transition energies around 600 nm.

- **Group II**: depicts an ensemble of emitters whose PL shows a broad spectrum from 600 nm to 800 nm. These broad spectra might have sharp peaks. As these

groups are ensembles of emitters, predicting their origins is difficult; According to Figure 5.1, there are many defects within that range.

- **Group III**: shows a group of emitters with an emission wavelength at 700 nm. Defects like $O_BO_BV_N$, V_BC_N, and HN can be some of the candidates for this group of emitters.

- **Group IV**: represents PL emissions around 800 nm. V_B^- is the most studied defect in this group, exhibiting a broad spectrum around 800 nm. N_BO_N and O_B are other candidates whose transition energies are around this wavelength.

According to Figure 5.3.b, etch step successfully generated defect centres by mainly damaging the crystal lattice; however, I observed that majority of these centres are unstable, and more prolonged exposure makes them less bright or, in some cases, they disappear in few seconds. This condition is defined as bleaching. Instead, there were some bright spots on the edge of flakes which showed higher stability in time (more than 1 min). Moreover, the fluorescence intensity of the entire flake increased after this step (check Figure 5.6.b).

In the next step, I annealed and then performed gentle O_2 plasma ash (100 W, 1 min, 30 sccm). The results of this step are shown in Figure 5.3.c. It is clear that after this step, narrow linewidth emitters appeared in the flake (group I and III); the FWHMs for emitters in group I and group III are 12–16 and 25 nm, respectively. In addition, I observed multiple peaked spectra (group II) as well as defects with broad spectra (group IV) around 700–800 nm. I also observed that fluorescence stability increased significantly after this step. As the treatment approach (etch–anneal–ash) was successful in generating narrow linewidth emitters, I was interested in examining the 2nd treatment effects on the same flake. Figure 5.4.a illustrates the results. I found all spectra featured broad and intense fluorescence. That suggests 2nd treatment (another etch–anneal–ash step) resulted in further crystal damage. Finally, I performed a long (1 h) plasma ash step on the same flake which is illustrated in Figure 5.4.b. Similar to the 2nd treatment, prolonged ash step can also damage the crystal lattice. Interestingly, the spectra in this step are more identical to each other than in the previous step.

To check the possibility of creating a single defect centre, I measured power saturation and second–order correlation. The selected defect centre in group III is shown in Figure 5.3.c. This defect is shown again in Figure 5.5.a. There are two prominent peaks in P70's spectrum; I suspect that the 669 nm is the central peak, and the 733 nm can be its PSB as it appeared around 162 meV (or $\sim 1305\,\mathrm{cm}^{-1}$). The power saturation experiment is depicted in Figure 5.5.b; although I were limited by maximum laser power at the time of the experiment, I could fit background corrected data. According to the fitting result, the saturation intensity and power are

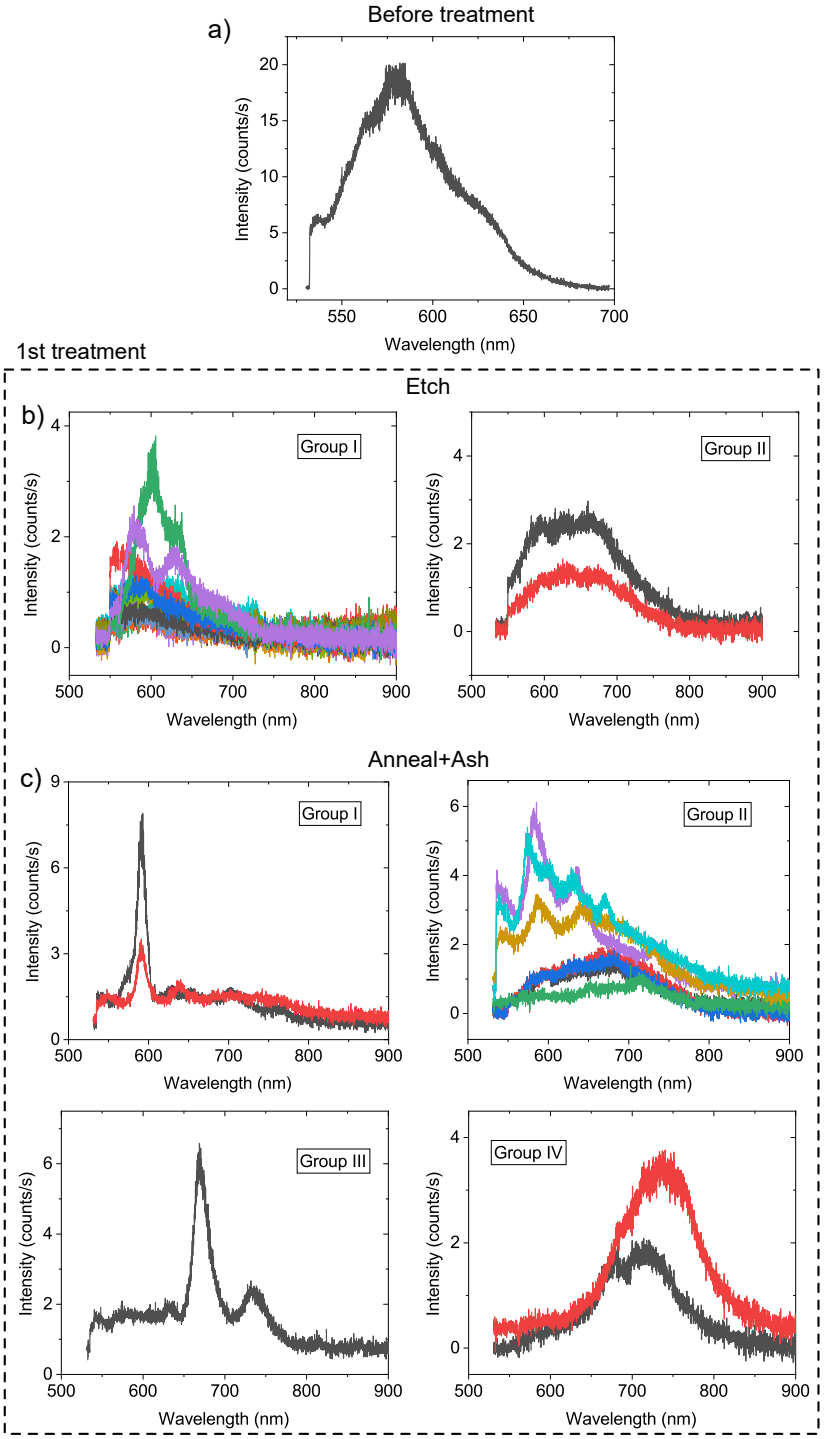

Figure 5.3: Treatment study on an exfoliated hBN flake. a) PL spectra before treatment from the only found defect. b,c) The PL spectra after the "etching" and "annealing and plasma ashing" steps, respectively. These two steps consider the 1st treatment. All spectra were taken from the same flake. A tilted long–pass filter at 550 nm was used to acquire these data.

268 ± 57 kHz and 9.56 ± 2.6 mW, respectively. In Figure 5.5.b, BGhBN represents the background date taken from the hBN flake. Finally, the second–order correlation result is shown in Figure 5.5.c, in which the black–dashed line indicates the fitting

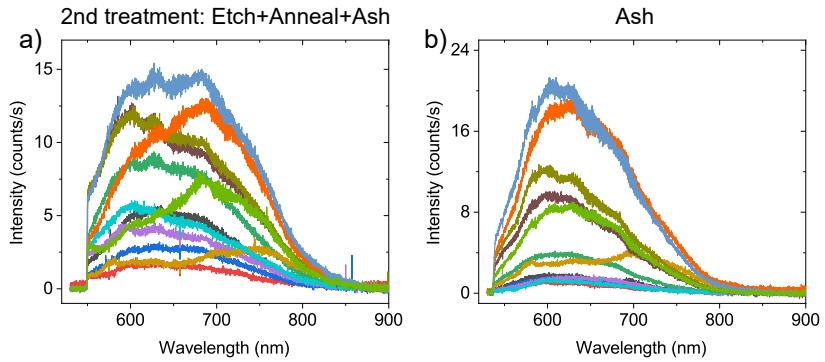

Figure 5.4: Second treatments on an exfoliated hBN flake. a) The PL spectra after 2nd treatment. b) The PL spectra after a single plasma ashing step. All spectra were taken from the same flake. A tilted long–pass filter at 550 nm was used to acquire these data.

function. A zoom–in view of the result is shown in this figure. According to this result, I can see both bunching and antibunching behaviours which suggest this defect centre can be a three–level system.

Optical microscopy images and PL raster scans of the studied flake in Figure 5.5 are shown in the top and bottom rows of Figure 5.6, respectively. Figure 5.6.a

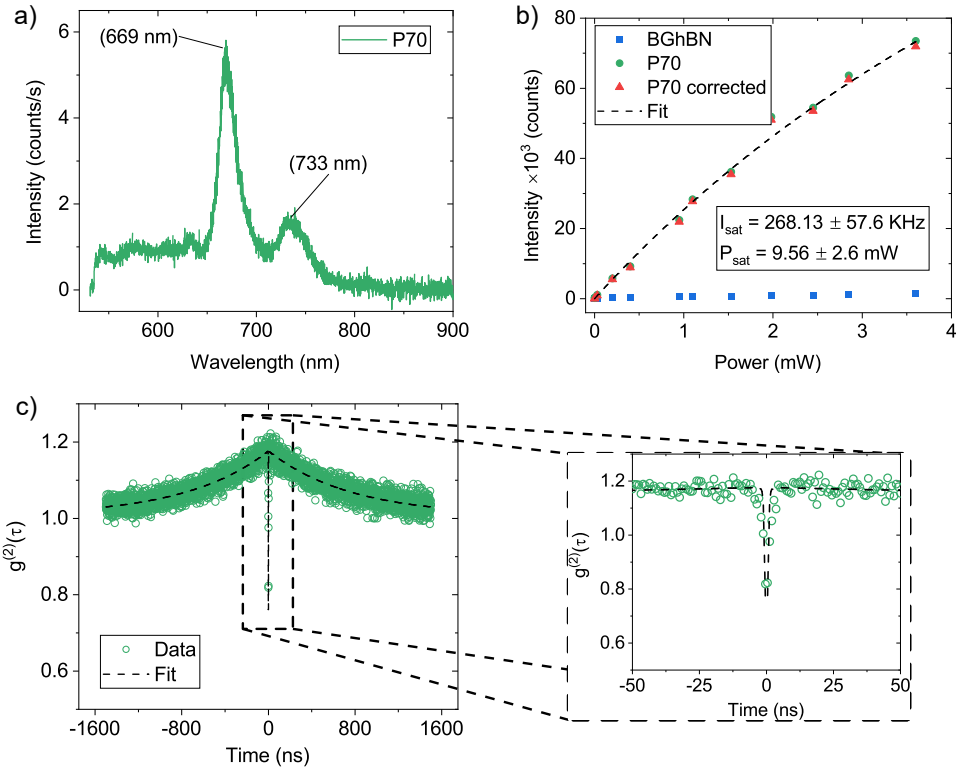

Figure 5.5: The power saturation measurement of an emitter was found after the first treatment study. a) PL spectrum of a point defect around 669 nm. b) Power saturation measurement from the defect centre showed in (a). The fitted values for the saturation intensity and power are 268 ± 57 kHz and 9.56 ± 2.6 mW, respectively.

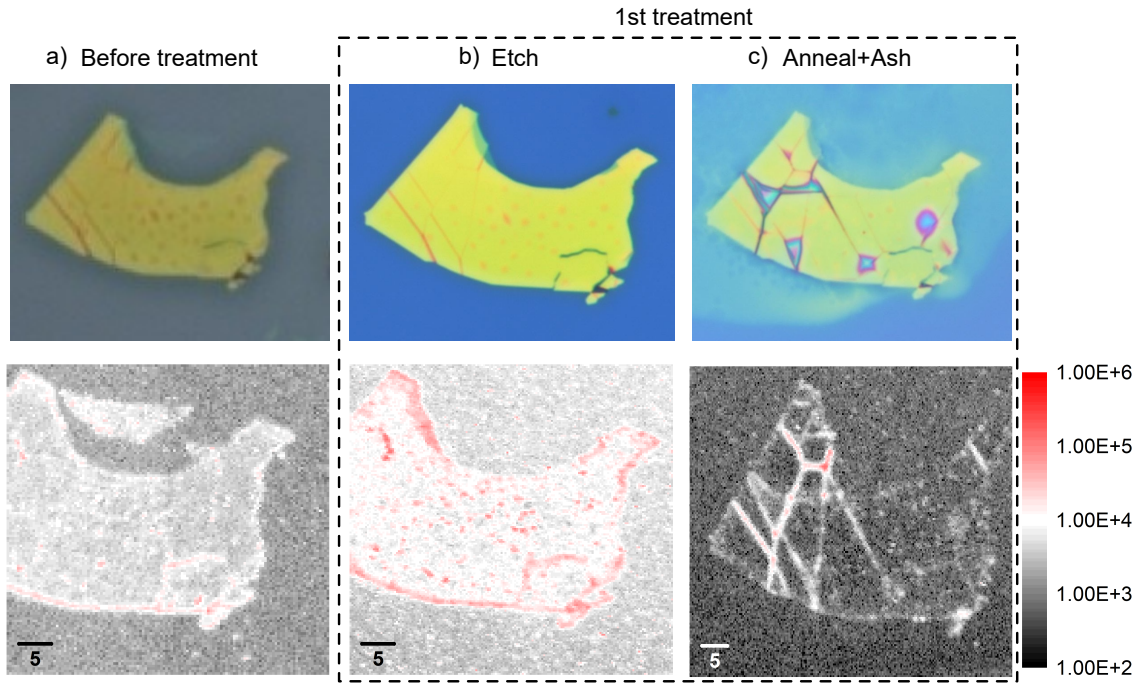

Figure 5.6: Evolution of 1st treatments on hBN flake. Optical microscopy images (top row) and PL raster scans (bottom row) for a) before treatment, b) after plasma etch, and c) after annealing and plasma ash.

and Figure 5.6.b show the condition before treatment and after plasma etch. As discussed, plasma etching increases the flake's and substrate's overall fluorescence intensity (around two or three times). Also, the appearance of point–like spots is clear after the plasma etch. The result after the annealing and plasma ash step is illustrated in Figure 5.6.c. It is evident that the overall fluorescence intensity of both flake and substrate decreased (around ten times). It is expected that annealing damages the flake's crystal structure. During these measurements, the excitation laser power was kept constant at around 195 µW at the back of the objective lens. This study shows that 1st treatment can create narrow linewidth emitters with antibunching characteristics.

5.5 Strain and treatment approach

Earlier works on WSe_2 showed that a localised strain gradient induced by the nanopillars might be playing an active role in producing single photon emitters [150, 151]. Therefore, I explored the possibility of generating emitters in hBN by applying local strain in this study. To achieve this, I investigated thin layers of CVD–grown hBN on Si and SiO_2. The samples were prepared by the Hoffman group at Cambridge University; as discussed in [75], hBN is grown on a platinum catalyst at high temperature, then transferred onto the substrate and finally peeled off the catalyst due to the weak interaction between the two. As shown in the pre-

vious section, the treatment helped me to create defect centres in hBN; therefore, I treated samples in the next step with the recipe mentioned earlier. In what follows, I elaborate on these studies.

5.5.1 CVD hBN on Si nanostubs

One of the samples I studied was a thin layer of CVD grown hBN transferred on Si nanostubs. Silicon nanostubs sample consists of 10 × 10 arrays of top–down etched silicon formed in nanostubs fabricated at UCLA. The height of the nanostubs was 100 nm, the pitch size was 2.8 µm, and the width of each nanostub was 150 nm. Figure 5.7.a indicates the tilted viewing angle scanning electron microscope (SEM) image of one of the regions, including thin layers of hBN on Si nanostubs. Figure 5.7.b is the 2D atomic force microscope (AFM) result taken from the same area shown in Figure 5.7.a. The contrast between the two regions in the AFM result belongs to different thicknesses of hBN. It should be noted that nanostubs pierce hBN flakes.

PL raster scan of Si nanostubs covered by hBN before the treatment is shown in Figure 5.8.a. The scale bar shows 2 µm in all figures. There is no sign of PL enhancement in this area. The two bright spots in Figure 5.8.a are contamination. Next, the sample was treated; the recipe used in this work is explained in subsection 3.4.2. I observed enhancement of PL emission from hBN on and off the nanostubs and on the edge of the square shown in Figure 5.7.a. Next, I treated the sample for the second time with the same recipe. Figure 5.8.c shows the result of this step. I observed that the number of bright spots on and off the nanostubs and on the edge of the square increased compared to the previous step. Yellow and green dashed

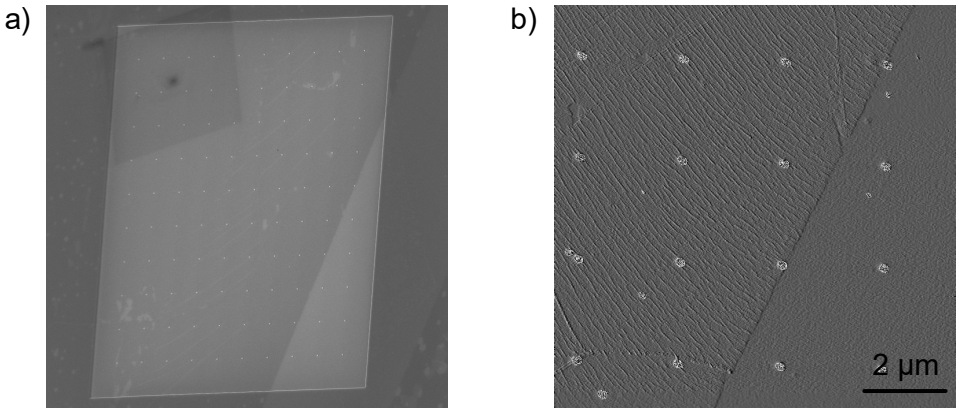

Figure 5.7: SEM and AFM of hBN on Si nanostubs. a) Stage–tilted SEM image of Si nanostubs. All the region is covered by hBN. The contrast between two areas is related to the difference in their thickness. b) AFM result of the same area shown in (a). According to the AFM result, the nanostubs pierce the hBN flakes. The scale bar shows 2 µm.

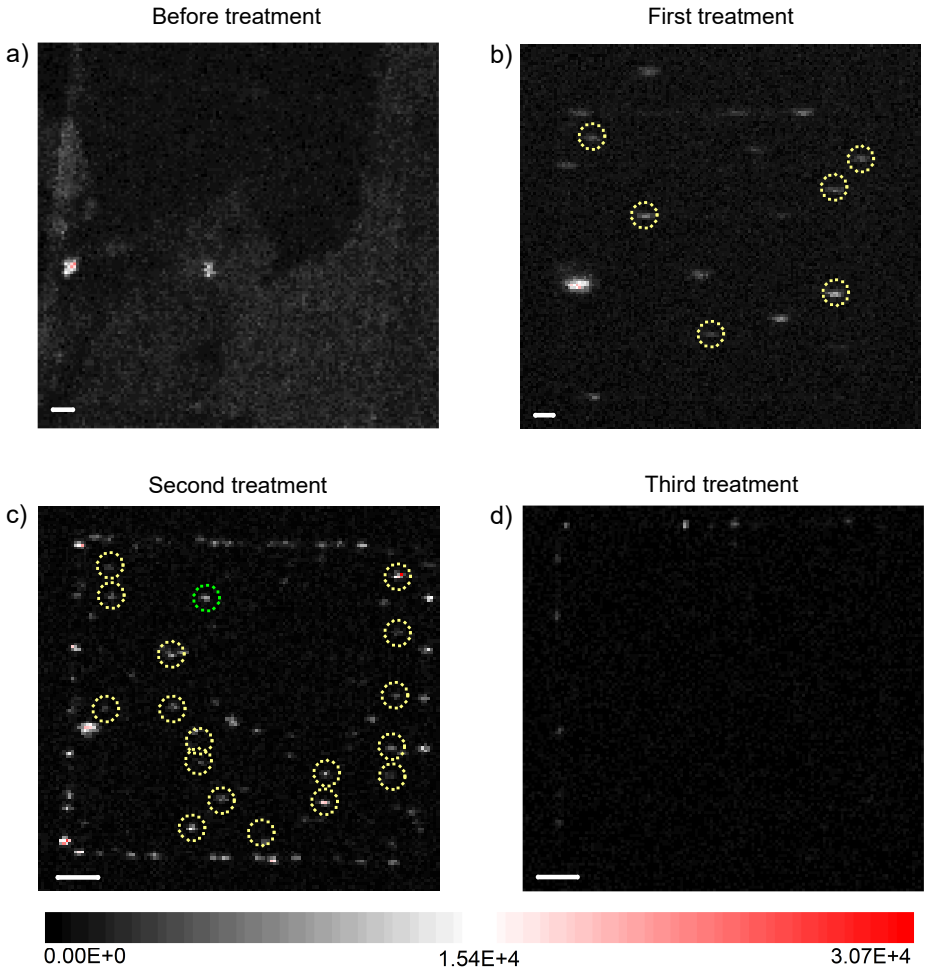

Figure 5.8: The PL raster scans of Si nanostubs covered by hBN. a) before, and after b) first, c) second, d) and third treatments. Yellow and green dashed circles indicate the bright spots appeared on the nanostubs. The scale bar shows 2 µm.

circles indicate the bright spots on the nanostubs in the first and second treatments. Finally, I treated the same area for the third time. Unlike the last two treatments, I only found bright spots on the square's edge. It should be noted that the area shown in Figure 5.8 is different from the one shown in Figure 5.7.

Figure 5.9 depicts the result after the same area's 1^{st}, 2^{nd}, and 3^{rd} treatments. We performed etch–anneal–ash in each treatment step on the sample without changing the recipe. Because of the background emission from the silicon substrate, I corrected all PL results with the background signal. As also discussed earlier, there was no sign of PL enhancement in the area of nanostubs before the treatment. After the 1^{st} treatment, there was no evidence of the deterministic generation of defect centres on silicon nanostubs; however, I observed the deterministic generation of defect centres on nanostubs after the 2^{nd}. group I in Figure 5.9.b and Figure 5.9.d illustrates a group of defect centres which have PL peaks around 600 nm, whereas group II in Figure 5.9.c and Figure 5.9.e identifies a group of defect centres which

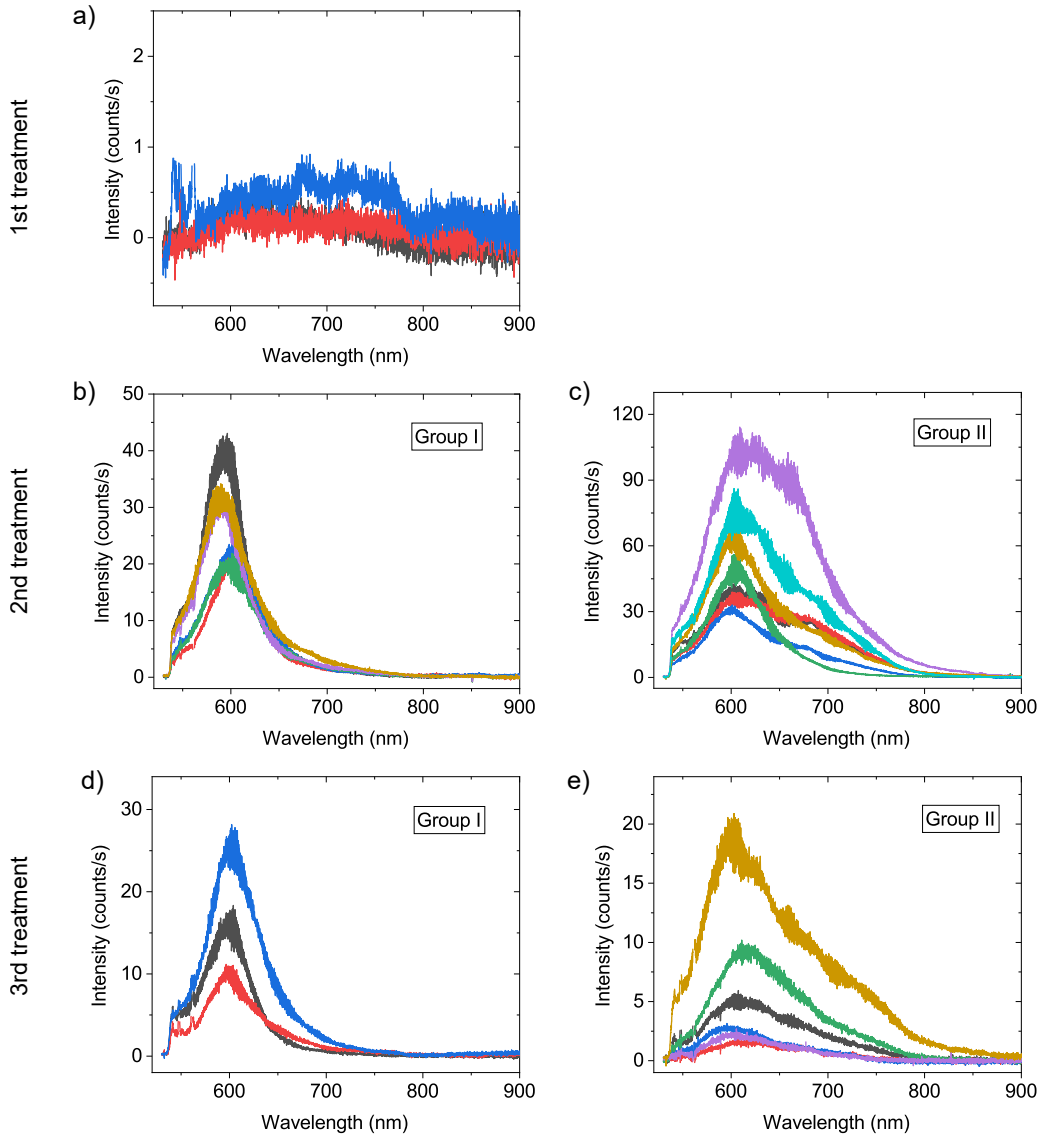

Figure 5.9: PL spectra of Si nanostubs covered by hBN. PL spectra after a) the 1st, b) the 2nd, and c) the 3rd treatments from the same area. Before treatment, there was no sign of PL enhancement in this area. Two bright spots in (a) are contamination.

have PL peaks around 600 nm but also feature a broad spectrum from 600 nm to 800 nm.

I studied power saturation measurement from one of the defect sites shown in Figure 5.10.a generated after the 2nd treatment (check the green dashed circle in Figure 5.8.c). According to the result depicted in Figure 5.10.b, the hBN background corrected signal from this defect centre shows a saturation behaviour at 3.3 mW. The saturation intensity derived from the fitting formula is 274 ± 20 kHz. In this figure, BGhBN represents the background date taken from the hBN flake. I performed a second–order correlation experiment on this particular defect centre, but I did not observe any anti–bunching, which suggests this defect centre is an ensemble of

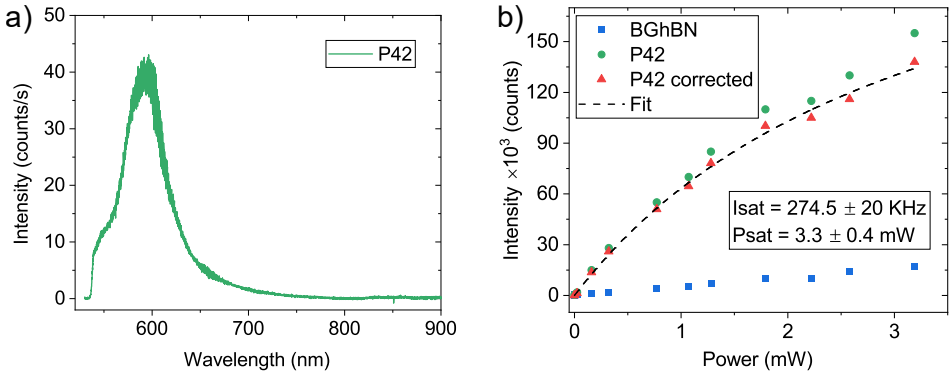

Figure 5.10: The power saturation measurement of an emitter found on Si nanostubs after the second treatment. a) PL spectrum of a point defect around 600 nm. b) Power saturation measurement from the defect centre showed in (a). The fitted values for the saturation intensity and power are 274 ± 20 kHz and 3.3 ± 0.4 mW, respectively.

defects.

5.5.2 CVD hBN on SiO_2 nanostubs

In addition to Si nanostubs, I studied SiO_2 nanostubs. Despite achieving better optical contrast between hBN layers and the underlying layer, this study aims to apply different strains to the hBN. This sample consists of arrays of circular and rectangular SiO_2 nanostubs with different widths from 80 nm to 320 nm fabricated on Si substrate. The height of nanostubs is 150 nm. The hBN in this sample was fabricated, as discussed earlier in subsection 5.5.1. Figure 5.11 shows a SEM image of the rectangular SiO_2 nanostubs.

After characterisation, there was no sign of PL enhancement. Next, this sample was treated the sample with the condition described in Section 3.4.2. Figure 5.12.a and Figure 5.12.b indicate PL spectra. From Figure 5.12.a, I can distinguish a peak around 575 nm; in contrast, there was no sign of any peaks in Figure 5.12.b. The hBN Raman peak is expected to appear around 574 nm (very close to the 575 nm I see in the spectrum); however, because of the relatively broad spectrum at 575 nm, I attribute this peak to defect centre in hBN, similar to the one reported in [75]. I checked power saturation and second–order correlation measurements; however, I did not observe any saturation in intensity or antibunching.

Next, I treated the sample for the 2nd time (with the same recipe), and these results are shown in Figure 5.12.c and Figure 5.12.d. After this step, I observed that the peak intensity at 575 nm dropped, whereas the intensity of defects in Figure 5.12.d increased. The peaks around 548–561 nm mainly belong to the substrate Raman peaks.

5.6 Annealing approach

According to the treatment results, it is evident that annealing can generate defect centres in hBN. Therefore, I explored this approach in this section with two different methods. In the first method, consecutive annealing on a sample at medium temperature was studied. Next, I investigate annealing at high temperatures. In what follows, the results of these experiments are elaborated.

5.6.1 Consecutive annealings at medium temperature

This study aims to check whether consecutive annealings on one sample can create colour centres; in addition, I want to investigate the effect of further annealings in one sample. Therefore, I selected a sample and characterised it before and after each anneal. According to the characterisation before annealing, I could only find one emitter in the sample. The PL raster scan of this area and the PL spectrum of the emitter found in the same area are shown in Figure 5.13.a and Figure 5.14.a, respectively. This emitter exhibited a weak emission of around 580 nm. Next, I annealed the sample at 400 °C. Figure 5.13.b indicates three areas with colour centres after annealing at 400 °C. I did not find any emitters in the area shown in Figure 5.13.a. It is be noted that after this step, I observed the appearance of diffraction–limited spots in the middle and edge of the flakes. After characterisation, I found different defects and categorised them as shown in Figure 5.14.b.

In the next step, I annealed the sample at 500 °C, and the results of PL raster scans are depicted in Figure 5.13.c. I observed diffraction–limited spots on two flakes presented in Figure 5.13.b and new bright spots appeared in a new flake. These bright spots were less bright compared to the previous step. Figure 5.14.c illustrates three different groups of defects after annealing at 500 °C. The intensity of defects decreased in the 2nd annealing. Also, there is no sign of narrow linewidth emitters.

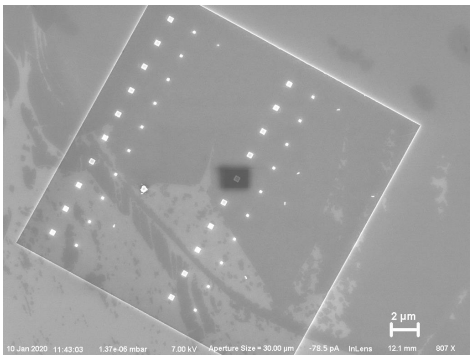

Figure 5.11: SEM hBN on SiO_2 nanostubs. All the region is covered by hBN. The contrast between two areas is related to the difference in their thickness. The scale bar shows 2 µm.

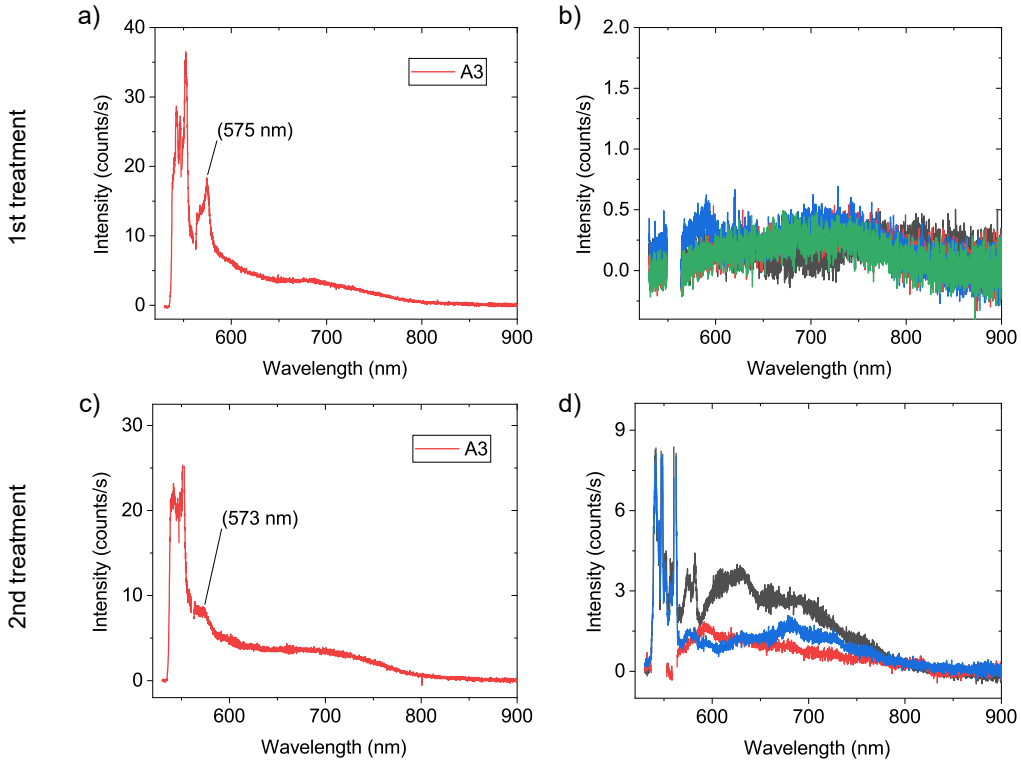

Figure 5.12: PL spectra of hBN on SiO_2 nanostubs. PL spectra after (a,b) the 1^{st}, and (c,d) the 2^{nd} treatments. Figures (a,c) and figures (b,d) were taken from the area 1 and area 2, respectively. Before treatment, there was no sign of PL enhancement in this area.

Finally, I annealed the same sample for the 3^{rd} time. The PL raster scan and the PL spectra are shown in Figure 5.13.d and Figure 5.14.d, respectively. According to these results, the intensity of spectra in all groups decreased. Moreover, there was no sign of diffraction–limited spots on the studied flakes. In Figure 5.14.b, Figure 5.14.c, and Figure 5.14.d, spectra were taken from bright spots in Figure 5.13.b, Figure 5.13.c, and Figure 5.13.d.

5.6.2 Single annealing at high temperature

In the following method, I investigated the possibility of generating emitters at high temperatures. For this purpose, I chose 850 °C and 1000 °C while other parameters were kept unchanged. The recipe for the annealing is discussed in subsection 3.4.2. In this study, I only annealed each sample once. Figure 5.15 depicts the PL raster scan of the areas that were studied. The left and right columns show 850 °C and 1000 °C areas, respectively. Both methods could create diffraction–limited spot–size emitters. Some emitters appeared at the flake's edge or a crack, while others appeared inside the flake.

Next, I explored PL spectra to find single–photon centres. Figure 5.16 shows the PL spectroscopy results characterised using the $4f$ confocal microscopy described in

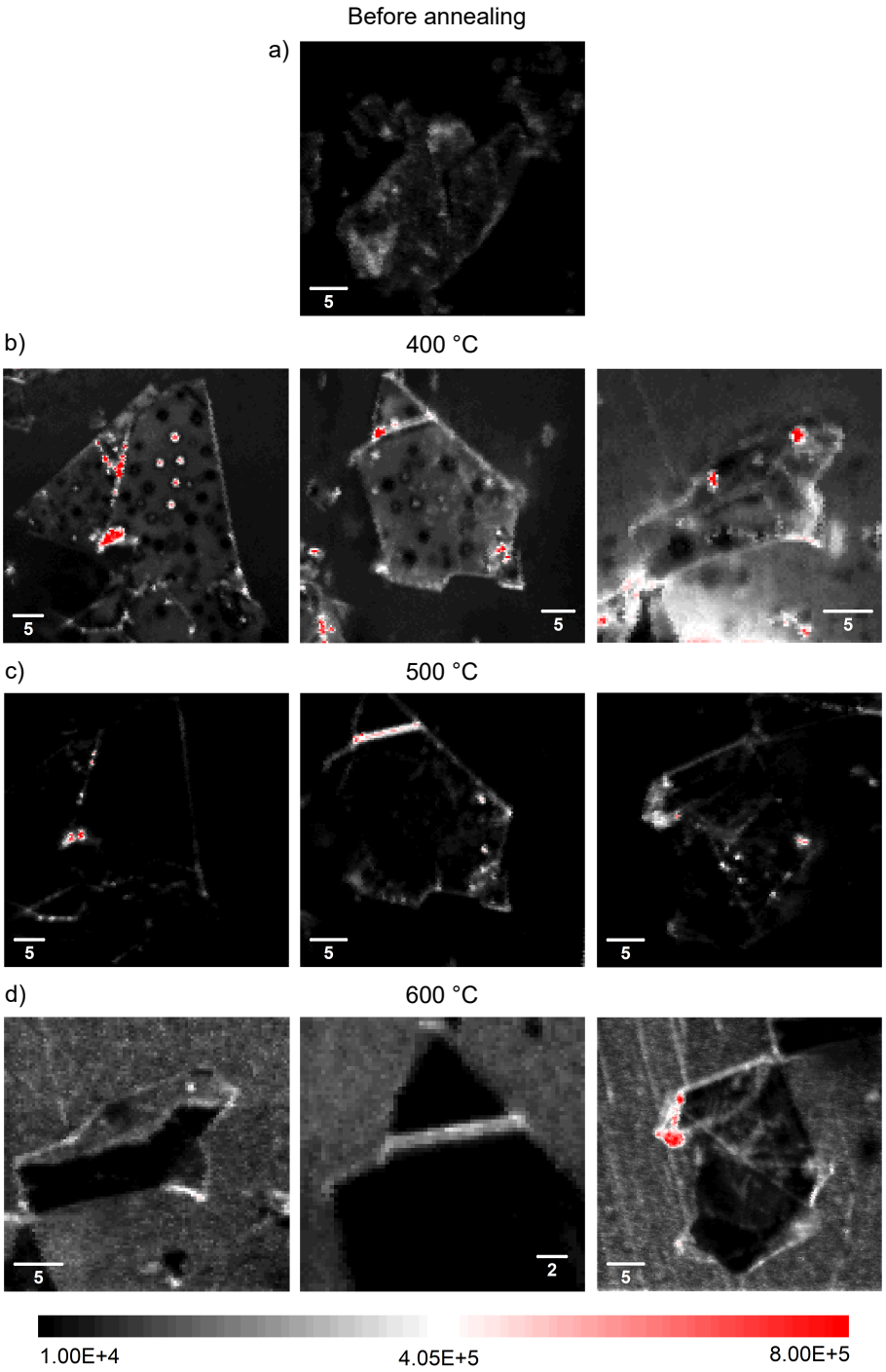

Figure 5.13: The PL raster scan of consecutive annealings at medium temperature on single sample. The PL scan for a) before annealing, annealed at b) 400 °C, c) 500 °C, and d) 600 °C on the same sample. The red colours indicate high PL intensity areas.

subsection 3.2.1. I used the same definitions used in Section 5.4 to categorised the PL spectra. Results of 850 °C annealed samples (left–hand column in Figure 5.16) show that the possibility of creating defect centres a high, but a majority of them have higher linewidths (FWHM $\geqslant$ 22 & 57 nm). In contrast, the likelihood of creating defects with narrow linewidth (FWHM $\leqslant$ 14 nm) in a wide range of wavelengths is

higher for 1000 °C annealed samples (left–hand column in Figure 5.16).

The big challenge I faced with this approach was the count rate stability of these emitters; more specifically, I observed that most single–defect–like emitters vanished within a day or a few days. Figure 5.17 depicts power saturation measurement from two emitters in 1000 °C annealed samples; I used spectral filtering to remove laser

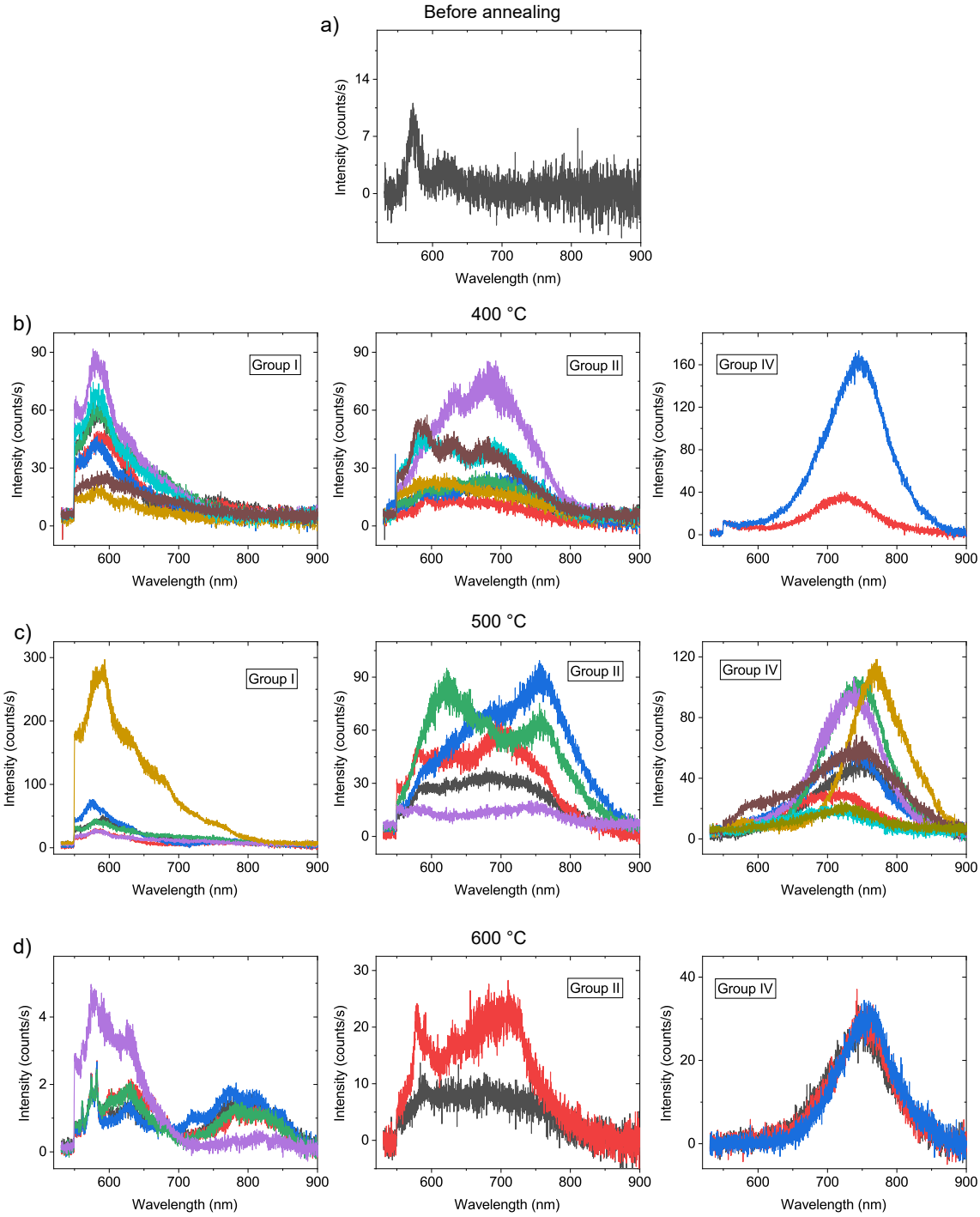

Figure 5.14: The PL spectra of consecutive annealings at medium temperature on single sample. The PL spectra for a) before annealing, annealed at b) 400 °C, c) 500 °C, and d) 600 °C on the same sample.

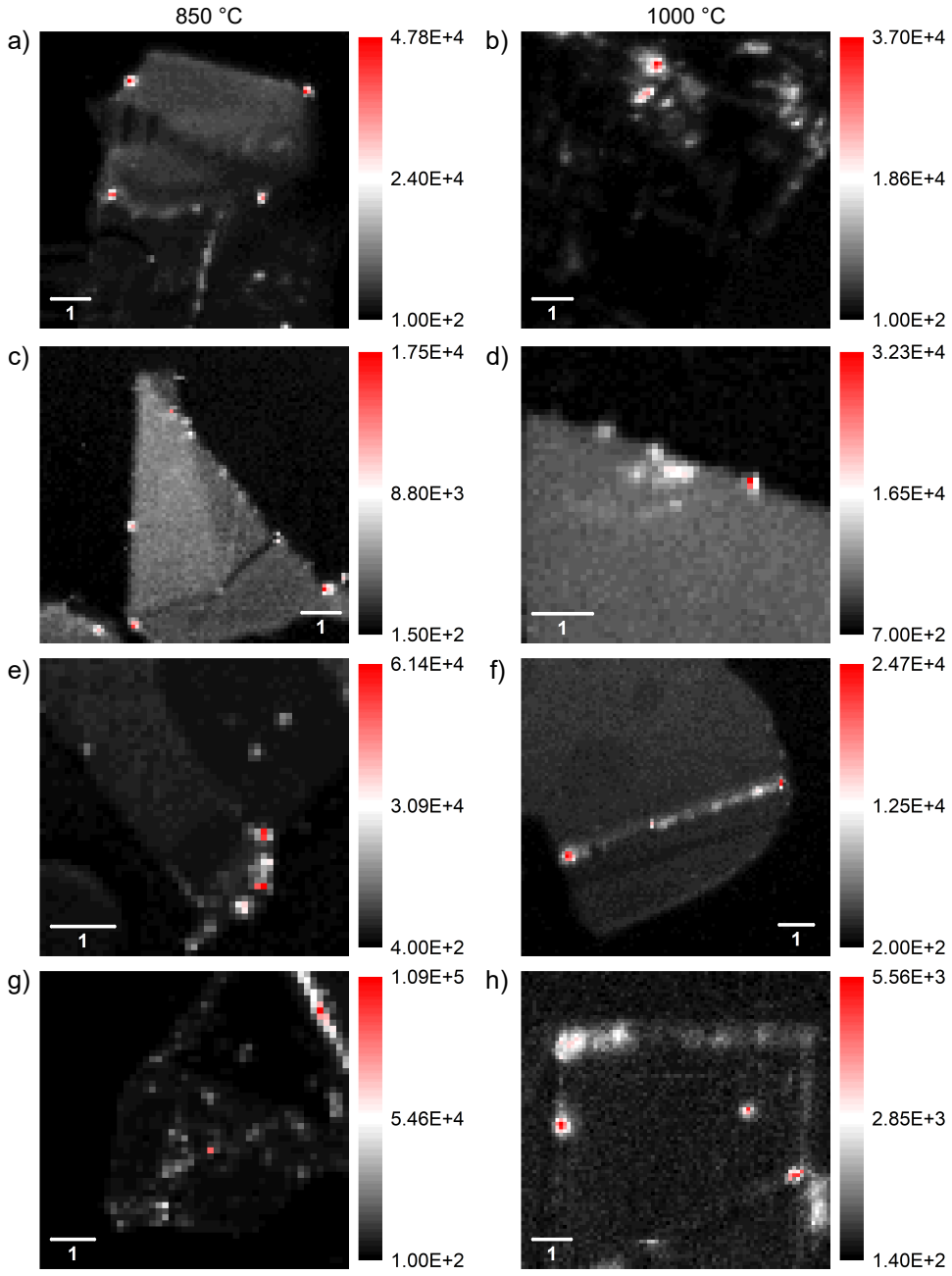

Figure 5.15: The PL raster scan of single annealing at high temperature. The PL scans for annealed samples at 850 °C (left–hand column) and 1000 °C (right–hand column). The red colours indicate high PL intensity areas.

and background emissions (mainly Raman signals from the substrate); Figure 5.17.a shows Background corrected spectra from the point defect and after using filters (700 nm long–pass and 900 nm short–pass), and Figure 5.17.c illustrates spectra before adding filter (600 nm long–pass) to the setup. Both point defects exhibit saturation behaviour with saturation intensity (power) of 18 ± 1 kHz (0.23 mW) and 114 ± 3 kHz (1.3 mW), respectively. In Figure 5.17.b and Figure 5.17.d, BGhBN represents the background date taken from the hBN flake. I were not able to perform second–order correlation measurement as both of these emitters disappeared.

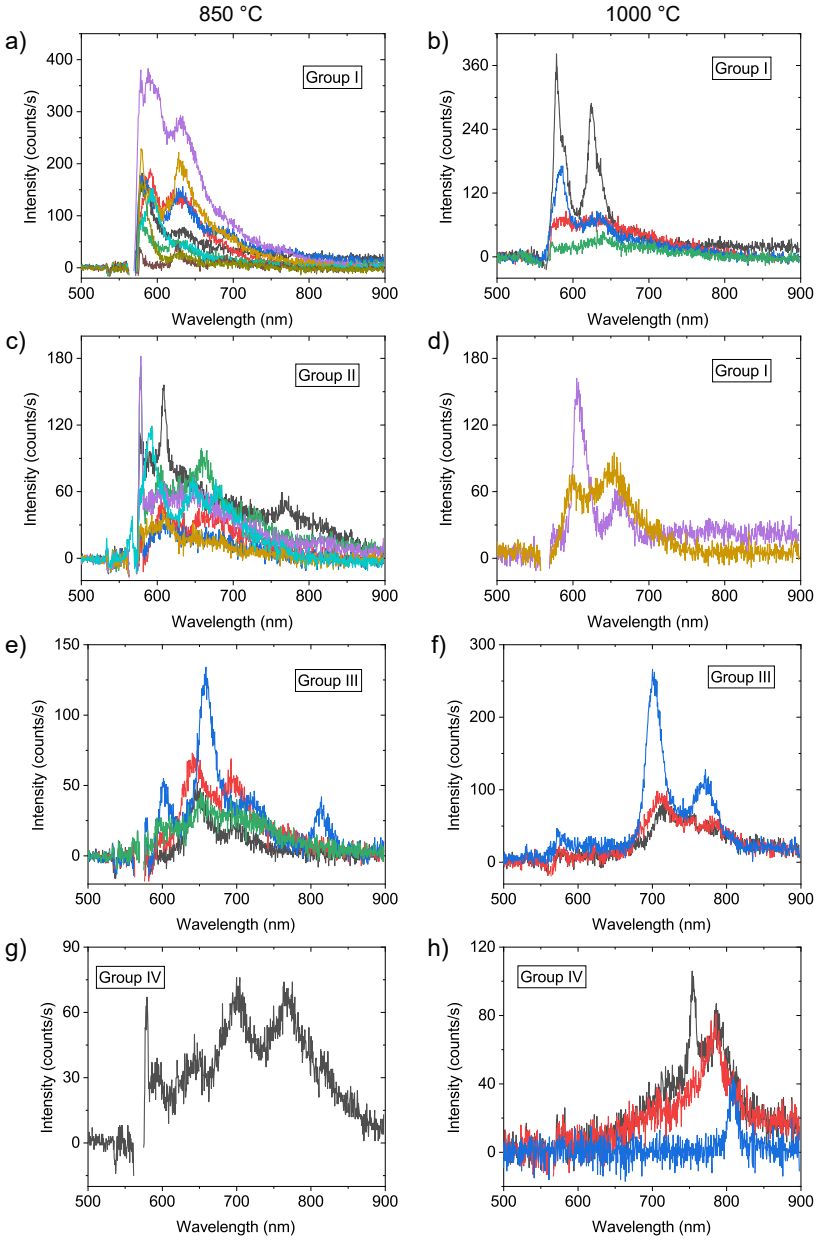

Figure 5.16: Single annealing at high temperature. The PL spectra for annealed samples at 850 °C (left–hand column) and 1000 °C (right–hand column) for (a,b,d) group I, (c) group II, (e,f) group III, and (g,h) group IV.

5.7 Kr^+ irradiated approach

Kr^+ irradiated hBN samples were studied in the final step. Kr^+ was chosen because it is optically inactive, and it would possibly create vacancies in the crystal. Different irradiation conditions were investigated for this study to determine the optimal condition for generating a single defect centre. In what follows, I will elaborate on them.

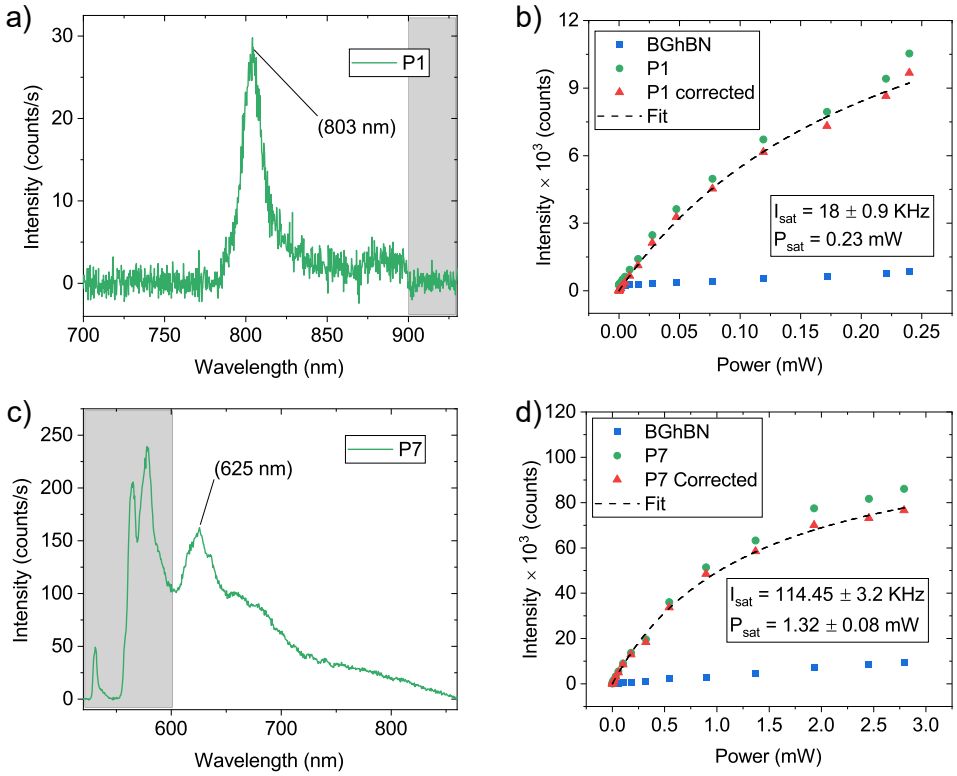

Figure 5.17: The power saturation measurement of two emitters after annealing the sample at 1000 °C. a) Background corrected PL spectrum of a point defect around 803 nm. b) Power saturation measurement from the defect centre showed in (a). The fitted values for the saturation intensity and power are 18 ± 1 kHz and 0.23 mW. c) Background corrected PL spectrum of a point defect around 625 nm. The grey window shows the filtered region used in saturation study. d) Power saturation measurement from the defect centre showed in (c). The fitted values for the saturation intensity and power are 114 ± 3 kHz and 1.3 mW.

5.7.1 Fluence study

In this approach, I first studied samples with different Kr ion fluences while the ion energies remained unchanged at 25 eV. Before irradiation, samples were annealed at 220 °C for 30 min in an ultra–high vacuum environment (around 10^{-7} mbar). This pre–anneal step has different purposes; first, it helps to remove surface contamination left from the polymer–based transfer of flakes on the SiO_2/Si substrate. Second, it may help relax[1] some chemical bonds in the hBN crystal lattice. In addition, there is no evidence that low–temperature annealing will result in defects in hBN. So, I can conclude this pre–anneal step is not responsible for defects generated in irradiated samples.

To find out which fluence has better PL characteristics (in order to create single photon source), I studied five samples; The first sample was a non–irradiated sample which I considered as the reference, and the remaining four were irradiated with the

[1]relaxation of bonds between atoms with fewer neighbors

fluence of 10^{11} cm^{-2}, 10^{12} cm^{-2}, 10^{13} cm^{-2}, and 10^{14} cm^{-2}, but with the same ion energy (25 eV). The PL raster scans from different flakes in these samples are depicted in the Left–hand side column of Figure 5.18. The PL scans were taken by the PL setup discussed in subsection 3.2.1. Next, all samples were annealed under the same conditions (nitrogen environment, 1 atm, 875 °C, 8 min) and later exposed to oxygen in plasma ash (50 W, 5 min). Annealing at high temperatures is essential in "healing" the crystal lattice and allowing impurities or vacancies to migrate within the lattice [152, 153]. Healing the crystal lattice means reconstructing the damaged lattice. I chose this temperature because it is shown that it is possible to create defect centres under this condition [92, 154, 155]. In addition, my earlier investigations revealed that the oxygen plasma ash would reduce the background fluorescence. Therefore, I exposed all samples to oxygen in a plasma asher. So, the term "anneal/ash dual treatment" in the "Kr^+ fluence" study stands for these two steps. The right–hand column of Figure 5.18 shows the PL raster scans from the same areas after the annealing step.

To investigate the effect of "Kr^+ fluence" and treatment, I first need to analyse background emissions. Because irradiation can have dissimilar impacts on different materials, I separated the substrate (SiO_2) background emission from the flake background emission. Figure 5.19.a and Figure 5.19.c show the substrate and flake background emissions before annealing, respectively. The substrate and flake background emissions after annealing are shown in Figure 5.19.b and Figure 5.19.d, respectively. My observations are listed as follows:

- It can be seen that at higher fluences ($\geqslant 10^{13}$ cm^{-2}), the PL increases with higher fluences. At lower fluences ($\leqslant 10^{12}$ cm^{-2}), the irradiation has less impact on the substrate and the flake backgrounds.

- Nearly all flakes on all samples showed short–lived fluorescence that bleached.

- After annealing, the fluorescence from all samples was reduced.

- A peak around 700 nm arises from the substrate, and the origin of this emission is unknown.

- Other features, such as a bump around 800 nm and a minor peak around 640 nm, are appeared in both substrate and flakes. The origin of these features is unknown.

- The peak around 575 nm was seen in both substrates and flakes before the annealing; however, after the annealing, this peak at 575 nm only appeared on flakes.

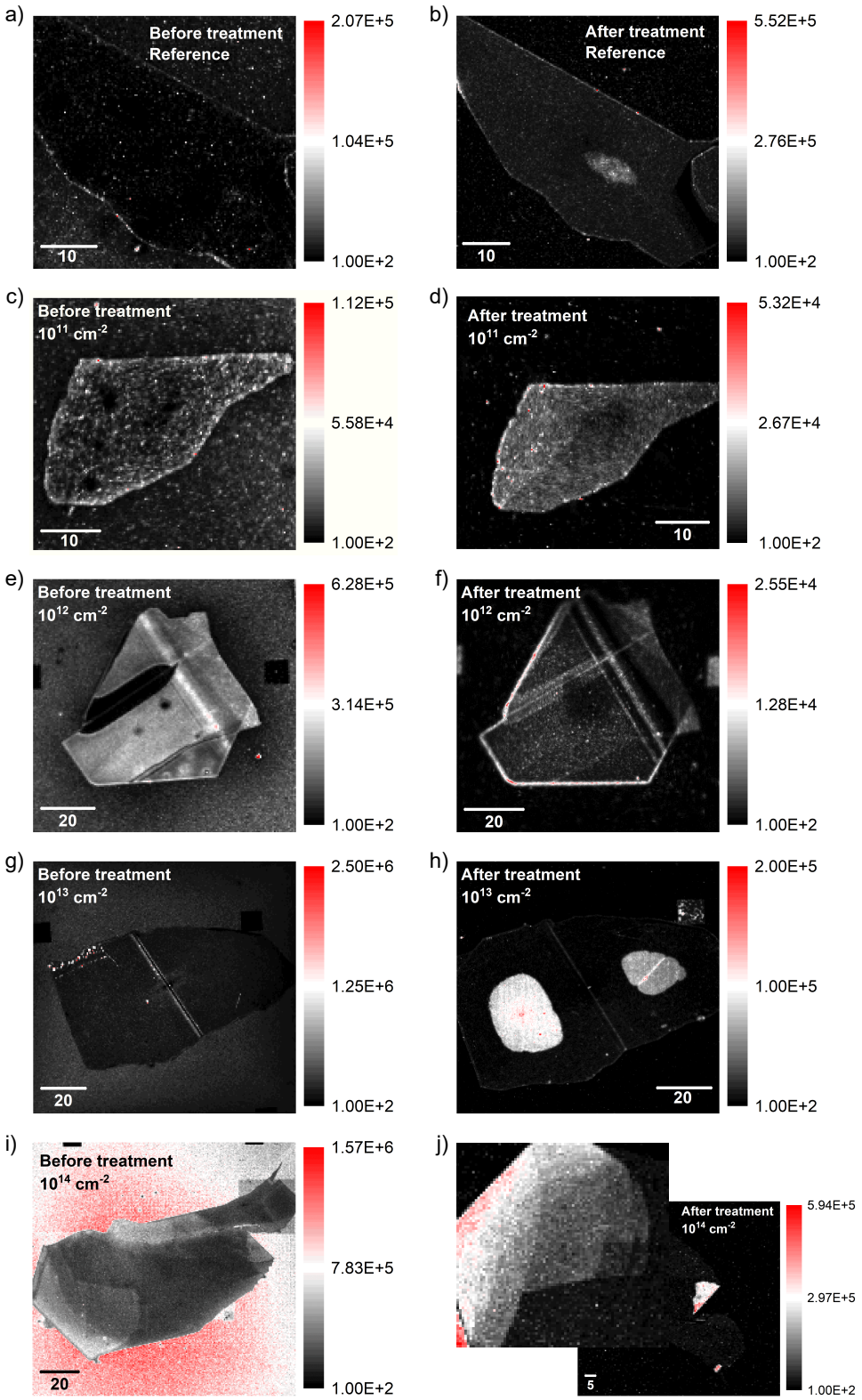

Figure 5.18: The PL raster scans from samples with different fluences. PL scans before (left–hand column) and after annealing (right–hand column) for (a,b) reference, (c,d) 10^{11} cm^{-2}, (e,f) 10^{12} cm^{-2}, (g,h) 10^{13} cm^{-2}, and (i,j) 10^{14} cm^{-2} samples, respectively. These samples were irradiated with the same ion energy (25 eV). The scale bar is in µm.

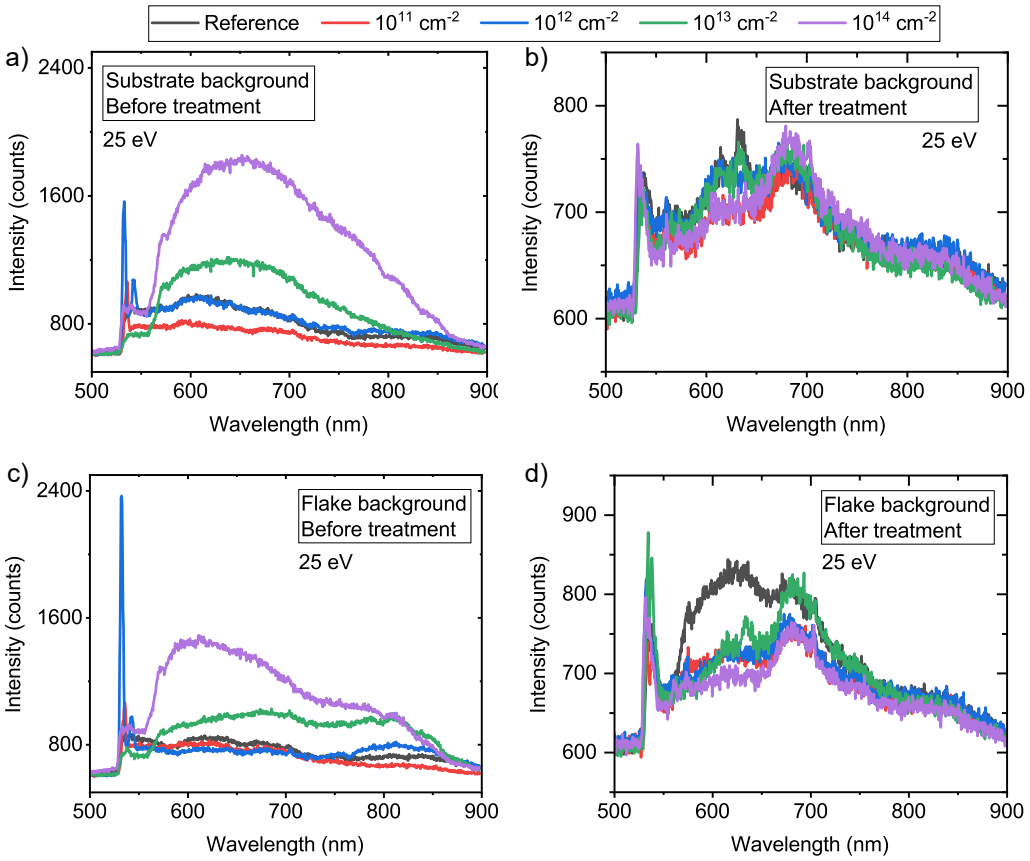

Figure 5.19: Fluence study of Kr^+ irradiated samples (Backgrounds). (a,c) Substrate and flake backgrounds before annealing, respectively. (b,d) Substrate and flake backgrounds after annealing, respectively. In all figures, red, blue, green and pink lines represent fluences of 10^{11} cm^{-2}, 10^{12} cm^{-2}, 10^{13} cm^{-2}, and 10^{14} cm^{-2}, respectively. These samples were irradiated with the same ion energy (25 eV). The black line indicates the reference sample which is not being irradiated.

After identifying the impact of irradiation and a post–annealing on the substrate and the flake's backgrounds, I explored PL spectra from bright spots on these flakes. These results are shown in Figure 5.20, where the left–hand and the right–hand columns indicate before and after annealing, respectively. I subtracted flake background data, Figure 5.19.c (Figure 5.19.d), from all data shown in the left–hand (right–hand) column in Figure 5.20 to consider the effect of irradiation on defects only before (after) annealing. Based on the pre–annealing results, it is clear that increasing fluence results in higher fluorescence intensity. In addition, the likelihood of creating an ensemble of defects increased at the fluence $\geqslant 10^{12}$ cm^{-2}. The impact of irradiation is insignificant at 10^{11} cm^{-2} as intensities of PL spectra are similar to the reference sample. After the annealing, I observed reductions in the PL intensities; however, in contrast to pre–annealing results where the fluorescence was bleaching gradually, I observed stability in intensity. I didn't observe any diffraction–limited spot from these flakes before or after annealing, which suggests no single defect centre was created.

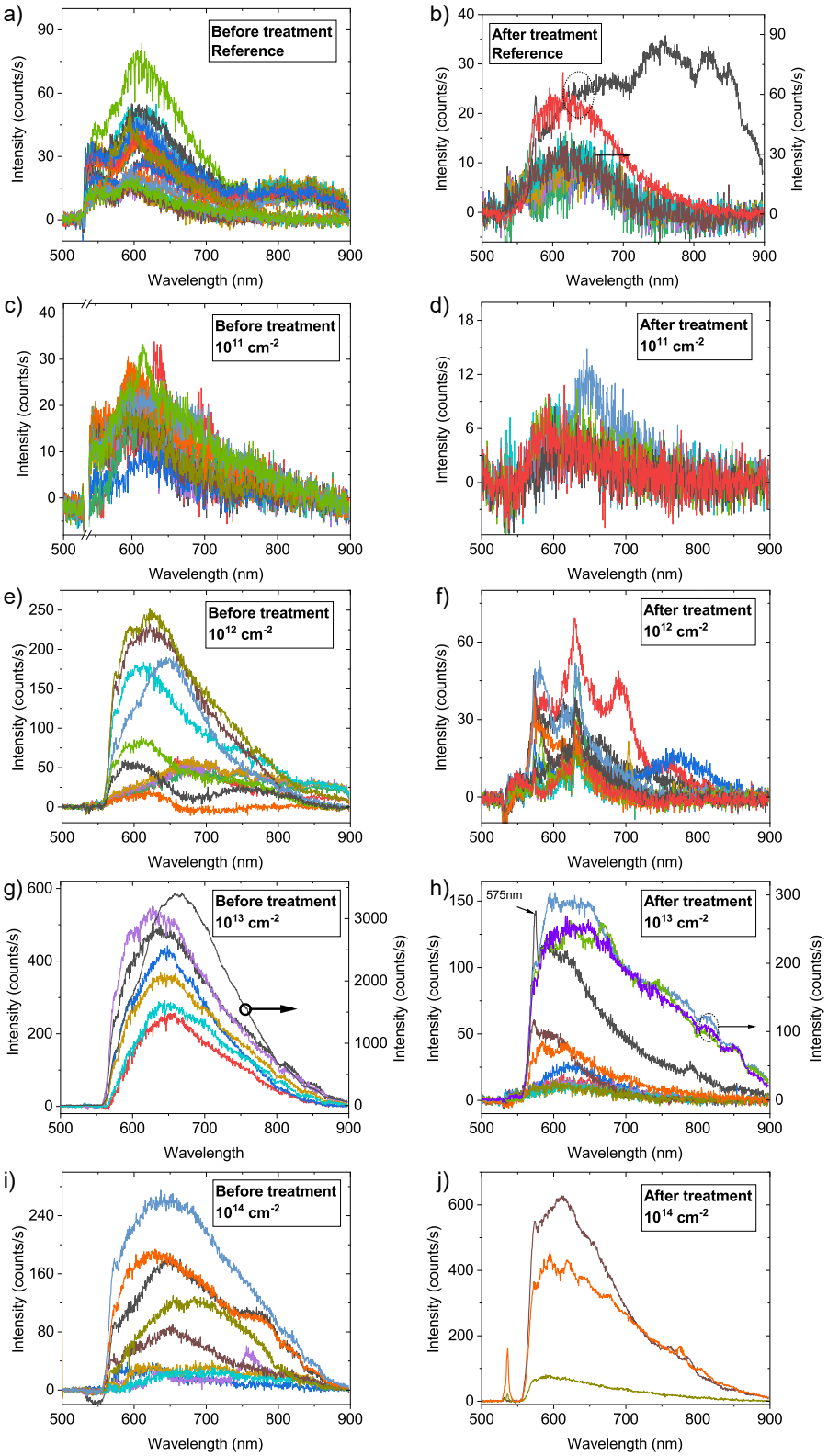

Figure 5.20: The PL spectra for different Kr^+ fluences. The PL spectra before (left–hand column) and after annealing (right–hand column) for (a,b) reference, (c,d) 10^{11} cm^{-2}, (e,f) 10^{12} cm^{-2}, (g,h) 10^{13} cm^{-2}, and (i,j) 10^{14} cm^{-2} samples, respectively. These samples were irradiated with the same ion energy (25 eV)

Based on the PL spectra shown in Figure 5.20, I decided to pick the fluence of 10^{12} cm^{-2} for the "energy study"; although the PL spectra before the annealing showed ensemble–like signatures, spectra showed recognisable peaks after the annealing. In addition, the flake's and the substrate's background emissions are negligible before and after the annealing (see Figure 5.19).

5.7.2 Energy study

In this study, I investigated samples with different Kr^+ ion energies while the ion fluence remained unchanged at 10^{12} cm^{-2}. Before irradiation, samples were annealed at 220 °C for 30 min in an ultra–high vacuum environment (around 10^{-7} mbar). This pre–anneal step has the same effect on samples as discussed in Section 5.7.1. I studied five samples to determine which ion energy has better PL characteristics. The first sample was a non–irradiated sample that I considered as the reference. The remaining four were irradiated with the energy of 50, 100, 150, and 200 eV but with the same ion fluence (10^{12} cm^{-2}). The PL raster scans from different flakes in these samples are depicted in the left–hand side column of Figure 5.21.

Next, all samples were annealed under the same conditions (Nitrogen environment, 1 atm, 800 °C, 30 min). Based on Figure 5.19, the background emission before annealing for fluence 10^{12} cm^{-2} has an insignificant impact; therefore, I avoided using plasma ash after the annealing. The right–hand column of Figure 5.21 shows the PL raster scans from the same areas after the annealing step. According to this figure, it is clear that there is no sign of a diffraction–limited spot size emitter. I analysed background emissions to investigate the effect of ion energy and post–annealing; my observations are listed as follows:

- Fluorescence emissions from flakes and substrates remained unchanged after irradiation which suggests ion energy ranging from 50–200 eV has a negligible impact on background emissions.

- Nearly all flakes on all samples showed short–lived fluorescence that bleached in sub–second timescale.

After identifying the impact of irradiation and annealing on the substrate and the flake's backgrounds, I checked PL spectra from bright spots on these flakes. These results are shown in Figure 5.22, where the left–hand and the right–hand columns indicate before and after annealing, respectively. Based on the before annealing results, higher energy irradiation seems to result in emissions around 500–700 nm; however, the emission increases around 600–800 nm after annealing. I couldn't observe any diffraction–limited single–photon centre from these samples. Also, my characterisations showed that these bright spots suffer from intensity instability

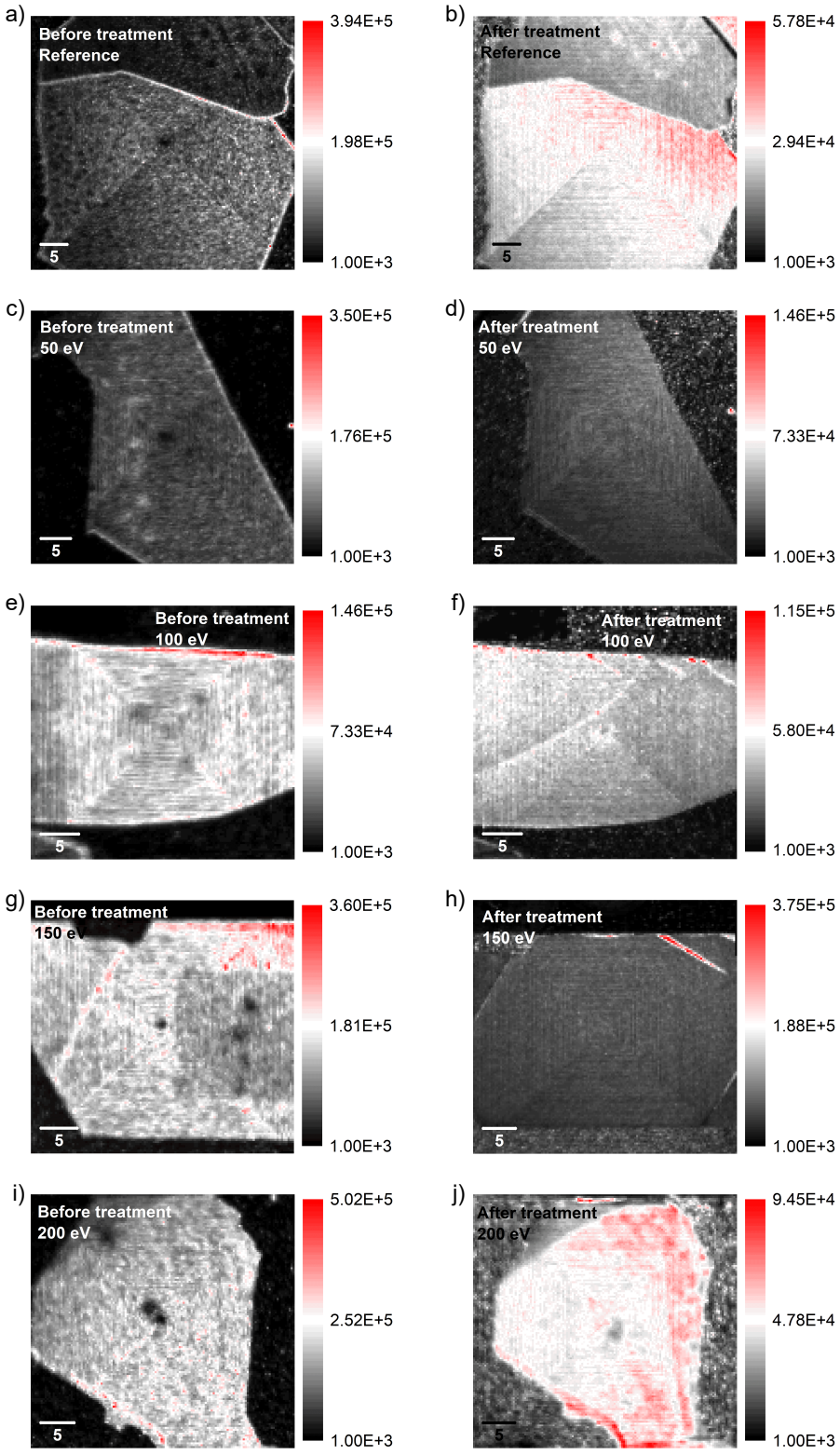

Figure 5.21: The PL scans for different Kr^+ energies. The PL raster scans before (left–hand column) and after annealing (right–hand column) for (a,b) reference, (c,d) 50 eV, (e,f) 100 eV, (g,h) 150 eV, and (i,j) 200 eV samples, respectively. These samples were irradiated with the same ion fluence (10^{12} cm^{-2}). The scale bar is in µm.

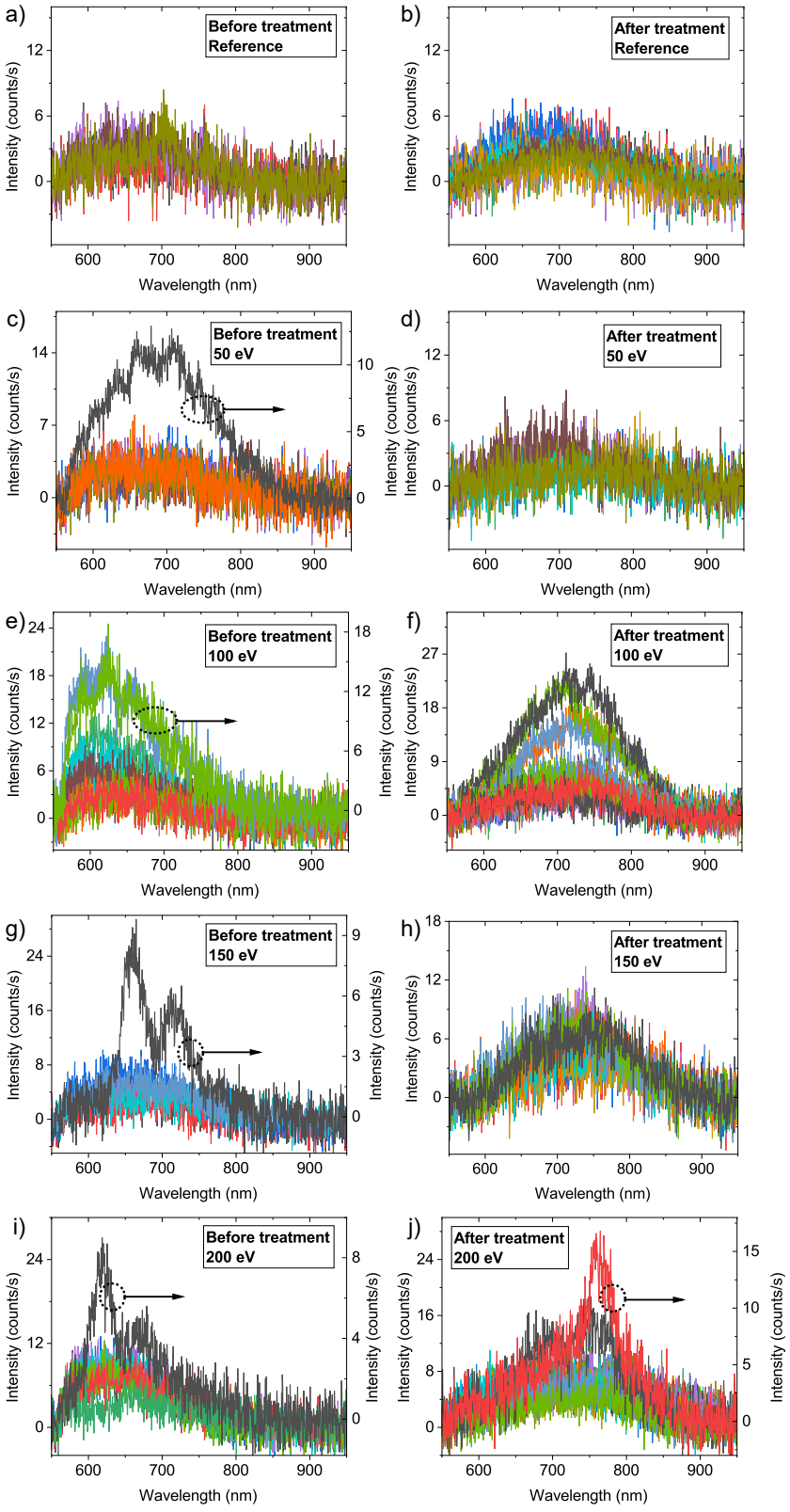

Figure 5.22: The PL spectra for different Kr^+ energies. The PL spectra before (left–hand column) and after annealing (right–hand column) for (a,b) reference, (c,d) 50 eV, (e,f) 100 eV, (g,h) 150 eV, and (i,j) 200 eV samples, respectively. These samples were irradiated with the same ion fluence (10^{12} cm^{-2}).

(50 % or more in less than 30 s). In particular, the characterisation of black–line spectra in Figure 5.22.g and Figure 5.22.i revealed that defect centres disappeared at long exposure (30 s). After annealing, I observed better stability in general (less than 20 % in more than 1 min); however, I still observed unstable centres. For example, the peak around 770 nm indicated by the red line in Figure 5.22.i disappeared at long exposure (30 s). The origin of these behaviours is not clear to us.

This study needs further investigations; however, based on PL results for 150 eV and 200 eV, it is possible to generate a single–photon centre using Kr^+ ions. Although I could not observe any diffraction–limited spot, I observed brighter spots which exhibited higher intensity and broader spectrum. After annealing, I could not find those brighter spots in their same locations. Among different reasons for such a behaviour, below cases can be addressed:

- The impurity–vacancy type defect that generated that brighter spot migrates to different areas after annealing after gaining enough energy; this energy is the so–called "threshold displacement energy".
- Annealing helps to heal the damaged crystal lattice .
- Annealing changes the strain because the SiO and hBN expand at different rates, and this strain might alter the position of the emitters.

5.8 Discussion

In this study, I showed different approaches are capable of generating defect centres in hBN. However, in most cases, I observed the creation of ensembles of defects.

The cleanroom recipe could be used to create and stabilise defect centres in hBN. After the etching step, new generated point sources in hBN crystal blinked and mostly bleached quickly; however, after annealing, I observed significant stability in emission, especially at higher temperatures. Another interesting result from this work is the effect of plasma ash on suppressing background fluorescence and increasing the purity of single photon emission. It has been studied that based on the annealing temperature condition (in my case, 600 °C) and the wavelength of the emitted PL, the non–bridging oxygen hole centre could be a candidate for high background fluorescence (figures 4, 14, 15; [156]). When I exposed the sample to plasma ash, supplied O– (or O_2) had enough energy under RF plasma power to attach to these defect centres on the substrate and reduce SiO intensity from the background.

The combination of the strain and treatment is the closest approach I could create defects with high consistent spectra. In the CVD hBN on silicon nanostubs

sample, I observed many emitters with emissions almost at 600 nm and some degree of saturation of photon intensity with laser power, however, without any antibunching behaviour. One reason could be that the point source might consist of multiple defects. In the CVD hBN on SiO_2 nanostubs sample, I observed high intensity from the background after each treatment, especially on the nanostubs. The reason for this behaviour is still unknown but based on my observation, Raman signals from SiO_2/Si substrate increase significantly after each treatment. This might be related to the higher scattering of light into the lens by the nanostubs.

In the annealing study, I observed that consecutive low–temperature annealing on the same flake only creates more defects; however, single annealing at high–temperature results in narrow linewidth spectra with power saturation behaviours. These results suggest that annealing is the most promising approach to creating narrow linewidth emitters, among other studied techniques. The main challenge in this step is the stability of the centres, and more studies are required to unravel this issue.

Finally, the irradiation study showed that Kr^+ ions could create single defects and ensembles of defects; however, single defect centres are very unstable. Although annealing the Kr^+ irradiated samples could improve the stability of the ensemble of defects, I did not observe any improvement in the stability of single defect centres. This approach requires more investigation.

CHAPTER 6

Coherent control of electron spin of V_B^- in hBN

6.1 Introduction

Some colour centres in hBN exhibit attractive quantum emission properties such as high brightness at visible wavelength, well–matched to silicon detectors. In addition, some reports of transform–limited transitions with a high fraction of emission occurring through the ZPL [157]. If a defect could be identified that combines the excellent quantum emitter properties with a spin memory, this could provide a competitive system to build a spin photon interface. In addition, hBN can allow the spin defect to be placed close to the target of interest. In hBN, there are a few recent studies on single bright defects; Exarhos *et al.* studied the first type of paramagnetic defect with a single quantum emission characteristic [158]. A few years later, Stern *et al.*. reported a new paramagnetic defect in which the ODMR signal emerged from a diffraction–limited spot size emitter with single–photon characteristics [159].

Nevertheless, most of the work has focused on boron vacancy ensembles. Although these centres suffer from low brightness, they are easy to generate, and their internal energy levels have been theorised, which allow facile spin–pumping. Many groups reported ODMR from this centre, and these papers reported spin–triplet ground state in V_B^-, which was also theoretically proven from this defect centre [43, 96, 97, 110]. In this work, we focus on carbon–irradiated samples and aim to unravel the spin properties of boron vacancy in this sample. It is expected that, like other III–V materials, the electron spin coherence times are limited by the nuclear spin environment.

In this work, all data was acquired by the author with the exception of Figure 6.2 and Figure 6.9.

6.2 V_B^- centre

6.2.1 Defect system

The negatively charged boron vacancy centre consists of a missing boron atom surrounded by three equivalent nitrogen atoms in the hBN lattice. A 2D view of the defect inside the crystal lattice is depicted in Figure 6.1.a. The defect exhibits room–temperature phonon–broadened PL and photoluminescence excitation emissions around 800 nm and 478 nm, respectively [96, 100].

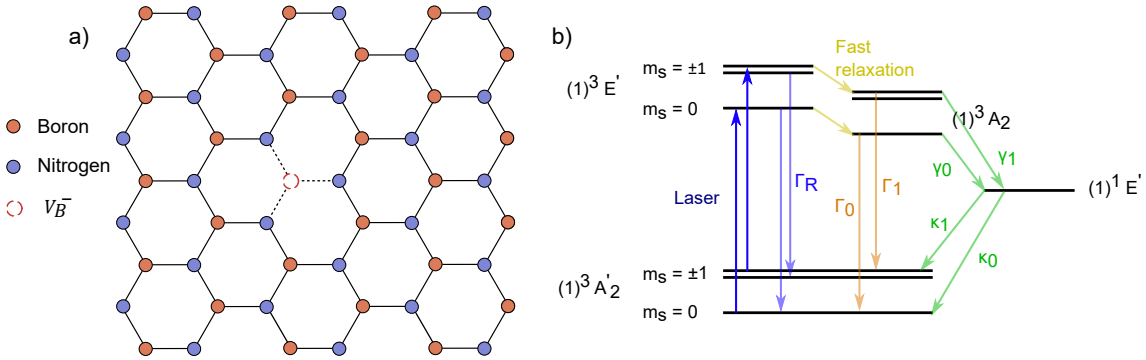

Figure 6.1: V_B^- defect system. a) Schematic of a hBN monolayer and its hexagonal crystal structure with boron (red) and nitrogen (blue) atoms. The hollow circle indicates the defect. b) Energy level diagram of the defect. (Re–plotted from ref. [100, 110])

As depicted in Figure 6.1.b, Reimers *et al.* predicted that the relaxation of the optical triplet ES, $(1)^3A_2$, to singlet meta–stable state, $(1)^1E'$, is dominated by ISC; $1/\gamma_1$ was calculated to be 1.7 ns at room temperature. On the other hand, the radiative decay rate of $(1)^3E' \rightarrow (1)^3A_2'$ was calculated to be $1/\Gamma_R = 11\,\mu s$ [110]. Baber *et al.* measured the spin–dependent PL decay rate as $\gamma_0 = 1.01$ GHz (0.99 ns) and $\gamma_1 = 2.03$ GHz (0.49 ns). This is in consistent with estimates of ISC times but fast compared to the estimated radiative rate calculated in [100]. Because of its very weak emission, it is suggested that the defect spectrum features a low quantum yield (possibly due to its ISC to singlet state, i.e. $(1)^1E'$), but it is strong enough to display ODMR contrast.

As the relaxation mechanism is primarily dominated by γ_0, γ_1, understanding the physics of spin–triplet systems, i.e. $(1)^3A_2'$ and $(1)^3A_2$, is an crucial step to perceiving the spin readout in ODMR.

6.2.2 Spin–triplet system ($S = 1$)

The Hamiltonian of a spin–triplet state ($\mathcal{H}$), like the ground/excited state of V_B^-, is governed by three terms (Equation (6.1)): the first term ($\mathcal{H}_S$) refers to the electron spin ($S = 1$) only. The second term ($\mathcal{H}_{SI}$) explains the HFI between electron spin and the nuclei surrounding the electron spin. The final term ($\mathcal{H}_I$) is related to nuclei–related contribution to the system's total energy. These terms are written in Equation (6.2), Equation (6.3), and Equation (6.4).

$$\mathcal{H} = \mathcal{H}_S + \mathcal{H}_{SI} + \mathcal{H}_I \tag{6.1}$$

$$\mathcal{H}_S = \underbrace{D(S_z^2 - S(S+1)/3) + E(S_x^2 - S_y^2)}_{\text{ZFS}} + \underbrace{g_e \mu_B \mathbf{BS}}_{\text{e-Zeeman}} \tag{6.2}$$

$$\mathcal{H}_{SI} = \underbrace{\sum_i \mathbf{S}.\mathbf{A_i}.\mathbf{I_i}}_{\text{HFI}} \tag{6.3}$$

$$\mathcal{H}_I = \underbrace{Q(I_z^2 - I(I+1)/3)}_{\text{QI}} - \underbrace{g_N \mu_N \mathbf{BI}}_{\text{n-Zeeman}} \tag{6.4}$$

In the above equations:

- S is the total electron spin. For V_B^- (both ground/excited states), due to its two unpaired electrons, S equals 1, and the S_{xyz} are spin–1 operators.
- $\mathbf{I}$ is the vector of the nuclear spin Pauli operators corresponding to the nuclear spin. For the case of V_B^-, nuclear spin is equal to 1 (^{14}N).
- D and E describe the zero–field axial and off–axial (transverse) components of the ZFS parameter, respectively. The E parameter is often attributed to the strain parameter.
- g_e and g_N are the electron Landé g–factor and nuclear Landé g–factor, respectively. Landé g–factor is a tensor operator. g_N is an isotope–dependant parameter.
- μ_B and μ_N are the Bohr magneton and the nuclear magneton, respectively, and both of them are constant.
- $\mathbf{B}$ is magnetic flux density.
- Q is the quadrupole interaction constant induced by electric field gradients at the defect location.
- $\mathbf{A_i}$ is the HFI tensor of the i–th nuclear spin.

When a boron atom removes from a pristine hBN layer to make V_B^-, dangling bonds appear at each neighbouring nitrogen atom in both σ and π electronic systems, making six orbital levels associated with the defect. The theoretical calculations suggest that these six levels sit in the band gap of hBN [110]. A negatively charged boron vacancy surrounded by three equivalent nitrogen atoms with the nuclear spin of one ($\mathbf{I} = 1$) in the first and nearest neighbour. These atoms are strongly coupled to the V_B^- via hyperfine interaction [96]. Ab initio analysis for this vacancy indicates that the hyperfine coupling constant of V_B^- with ^{14}N nuclei in the first neighbour is 10 times bigger than the ^{14}N nuclei in the second neighbour and ^{11}B nuclei in the first neighbour [63]. It should be noted that the z–axis is perpendicular to the hBN crystal (multilayer). In the following, mentioned parameters the above will be discussed in more detail in the context of the ODMR.

6.3 Optically detected magnetic resonance

6.3.1 Electron spins interaction

In zero magnetic field (**B**), GS and ES split into three levels as shown in Figure 6.1.b. Zero–field splitting of the electronic states or ZFS is associated with spin–spin and spin–orbit interactions (first and second–order components of electron spin interaction, respectively). Spin–orbit interaction is relatively weak in hBN. Therefore spin–spin interaction dominates the electron spin interaction mechanism in V_B^- defect [158]. In other words, spin–spin interaction between unpaired electrons causes the ZFS between the $|0\rangle$ and $|\pm1\rangle$ states.

Spin–spin interaction is represented by the symmetry of the defect along the z– and (x,y)– directions (check ZFS term of $\mathcal{H}_S$ in Equation (6.2)). D and E, axial and off–axial ZFS parameters, are determined by ellipsoidicity and rhombicity of the electronic wavefunction distribution, respectively. V_B^- defect has intrinsic D_{3h} local point–group symmetry. Due to this high–symmetry case (i.e. D_{3h}), the E parameter in Equation (6.2) vanishes [158]; however, under strain, the symmetry reduces to C_{2v} symmetry [63, 110]. This new symmetry results in a non–zero E parameter. Consequently, GS and ES orbital doublet (D_{3h}) split into a non–degenerate orbital–singlet Hamiltonian (C_{2v}). In contrast to E_{GS}, E_{ES} varies with temperature, suggesting that strain is the possible scenario [160]. Energy levels of electron spin $|\pm1\rangle$ states are shifted under a continuous and static DC magnetic field, and this further splitting is caused by electron Zeeman interaction. In order to account for both ZFS and Zeeman splitting, one can use the below equation:

$$\nu_{\pm1} = \frac{1}{h}(D \pm \sqrt{E^2 + (g_e \mu_B B)^2}) \tag{6.5}$$

in which ν_{+1} and ν_{-1} are the transition frequencies between $|0\rangle \leftrightarrow |+1\rangle$ and $|0\rangle \leftrightarrow |-1\rangle$, respectively. This equation ignores the hyperfine interaction and is valid when the magnetic field and the defect's quantisation axis are aligned. $g_e \mu_B B/\hbar$ is the Zeeman term in the above equation, and the rest are ZFS–related.

6.3.2 CW ODMR

To extract D and E parameters, CW ODMR was performed. The sequence utilised during this study is shown in Figure 6.2.a. The laser illumination and the photon counting are executed continuously, and MW frequency is swept. When MW frequency is at resonance with two electronic states (i.e. $|0\rangle \rightarrow |+1\rangle$ or $|0\rangle \rightarrow |-1\rangle$ in Figure 6.1), the fluorescence detected by APD decreases, giving a series of dips. To

quantify the contrast between two states, the following formula was used:

$$C(t) = \frac{I_{on}(t) - I_{off}(t)}{I_{off}(t)} \tag{6.6}$$

where I_{off} and I_{on} are the PL intensity with the microwave off and on, respectively. This formula is independent of the type of study (ODMR spectrum, Rabi, etc.). To achieve better contrast, the defect system was excited by the high laser power. We read the number of counts around 7–8 Mtags/s during experiments. The spin–dependent fluorescence readout is taken over 2000 ns to maximise the signal strength. Photon shot noise is proportional to $\sqrt{N}$, where N is the number of

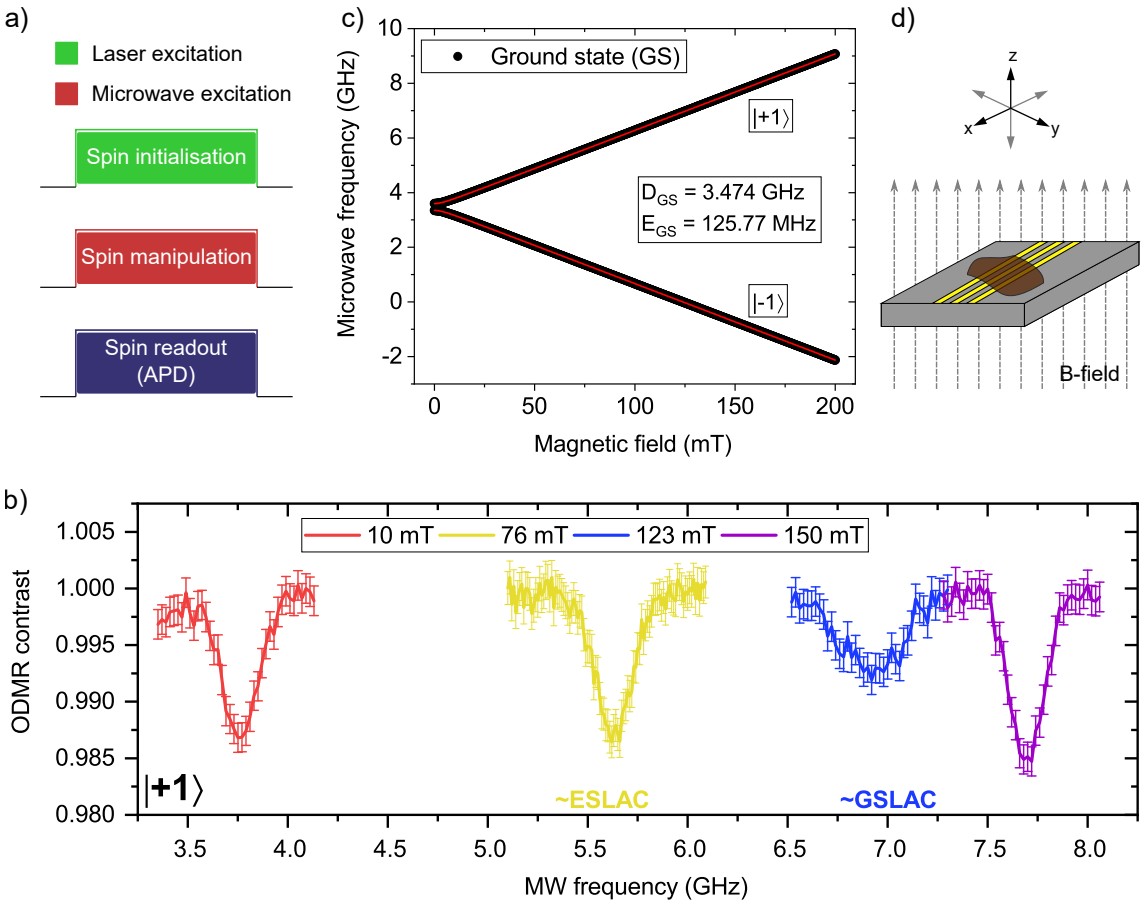

Figure 6.2: ODMR experiment. a) CW ODMR pulse sequence. The MW frequency is swept during the experiment. b) Examples of ODMR contrast in four different magnetic strengths. In this plot, only ODMR contrasts for $|0\rangle \leftrightarrow |+1\rangle$ transitions are shown. Error bars are defined as ± 1 SD of the photon shot noise and MW amplitude was set to 500 mV. c) The ground state energy level of the V_B^- defect. Electron spin resonance frequency of $m_s = \pm 1$ sublevels as a function of the external magnetic field. Black dots and red lines are experimental data and fitting results, respectively. At $B = 0$, the splitting results from ZFS, and it is lifted further at $B \neq 0$ due to Zeeman splitting. d) Direction of the static B–field applied to the sample.

Table 6.1: Electron Zeeman splitting parameters of spin Hamiltonian (T = 300 K)

Parameter	Value	Ref.
D/h	GS = 3.47 (GHz) ES = 2.09 (GHz)	[100, 161]
E/h	GS = 50 – 126 (MHz) ES = 74 – 154 (MHz)	[100, 160–162]
$\mid g_e \mid$	GS = 2.001 ES = 1.980 – 2.04	[100, 161, 162]

photons; exciting and collecting more photons per second, it is possible to measure small changes in the fluorescence intensity and consequently in the ODMR contrast. Figure 6.2.b illustrates the ODMR experimental result of the ground state. In Figure 6.2.b, ODMR contrast in four different magnetic strengths is shown; The error bar are defined as one standard deviation (SD) of the photon shot noise which is defined by $\sqrt{\bar{N}}$ where $\bar{N}$ is the total number of detected photons. MW amplitude was set to 500 mV.

Figure 6.2.c shows the ground state energy level of the defect. In this figure, central frequency of the ODMR contrast is plotted as a function of the magnetic field. The inset shows the fitting results derived by Equation (6.5). The ZFS parameters is derived as $(D/h)_{GS} = 3.474\,\mathrm{GHz}$ and $(E/h)_{GS} = 150\,\mathrm{MHz}$ with electron gyromagnetic ratio of $\gamma_e = 28\,\mathrm{MHz\,mT^{-1}}$. $(D/h)_{GS}$ is consistent with previous works; however, $(E/h)_{GS}$ is relatively large, perhaps due to high level of strain caused by use of carbon–irradiation to generate the defects. An overview of the measured parameters is summarised in Table 6.1.

Looking closely at ODMR spectrum result in Figure 6.3.a, one may notice that ODMR spectra dips are not quite Gaussian. Figure 6.3.b illustrates the same ODMR spectrum fitted by Bi–Gaussian fit, defined as:

$$\begin{aligned} C &= C_0 + He^{-0.5(\frac{f-f_c}{FWHM_{left}})^2} \quad (f < f_c) \\ C &= C_0 + He^{-0.5(\frac{f-f_c}{FWHM_{right}})^2} \quad (f \geqslant f_c) \end{aligned} \tag{6.7}$$

in which f, f_c, C, C_0 and H are MW frequency, centre frequency, ODMR contrast, fitting constant, and height, respectively. In addition, $FWHM_{left}$ and $FWHM_{right}$ indicate FWHM of the left and right Gaussian fits, respectively. It is clear that with this method, better fitting was achieved. In the next step, we fitted all ODMR spectra with Equation (6.7). Figure 6.3.c indicates fitting results in which the x–axis represents the B–field strength. In the top panel, the FWHM of the left (right) Gaussian shows in red (Blue). According to this result, there is no significant difference between left and right Gaussian fits; however, around [115-140]

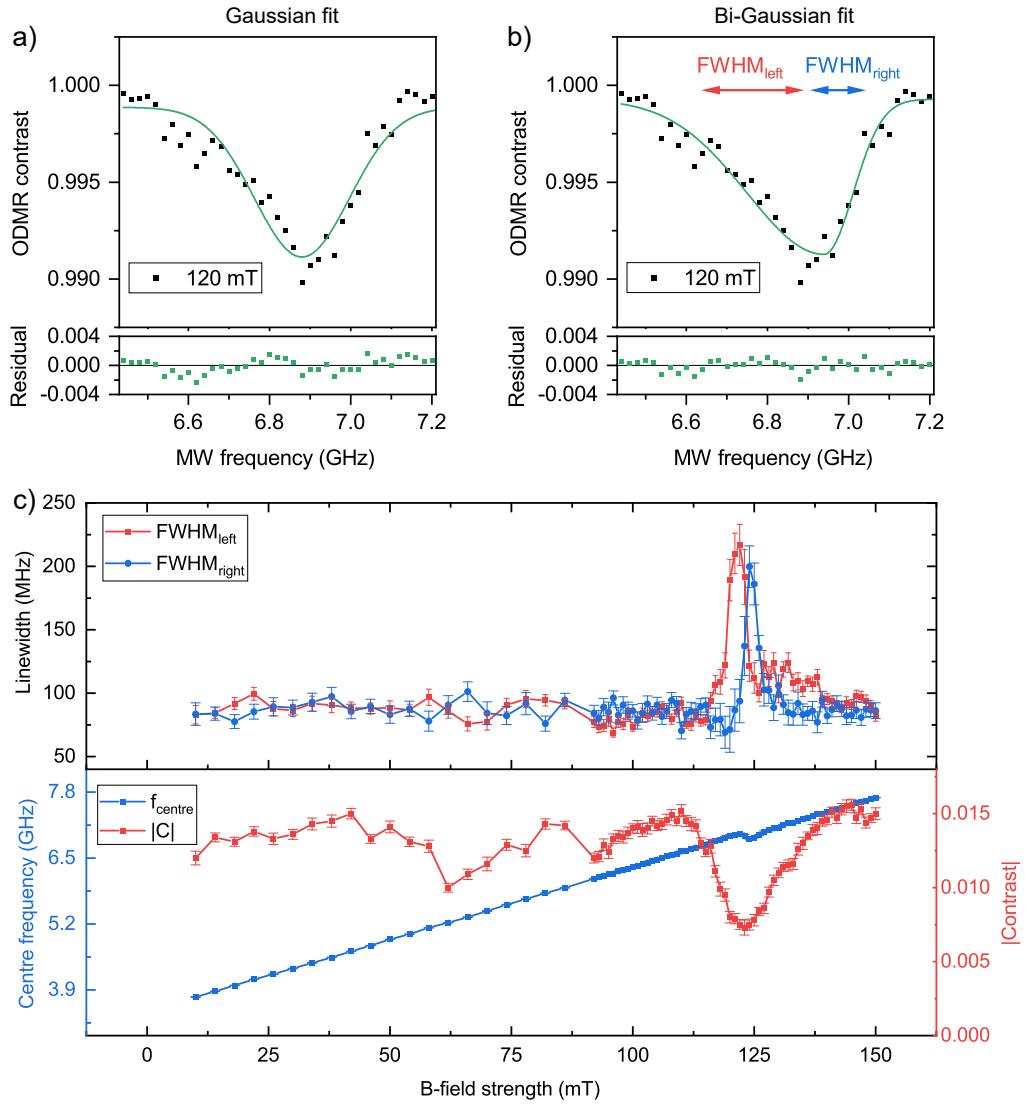

Figure 6.3: Bi–Gaussian fitting results of ODMR experiment over different B–field strength. a,b) Fitting results of ODMR spectrum at $B = 120\,\mathrm{mT}$ with Gaussian and Bi–Gaussian fits, respectively. c) Derived FWHMs for the left and the right side of the Gaussian fit is shown in the top panel in red and blue, respectively. The central frequency and the value of the dip of the ODMR contrast are shown in the bottom panel in blue and red, respectively.

mT, FWHM of both left and right–hand sides becomes asymmetric. According to Figure 6.2.c, this is around the magnetic field where the energies of $m_s = |0\rangle$ and $m_s = |-1\rangle$ are equal; this point is called ground state level anti–crossing (GSLAC). In real cases, there is a gap between two electronic states at the crossing point caused by tiny perturbations of the transverse magnetic field components and/or nuclear field [163]. Also, this energy gap is associated with those electron–nuclear levels ($|m_s, m_l\rangle$) that are avoided in mixing[1] [164]. The hybridisation of electron spin and nuclear spin near the GSLAC results in a further polarisation of the spin bath at

[1]Mixing of states at GSLAC will be discussed in subsection 6.3.3

the ground state. This possibly could explain why the linewidth of the ODMR dip around GSLAC turns to be asymmetric. The bottom panel in Figure 6.3.c shows the central frequency (blue) and contrast value (red) of ODMR dips. It is noted that the contrast near the GSLAC decreases. This can be explained by the level mixing mentioned earlier in the discussion.
To better understand the effect of magnetic fields on the spin system, it is mandatory to know the dynamics of magnetisation and relaxation mechanisms; these concepts are discussed in Appendix A and Appendix B, respectively.

6.3.3 Rabi Oscillations

Spin states can be manipulated coherently by applying the MW field at the resonant frequency. In the presence of the microwave excitation (spin manipulation), the Bloch equation can be written:

$$d\vec{S}/dt = \vec{\Omega} \times \vec{S} \tag{6.8}$$

where Rabi vector is defined as:

$$\mathbf{\Omega} = (\Omega_R \cos\varphi, \Omega_R \sin\varphi, \delta) \tag{6.9}$$

where $\Omega_R = g\mu_B B_{ac}/\hbar$ is the bare Rabi angular frequency, δ is the detuning from the resonance frequency, and φ is the phase (controlled by φ_{MW}). This precession is is inclined out of the x-y plane by an angle $\arctan(\delta/\Omega_S)$. Given that $d\vec{S}/dt$ and $\vec{\Omega}$ are orthogonal, it can be inferred that $\vec{S}$ rotates around the axis defined by $\vec{\Omega}$ with the angular frequency of $|\Omega|$. Figure 6.4.b depicts this oscillation. In this figure, the green (S) and red (Ω) arrows indicate Bloch and Rabi vectors, respectively.

In order to measure Rabi frequency, the defect system was studied under the Rabi sequence depicted in Figure 6.4.a. The ISC usually results in initialisation into $m_s = 0$ with imperfect fidelity. Next, the MW rotates the electron spin about z–axis. By varying the pulsewidth, τ (check Equation (C.3) and Equation (C.4)), the electron spin gets a different phase in the Bloch sphere. In the readout (when MW is switched off), the intensity recorded is proportional to the projection of the spin on the z–axis. In this stage, the electron spin is still precessing around z but we only measure the projection of spin along z–axis. The frequency of this oscillation is at Rabi frequency; the coherence time of this oscillation is called $T^*_{2,\mathrm{Rabi}}$, and it is often called inhomogeneous Rabi dephasing time. To distinguish this dephasing time from other dephasing times derived by other techniques, we use "Rabi" term in the subscript. Figure 6.4.c illustrates ODMR contrast for different B–field strengths as a function of pulsewidth for V_{MW} =750 mV (no tilt). This bias is applied to the

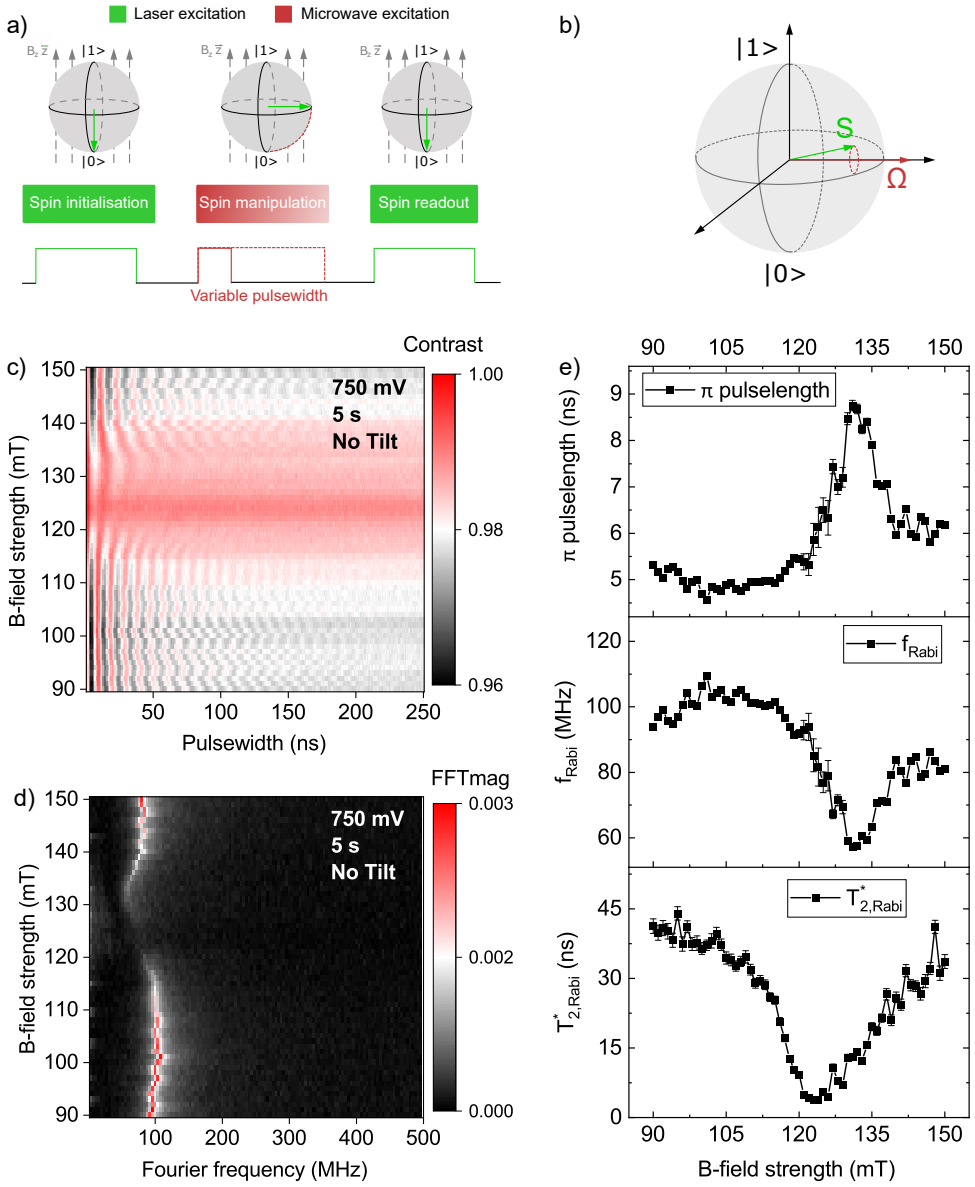

Figure 6.4: Rabi oscillation experiment. a) Rabi sequence used in this work. By varying pulsewidth, electron spin rotates on the Bloch sphere and get different phase. b) Bloch vector (green arrow, S) and Rabi vector (red arrow, Ω) evolution on the Bloch sphere. Under MW excitation, Bloch vector rotate around Rabi vector with Rabi angular frequency. c) Rabi oscillation at different B–field strengths for 750 mV MW amplitude. d) FFT of the time domain data. e) Inhomogeneous dephasing time, $T^*_{2,\mathrm{Rabi}}$, Rabi frequency, f_R $(= \Omega_R/(2\pi))$, and π pulse length derived from the fitting function mentioned in the main text.

CPW through amplifier. Rabi oscillation is observable in this 2D plot. By taking fast Fourier transform (FFT) from the time–domain data, the resonance frequency of Rabi oscillations can be identified. As it is shown in Figure 6.4.d, Rabi frequencies range is within $60\,\mathrm{MHz} < f_R < 110\,\mathrm{MHz}$. Proximity of the defect centre to the waveguide allows us to achieve high Rabi frequency ($\geq 100\,\mathrm{MHz}$). Rabi oscillation starts to disappear as the B–field strength reaches GSLAC point [100].

To unravel Rabi dephasing time, $T^*_{2,\mathrm{Rabi}}$, the following function was used for fitting the data in the time domain [165]:

$$Ae^{(-\alpha t)} + Be^{(-t/T^*_{2,Rabi})}\cos(2\pi f_R t + \phi) + Ee^{(-t/T^*_{2,Rabi})}\sin(2\pi f_R t + \phi) + D \quad (6.10)$$

Usually, the second and the last terms are enough for most Rabi data; however, if the data shows overall decay (the current case), the above function can fit the data better. The result of the fitting is shown in Figure 6.4.e. According to the result, coherence time is at its minimum around GSLAC. At GSLAC, $|m_s = -1, m_l\rangle$ and $|m_s = 0, m_l\rangle$ mix with each other in which $-3 \leq m_l \leq 3$. Mixing of states happens only when the sum of the electron and nuclear angular momentum projection for the mixing partners must be equal; i.e. $(m_s + m_l)_s = (m_s + m_l)_f$ where s and f account for start and final states [166]. Also, the energy must be conserved, and at GSLAC, there are close–by energy states for the electron to flip into. As a result, electrons have more pathways to decay into, which is probably why the coherence time is reduced at GSLAC. Finally, the derived π pulse length values are used in the Ramsey and spin–echo experiments. Half of this value is needed to rotate the electron spin on the Bloch sphere by 90°.

The fitting of the Rabi data sometimes uncovers more underlying physics. Rabi data and its fitting result at $\mathbf{B} = 150\,\mathrm{mT}$ is shown as an example in Figure 6.5.a. Based on the fitting results, f_{Rabi} and $T^*_{2,\mathrm{Rabi}}$ are around 81 MHz and 33.6 ns; however, Rabi oscillations persist at longer times than would be expected from fits to data at shorter times; this suggests that single damped oscillation is not enough. Therefore, we extend Equation (6.10) to support two Rabi frequencies ($f_{1,\mathrm{Rabi}}$ and $f_{2,\mathrm{Rabi}}$) and Rabi coherence times ($T^*_{21,\mathrm{Rabi}}$ and $T^*_{22,\mathrm{Rabi}}$). It is evident from the fitting results depicted in Figure 6.5.b that the data is appropriately fitted. According to the results, Rabi frequencies and Rabi coherence times are around (79.6 and 87.5) MHz and (81.4 and 8.7) ns, respectively. Interestingly, the Rabi frequency 79.6 MHz has one order of magnitude higher coherence time which suggests it can be the main transition; also, the other transition has a higher Rabi frequency (8 MHz) which is four times higher than quadrupole interaction in hBN [111]. There are two possible explanations for this:

- when $\delta = 0$ (see Equation (C.5)), only principal (carrier) transition happens, i.e. $|m_s = 0, I_z\rangle \rightarrow |m_s = +1, I_z\rangle$, where ${I_z}^2$ is the projection of a nuclear spin along the external magnetic field [167]; however when there is a slight detuning in the driving MW field, this would result in sideband resonant transitions with a different amplitude (modified Rabi strength). The red (lower energy) and blue (higher energy) dashed arrows indicate these possible Zeeman transitions

[2] Often it describes as nuclear spin polarisation.

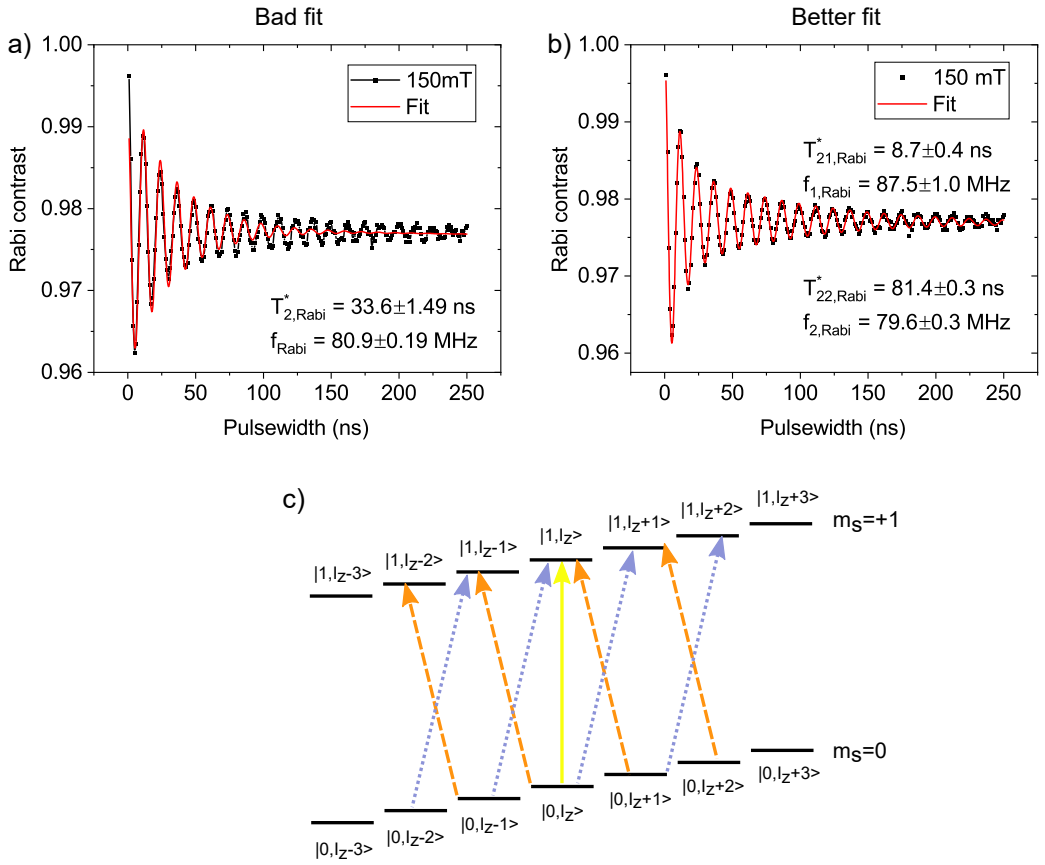

Figure 6.5: Explanation of failed Rabi fitting using ladder diagram. a) Example of Rabi fitting for data taken at $\mathbf{B} = 150\,\mathrm{mT}$. Fitting failed to longer pulsewidth. b) The same data presented in (a) but with a better fitting. c) Ladder diagram of the electron and nuclear states showing the principal (carrier) transition (yellow arrow) as well as sideband transitions (Blue and red).

in Figure 6.5.c. This scenario was observed experimentally in trapped ion and QD systems [168–170]. It is worth highlighting that optical excitation is another important factor here. As we are using a non–resonant green laser, it would be safe to say that this excitation mechanism, alongside MW detuned frequency, can drive the sideband transitions. Further experiment is needed to find answers.

- for an ensemble with variation in transition energies with a range of detuning, detuning the signal has the form

$$P(t) = \int P_{Rabi}(\delta, t)p(\delta)d\delta \tag{6.11}$$

where $p(\delta)$ is the probability distribution of detuning and $P_{Rabi}(\delta, t)$ is the Rabi oscillation signal of a single defect detuned from the drive. At low times, the frequency bandwidth is large, and many defects contribute, leading to fast decay. At longer times, the pulse has narrow bandwidth (Fourier transform theory), and a sub-set of defects contributes, leading to a long decay time.

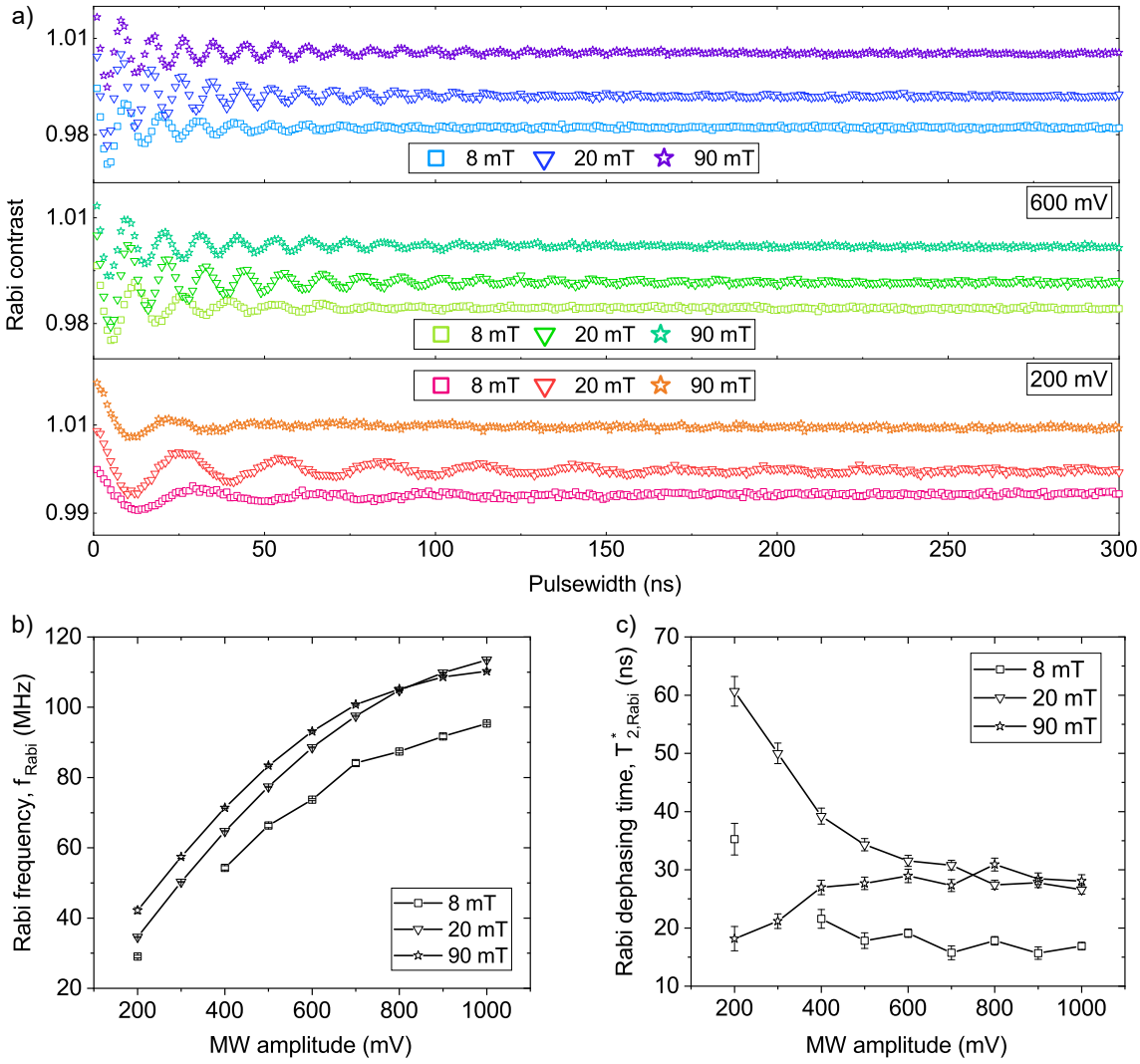

Figure 6.6: Rabi oscillations at different MW amplitude for three B–field strengths. a) Rabi contrast examples for three different MW amplitude, 200 mV (lower section), 600 mV (middle section), and 1000 mV (upper section in the stack). Each section consists of three plots in which the lower, middle and upper plots show Rabi oscillation for 8 mT (hollow square), 20 mT (hollow upside–down triangle), and 90 mT (hollow star), respectively. For better visualisation, all graphs are offset vertically. b) Rabi frequency as a function of MW source power for different B–field strengths. Each set of data shows linear dependence between Rabi frequency and source power. c) Coherence (inhomogeneous dephasing) time, $T^*_{2,\mathrm{Rabi}}$, versus MW amplitude.

Next, the effect of MW amplitude (V_{MW}) at different B–field strengths on Rabi frequency and its coherence time was studied. Figure 6.6.a shows a stack graph consisting of three sections; in each section, the top (hollow star), middle (hollow upside–down triangle), and bottom (hollow square) symbolised lines represent 90 mT, 20 mT, and 8 mT, respectively. The experimental data for 1000 mV, 600 mV, and 200 mV are from top to bottom. In order to fit the data, Equation (6.10) was used, and the results were depicted in Figure 6.6.b and Figure 6.6.c. Rabi frequency as a function of MW source power shows a linear trend as shown in [100]; however, it

deviates from the linear relation at higher power. Possibly the heating of the CPW that change its resistance is the reason of this behaviour and saturation of amplifier. (Another explanation could be due to anharmonicity of the confinement potential of the defect centre [171, 172].)

Rabi coherence time (i.e. inhomogeneous dephasing time) is depicted in Figure 6.6.c. There are two different trends; 1) when B–field strength is not close to GSLAC, i.e. 8 and 20 mT, by increasing MW amplitude, $T^*_{2,\mathrm{Rabi}}$ decreases. 2) when B–field strength is close to the GSLAC point, increasing MW amplitude will result in higher $T^*_{2,\mathrm{Rabi}}$. Based on the last two figures discussed here, the highest Rabi oscillation achieved was 115 MHz ($T^*_{2,\mathrm{Rabi}} = 28$ ns), and the highest inhomogeneous dephasing time was 60 ns ($f_R = 30$ MHz). In order to quantify spin–qubit controllability, the Rabi oscillation quality factor can be defined as $Q_R = T^*_{2,\mathrm{Rabi}}/T_\pi$, where T_π donates the spin–flip rotation time and can be simplified to $T_\pi = 1/2f_R$ [172, 173]. The parameter characterises the coherence of the rotation, which measures numbers of π rotations before Rabi oscillation visibility falls below $1/e$ of its initial value [174]. Rabi quality factor is extracted and plotted in Figure 6.7 for three different B–field strengths. At low Rabi frequency, Q_R is minimum, and that is due to higher $T^*_{2,\mathrm{Rabi}}$ (this cannot be applied to 90 mT case). By increasing f_R, the quality factor increases in an almost linear trend.

6.3.4 T_1 relaxometry

After electron spins are initialised (see subsection 3.5.4), the longitudinal magnetisation vector decays to the thermal equilibrium condition; the time characteristic of this decay is called longitudinal spin relaxation time or T_1. T_1 sets a limit on

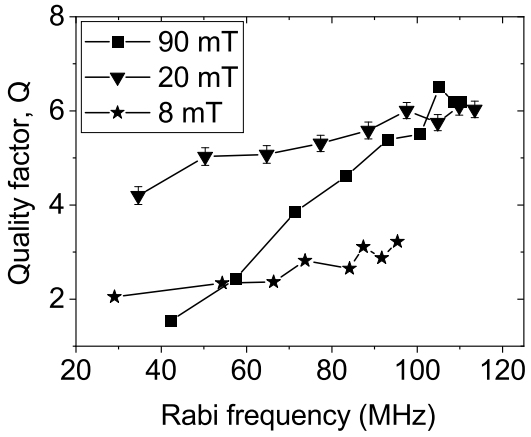

Figure 6.7: Rabi oscillation quality factor. a) Rabi quality factor as a function of Rabi frequency. Increasing Rabi frequency increases the quality factor. b) Quality factor versus temperature. Here, we compared the maximum quality factor in this work with different published works.

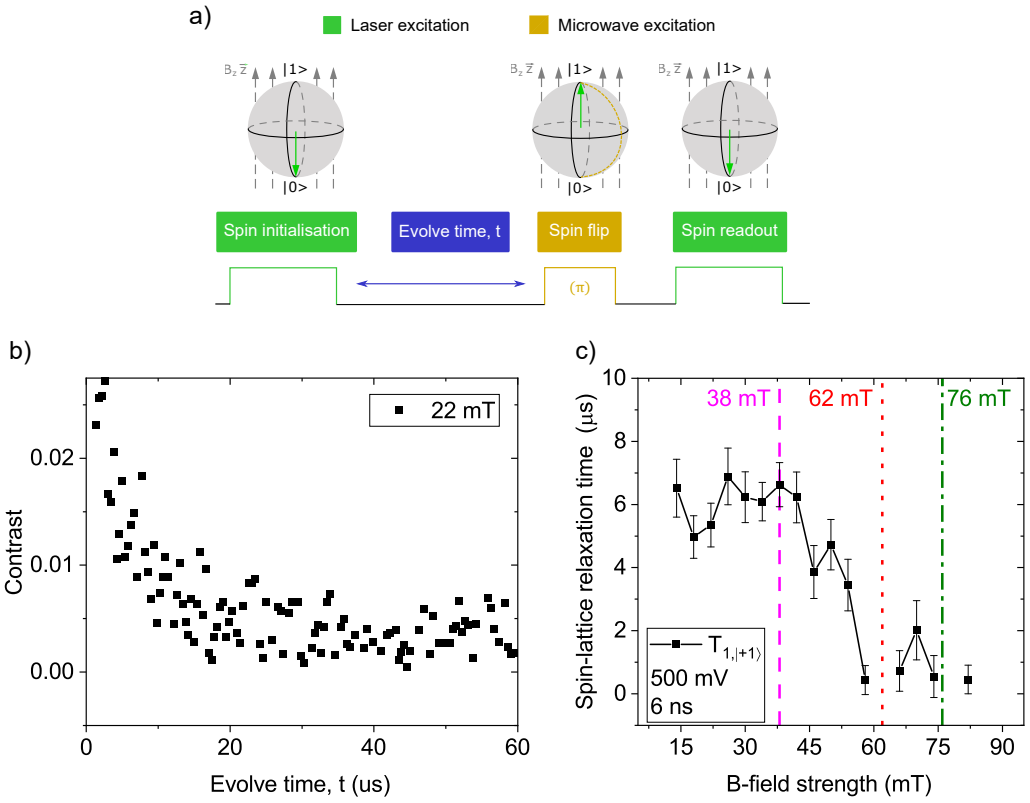

Figure 6.8: Spin relaxation time measurement. a) Pulse sequence used in this work to measure T_1 relaxation time. b) The difference of contrasts measured with and without MW π–pulse as a function of B–field strength. c) Fitting results of the experimental data in (b).

spin coherence times and is important to know. The sequence shown in Figure 6.8.a was used to determine the spin relaxation time with a standard π–pulse sequence. The microwave π–pulse shuffles the population to the $|1\rangle$ state by addressing the $|0\rangle \rightarrow |1\rangle$ transition, and finally, the population decay of the $|1\rangle$ is measured. In order to calculate T_1, we first calculate contrast for two different experiments, one with MW excitation and one without. Then the difference between the two contrast was calculated [175]. This result for B = 22 mT is shown in Figure 6.8.b. In order to fit this result, the below formula was used:

$$Ae^{-t/T_1} + B \tag{6.12}$$

The fitting result is shown in Figure 6.8.c; to analyse the evolution of $T_{1,|1\rangle}$ over different external magnetic fields, we break it into two distinct regions:

- **B $\leqslant$ 40 mT:** The $T_{1,|1\rangle}$ is around 6 µs, where $|1\rangle$ in the subscript indicates the electron spin state. In this B–field range, the spin relaxation time does not exhibit a strong dependency on the external magnetic field; the same behaviour was seen in [43] where such a robustness of spin relaxation time over the external magnetic field suggests attributed to the dominant factor of

the local magnetic field.

- **B > 40 mT:** $T_{1,|1\rangle}$ relaxation time starts to decrease. As addressed in [100], the Zeeman splitting of the spin–1/2 system is resonant with the $m_s = |0\rangle \leftrightarrow |-1\rangle$ transitions in the excited and ground state of V_B^- at a magnetic field of ~ 38 mT and ~ 62 mT, respectively. These transitions may be responsible for the decrement in spin relaxation time. These transitions are shown with pink–dashed and red–dotted lines in Figure 6.8.c, respectively. Coupling the boron vacancies to neighbouring paramagnetic defects of another species or charge state can be the origin of this behaviour [100, 176, 177]. Haykal *et al.* reported the same behaviour at 62 mT and attributed it to the cross–relaxation induced by electron dipole–dipole interaction. They claimed that the dip in the spin relaxation time is a signature of dark electron spin impurities with S = 1/2 in the close vicinity of the defect [175].

Another mechanism than can affect T_1 is the phonon process. Temperature dependence is not studied in this work, so we are not in a position to say much about phonons other than to discuss prior articles. Electron–populated vibronic states can be effectively a relaxation channel if their energies become comparable with electron spin Larmor frequency [43]. Temperature–dependent T_1 relaxation study on this defect centre (different sample, though) suggested that T_1 is temperature–independent at Temp$<$ 20 K, with the most extended measured value of $T_1 = 12.5$ ms. At temperature Temp$>$ 20 K, T_1 decreases with the slope of $\text{Temp}^{-5/2}$; this value rules out the single–phonon scattering process ($\propto \text{Temp}^{-1}$) and Orbach-type processes[3] ($\propto (e^{\frac{\hbar\omega_{loc}}{k_B Temp}} - 1)^{-1}$). The remaining possible scenario involves a two–phonon process (including direct transition, stokes and anti–stokes, and spontaneous emission), but the expected values for non–cubic 2D and 3D are Temp^{-3} and Temp^{-5}, respectively[4]; therefore, we conclude that the phonon process plays a role in limiting T_1, but the origin of such a process is unknown.

A comparison between reported T_1 values for V_B^- at room temperature is given in Table 6.2. According to this table, ions with larger radius sizes are likelier to create an ensemble of defects with shorter spin relaxation times [178]. In contrast, the best results are achieved for light particles (Neutron or Helium) at high doses, which also results in more damage to the crystal. It is worth highlighting that a 532 nm laser was used in all these works. The off–resonant optical excitation not only introduces emission or scattering phonons in the crystal through the spin–orbit interaction but also detunes λ_{exc} from λ_{res} by $\delta\lambda$; this detuning degrades the fidelity of the state and ultimately reduces the robustness of both nuclear spins and electron spins [179].

[3] It results from quasi–localised phonon modes; $\hbar\omega_{loc}$ characteristic energy

[4] Diamond and hBN are examples of 3D and 2D non–cubic structures.

Table 6.2: Reported T_1 values for V_B^- at $T = 300\,K$ ($\lambda_{exc} = 532\,nm$)

Generation method	Dose/Fluence (n/cm^2)	Energy (keV)	T_1 (µs)	λ_{em} (nm)	Ref.
Neutron	2.3×10^{18}		18, 25[1]	850	[43, 96]
Neutron (^{11}B)	2.6×10^{17}		16	800	[175]
Neutron (^{10}B)	2.6×10^{16}		16	800	[175]
He^+	5×10^{13}	2.5	17	810	[114]
He^+	1×10^{14}	30	17	800	[178]
Nitrogen	$[0.01 - 1] \times 10^{15}$	30	[14 - 5.5]	810	[178]
Argon	1×10^{14}	30	6	805	[178]
Carbon	1×10^{14}	30	11.5	820	[178]
Carbon	1×10^{14}	10	6	860	This work

[1] Hole–burning technique

Despite the measured T_1 in this work which is on the low end of reported values, it should be noted that the sample stage was not perfectly aligned at the time of the experiment. Sample and B–field angle misalignment would affect hyperfine coupling strength, which is the reason for our experiment's lower value of T_1. In [44], the spin relaxation time is reported to be around 12 µs.

To improve T_1, one possible challenge to overcome is to stabilise the charge state on–demand during qubit operation[5]. This is very important, especially in 2D material, which generally suffers from surface charge traps. Charge state stabilisation is about stopping the charge jumping on/off the defect which losing memory of its spin. Therefore, the defect is less prone to spin environment dephasing. A well–stabilised charge state is less likely to have an additional T_1 relaxation channel through random charge state switching [179].

6.3.5 Electron–nuclear interaction

As discussed, the electron spin of the V_B^- defect is a spin–triplet. These spin–triplets interact with their surrounding in the hBN lattice via spatially–dependent dipole interaction; in this sample, the nuclear spin bath consists of ^{14}N (99.6%), ^{11}B (80.1%) and ^{10}B (19.9%) and ^{13}C atoms [43, 100]. It is essential to know that the envelope of the electron wavefunction, **S**, interacts with the nuclear spin **I**. This interaction consists of two contributions [180]:

- Contact hyperfine (or isotropic Fermi): This represents the s–orbital contribution of the electron spin density at the nucleus.
- Dipole–dipole (or anisotropic): It represents anisotropy in hyperfine, caused by p, d, f or higher orbital contributions of the electron spin density at the

[5] ensemble

Table 6.3: Isotope–dependant parameters of spin Hamiltonian

Isotope	nuclear spin (l)	$A_{xx,yy}(A_\perp)^1$	$A_{zz}(A_\parallel)^1$	P^1	Ref.
^{14}N	1	A_{GS} = 45–47	88, 4.5[3]	0.2	[100, 175, 181, 182]
^{11}B	3/2		– 4.6[2]	3.004	[175, 182]
^{10}B	3		-1.5[2]	6.260	[175, 182]
^{13}C	1/2			–	

[1] MHz. [2] six second–neighbours. [3] six equivalent third–neighbours.

nucleus.

Apart from the type of the defect system, these two terms are of significant importance when it comes to the decoherence of the electron spin because electron–nuclear interaction results in nuclear spin flip–flops which ultimately affect the electron spin coherence time.

Experimental values for the hyperfine interaction, **A**, for different isotopes are given in Table 6.3. The hyperfine tensor is axially symmetric due to the trigonal symmetry of the V_B^- defect (ground state) and can be expressed by [111]:

$$\mathbf{A} = \begin{pmatrix} A_{xx} & 0 & 0 \\ 0 & A_{yy} & 0 \\ 0 & 0 & A_{zz} \end{pmatrix} \tag{6.13}$$

where $A_{xx,yy}$ and A_{zz} are the perpendicular and parallel components of the hyperfine tensor, respectively. This explanation is valid for isotropic hyperfine tensors; for spin–1/2 ^{13}C, it is reasonable to consider an anisotropic hyperfine tensor in which the non-diagonal terms in the above tensor become nonzero due to dipolar interaction [183]. Anisotropic hyperfine tensor becomes more important when the magnetic field direction, **B**, is no longer parallel with the V_B^- defect's c–axis.

Each nucleus' spin effect can be considered as a magnetic field vector; therefore, an ensemble of nuclear spins acts as an effective magnetic vector. If this field has a mean polarisation, it is known as the Overhauser field. For V_B^- with three ^{14}N (nuclear spin–1) as the nearest neighbour nuclei, a total nuclear spin of $I = 3$ and an Overhauser field of 141 MHz is suggested [100]. In thermal equilibrium, the electron and nuclear spin polarisation is given by Boltzmann factor $\mathbb{B} = \frac{\hbar\gamma B}{k_B T}$; this factor is approximately three orders of magnitude greater for electron spin than nuclear spin (check Figure B.1 and [184]). The Overhauser field alters the electron spin polarisation, affecting nuclear spins (for example, through the spin flip–flop process). Besides, electron spins can precess in the B–field caused by the nuclei and vice versa. These ultimately degrades the coherence time of the electron spin. Ensemble of V_B^- is a complex system.

6.3.6 Ramsey interferometry

Random and (quasi–) static distribution of nuclear spin states result in inhomogeneous Ramsey dephasing time, i.e. $T^*_{2,Ramsey}$. In order to measure this time characteristic, Ramsey interferometry can be studied. Standard Ramsey pulse sequence is shown in Figure 6.9.a. In the defect rotating frame, MW–unperturbed but optically–initialised electron spin (here $|0\rangle$) is considered in $-z$–direction and $|+1\rangle$ in the north pole of the Bloch sphere; by applying a proper $\pi/2$ pulse, electron spin rotates and is aligned in the x–y plane. During "evolve time, t", electron spin dephase in the x–y plane without any external optical or MW perturbations. Then,

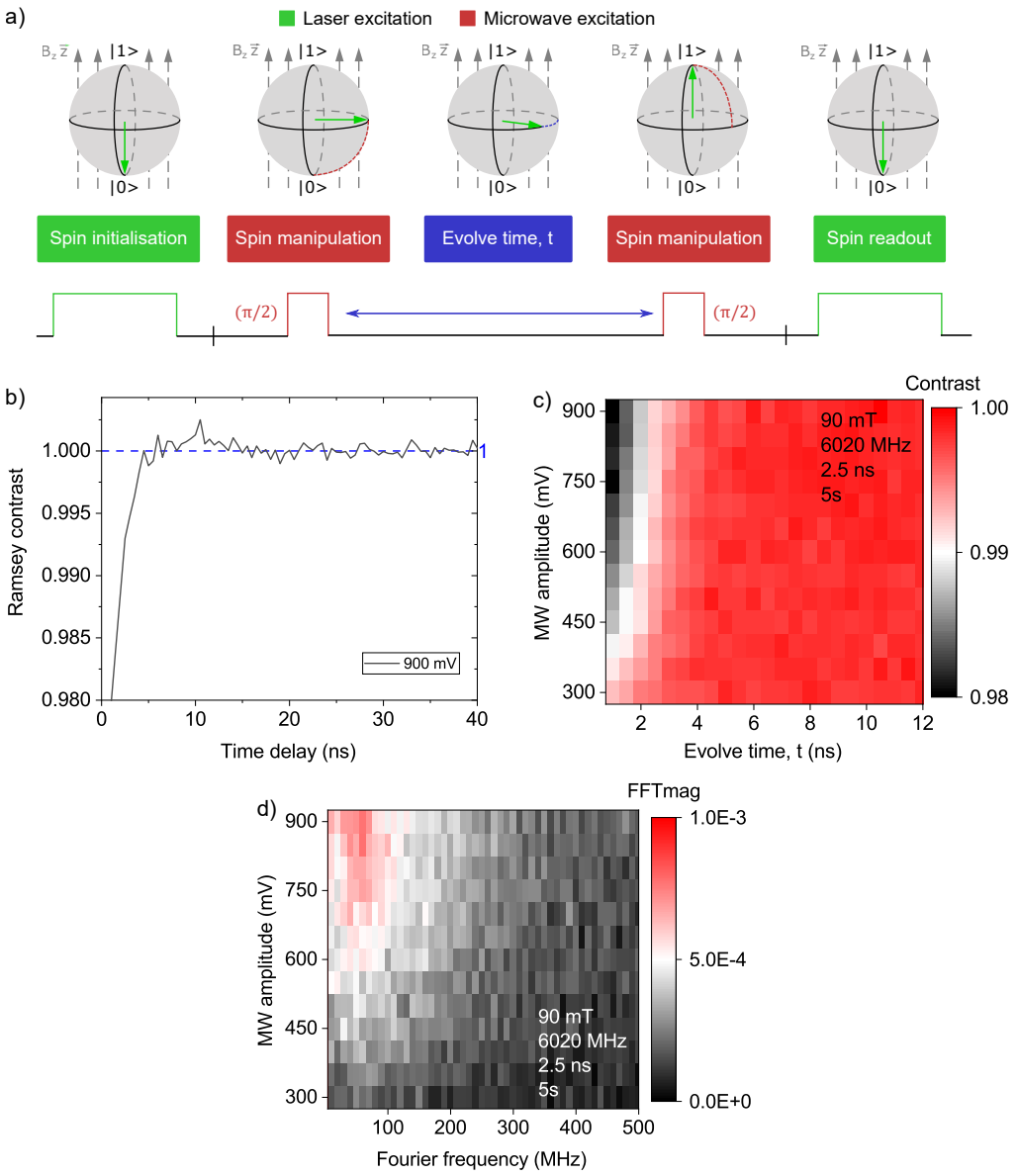

Figure 6.9: Ramsey interferometry. a) Ramsey sequence used in this work. b) Ramsey contrast for 900 mV acrshortMW amplitude versus time delay. c) Ramsey contrast for different MW amplitude versus time delay. d) FFT of the time domain data.

electron spin is rotated back to the z–axis by applying a second $\pi/2$ pulse. Finally, electron spin projections onto the z–axis is being readout by an optical pulse.

When the MW pulse is not quite $\pi/2$ pulse, what happens? This situation was investigated in Figure 6.9.c and Figure 6.9.d, where the former shows an example of Ramsey contrast at 900 mV, and the latter indicates a 2D scan of the contrast derived from Ramsey interferometry at 90 mT. From Figure 6.4.e, the π-pulsewidth at 90 mT was calculated at around 5.3 ns for 750 mV. Therefore, to apply a $\pi/2$ pulse, the system requires a pulsewidth of around 2.65 ns. In Figure 6.9.b and Figure 6.9.c, the pulsewidth was fixed at 2.5 ns, and the MW amplitude was swept as shown in the y–axes. The x-axis in this figure shows the "evolve time, t". It is clear that as MW amplitude increases, $T^*_{2,Ramsey}$ increases too. The following function was used to fit the data in the time domain [185]:

$$B + e^{(-t/T^*_{2,Ramsey})^m} \sum_{i=1} (A_i \cos(2\pi f_i + \phi_i)) \tag{6.14}$$

Fitting data showed a short Ramsey dephasing time ($T^*_{2,Ramsey} < 3$ ns) for imperfect $\pi/2$ MW pulses.

6.3.7 Spin echo interferometry

Spin–echo was studied to suppress the nuclear spin bath's static and slow fluctuations over the pulse sequence's duration by refocusing electron spins [186, 187]. Spin–echo sequence used in this work is depicted in Figure 6.10. After electron spins are initialised optically in the $|0\rangle$ state, a proper $\pi/2$ pulse is applied to the system to rotate electron spins by 90°. Similar to "evolve time, t" in the Ramsey interferometry, during "evolve time, t_1", electron spins dephased in the x–y plane without any external optical or MW perturbations. In the next step, electron spins are rotated by a π pulse; in this step, the fast dephasing electron spins before the π pulse become out–of–phase exactly 180° after the π pulse. Under this condition, all electron spins acquired same magnitude but opposite sign phase after "evolve time,

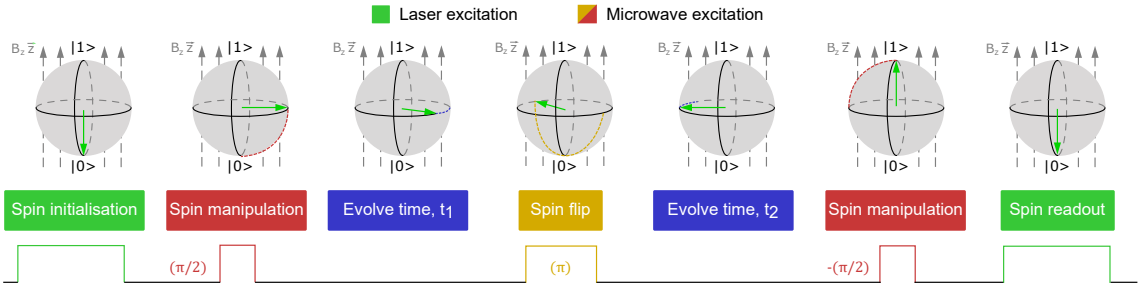

Figure 6.10: Spin echo pulse sequence. The 2nd $\pi/2$ pulse was applied with a 180° phase difference to the 1st $\pi/2$ pulse to increase contrast.

$t_2 = t_1$". Next, by applying the second $\pi/2$ pulse, electron spins rotated back to the z–axis. Finally, electron spin projections onto the z–axis are readout by an optical pulse.

To ensure selective addressing, we make sure that $f_R \ll$ Zeeman splitting, then two scenarios are studied:

- $f_R < A_\perp$: Rabi amplitude is less than the hyperfine coupling between nuclei states in this regime. Figure 6.11.a shows the spin echo result for this regime in which the x–axis is the total time delay and the y–axis is the B–field strength. The average magnetic–field dependent pulsewidth to rotate the electron spin for 180° is calculated to be around 25 ns. As is shown in the FFT result in Figure 6.11.b, the spin echo data does not show any frequency component. In order to fit the time domain data, the below function was used [188]:

$$C + Ae^{-(t/T_{2,echo})^n} \tag{6.15}$$

  in which $T_{2,echo}$ and n are homogeneous dephasing time and exponent factor, respectively. Relevant results are shown in Figure 6.12.a. According to the result, right before and after the GSLAC point (124 mT), the coherence time slightly increases (for example, 30 ns at 116 mT). Around GSLAC, the relevant results are less reliable, as a high error margin evidences it.
- $f_R > A_\perp$: In this case, electron spin can couple to nuclear spin and this coupling results in periodic collapses and revivals in the contrast (or coherence). This pattern can be seen in the time–domain data shown in Figure 6.11.c. To find the frequency of these collapses and revivals, FFT is taken from the time–domain data, which is depicted in Figure 6.11.d respectively. According to the FFT result, these oscillations compromise two frequency components, approximately at 45 and 90 MHz. One possible way to explain these results is electron spins couple to nearby nuclei by $1 \times HFI$ and $2 \times HFI$ (1^{st} and 2^{nd} order hyperfine, respectively). It is worth reminding that the A_{zz} component of the hyperfine for ^{14}N is also 88 MHz (see Table 6.3). However, it is less likely that this component plays any role in the spin echo experiment; After rotation, electron spins, due to the 1^{st} $\pi/2$ pulse, will interact with $A_{xx,yy}$ components; therefore, we assign the $f_{echo(2)}$ appearance to the 2^{nd} order hyperfine term.

  Next, we used the following formula to fit the time–domain data to extract the spin–echo coherence time [188]:

$$C + \sum_{i=1} e^{-(t/T_{2,echo(i)})^{n_i}} (A_i + B_i cos(2\pi f_{echo(i)} t + \phi_i)^{m_i}) \tag{6.16}$$

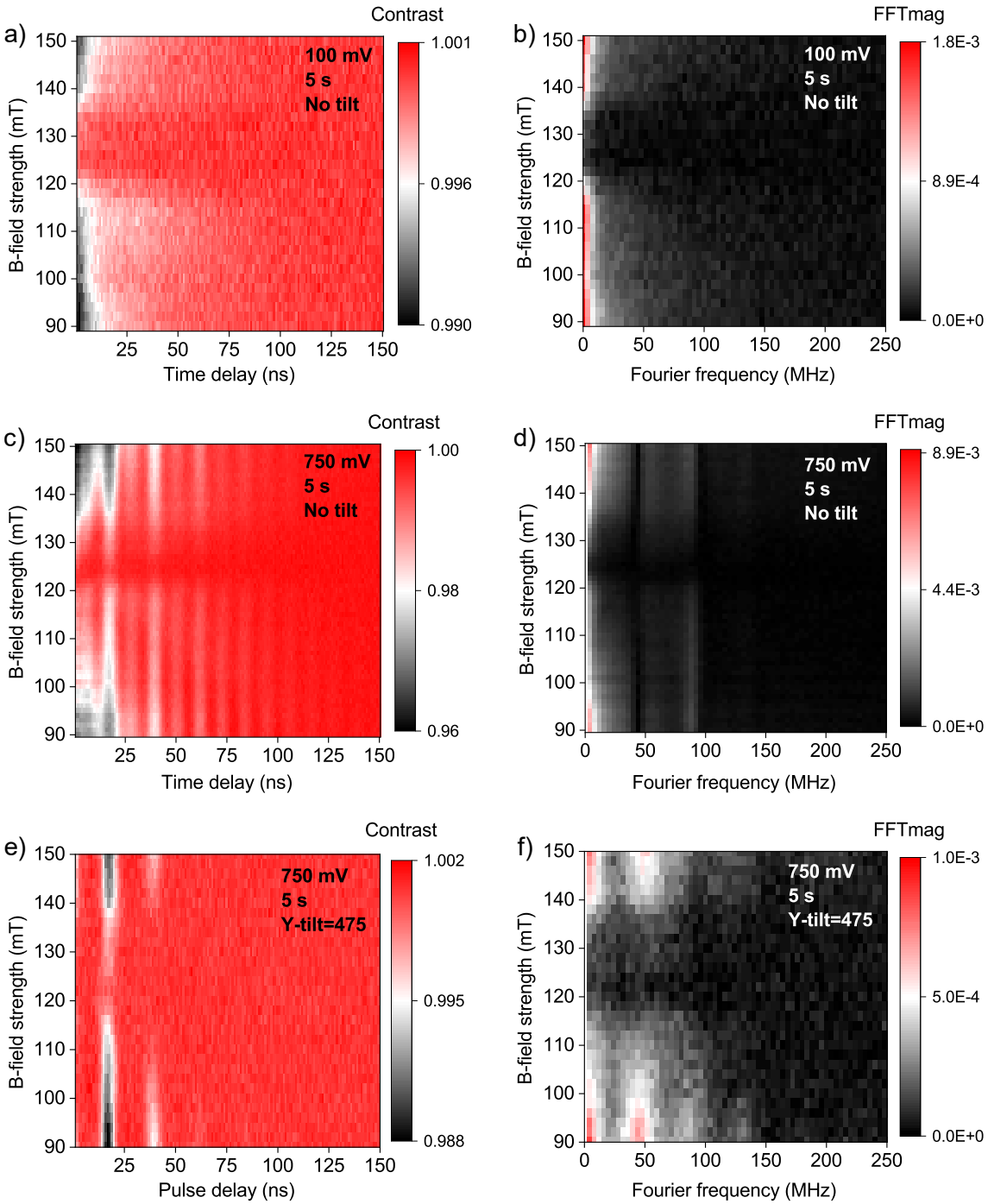

Figure 6.11: Spin echo interferometry. Spin echo contrast as a function of B–field strength and time delay for a) 100 mV and b) 750 mV. FFT of the time domain data for c) 100 mV and d) 750 mV. e) Spin echo contrast for 750 mV but tilted f) FFT of the time domain data shown in e.

where m is the empirical fitting parameter (or cosine factor). In this formula, we considered the initial guess for $f_{echo(1)}$ and $f_{echo(2)}$ around 45 MHz and 90 MHz, respectively. Figure 6.12.b illustrates the fitting results. Blue and red lines show spin–echo coherence (or homogeneous dephasing) times and derived frequencies, respectively. Those electron

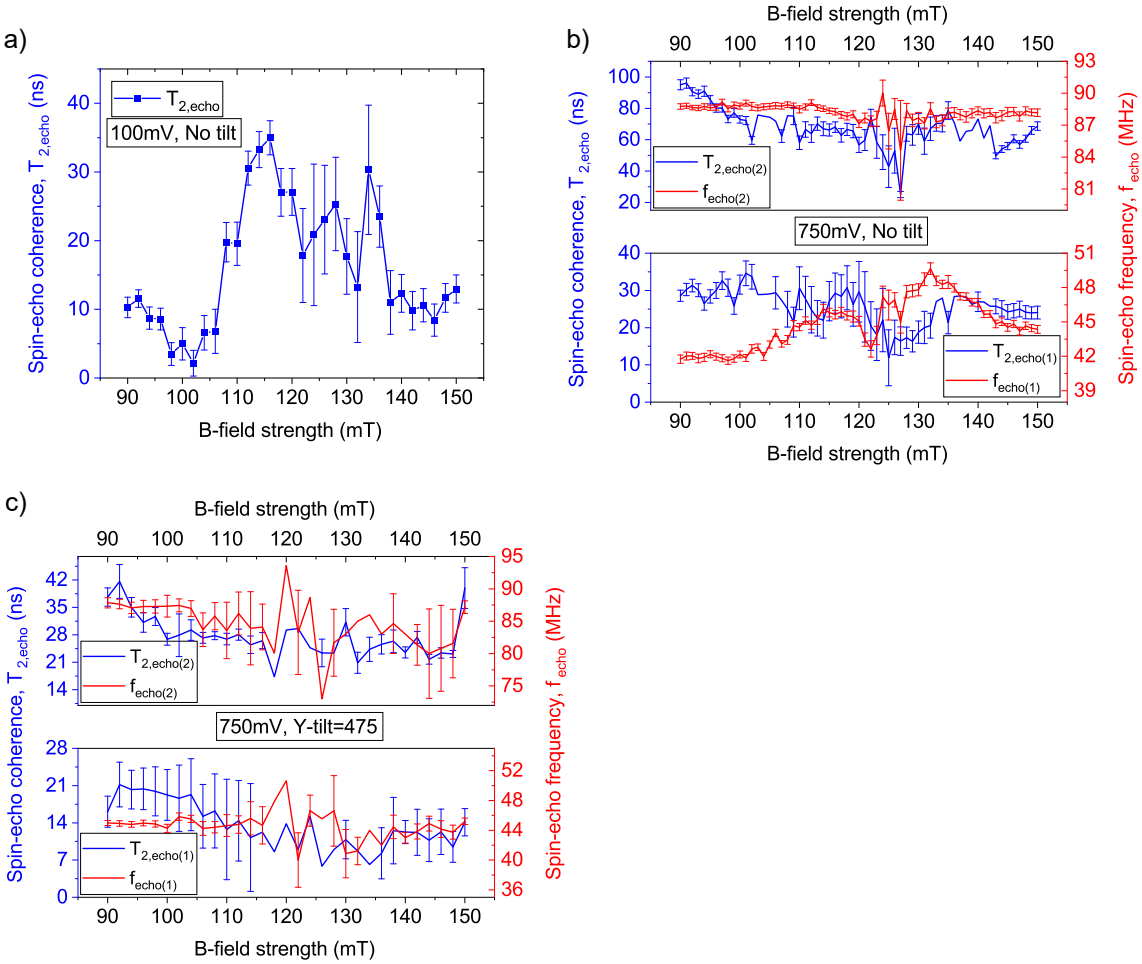

Figure 6.12: Spin echo fitting results. a) Coherence versus B–field strength for 100 mV. b) Coherence (blue lines) and frequency (red lines) for 750 mV. The lower and upper windows show results for the 1st and 2nd order hyperfine terms. c) Similar to the previous plot but for the tilted case.

spins couple to the 2nd order hyperfine term and decoheres differently ($\overline{X}_{f_{echo(1)}} = 44.8 \pm 0.4$ MHz, $\overline{X}_{T_{2,echo(1)}} = 25.7 \pm 3.1$ ns) than the 1st order hyperfine term ($\overline{X}_{f_{echo(2)}} = 88.2 \pm 0.4$ MHz, $\overline{X}_{T_{2,echo(2)}} = 67.6 \pm 3.6$ ns). Around the GSLAC point, the coherence of the signal comes mainly from the 2nd order hyperfine term. Also, the frequency of this term shows a more stable trend over the B–field strength sweep. It is worth to highlight that in the NV defect system, these trends are ascribed to the incoherent Larmor precession of the carbon spins [189].

To better grasp the collapse–revival patterns, the system was studied in the tilted condition. Figure 6.11.e and Figure 6.11.f illustrate the time domain and its FFT in the frequency domain, respectively. Just by quick comparison between this condition and the no tilt condition depicted in Figure 6.11.e, it can be easily said that overall oscillation, and contrast, decreased. More information can be derived

Table 6.4: Comparison between spin echo parameters mean values ($\overline{X}$) for no–tilt and tilted conditions

Parameter	no–tilt	tilted
$T_{2,echo(1)}$ (ns)	25.7 ± 3.1	13.4 ± 3.6
$T_{2,echo(2)}$ (ns)	67.6 ± 3.6	27.7 ± 2.0
$f_{echo(1)}$ (MHz)	44.8 ± 0.4	44.6 ± 1.1
$f_{echo(2)}$ (MHz)	88.2 ± 0.4	84.5 ± 2.2

by analysing the relevant results shown in Figure 6.12.c. The extracted mean values for all four parameters ($\overline{X}^t_{f_{echo(1)}} = 44.6 \pm 1.1\,\text{MHz}$, $\overline{X}^t_{T_{2,echo(1)}} = 13.4 \pm 3.6\,\text{ns}$, $\overline{X}^t_{f_{echo(2)}} = 84.5 \pm 2.2\,\text{MHz}$, $\overline{X}^t_{T_{2,echo(2)}} = 27.7 \pm 2.0\,\text{ns}$) suggest that frequency components remained untouched in comparison to the non–tilt condition. In contrast, the coherence components of the 1st and 2nd terms were reduced by 1.9 and 2.7, respectively (superscript t is donated for *tilted* to differentiate between two conditions). A summary of parameters compared between both conditions is shown in Table 6.4.

6.4 Discussion

In this chapter, we explored the spin properties of the V_B^- in hBN by studying Rabi, Ramsey, and spin echo experiments. These fundamental techniques are building blocks and necessary to study more complicated techniques. These studies helped us understand the defect system better. In this work, we studied a carbon–irradiated sample. We implemented the Rabi oscillation experiment on a wide range of static magnetic fields and showed that the $T^*_{2,\text{Rabi}}$ is at its minimum around GSLAC. B–field sweep analysis showed that it is possible to achieve higher spin dephasing time at 90 mT. The T_1 relaxometry study showed that the spin relaxation time we derived from this sample is shorter than other works. We conclude that smaller ions is more beneficial for achieving higher spin relaxation time. Finally, we demonstrated that the coherence time of the electron spin could be extended to 100 ns (Figure 6.12) at 90 mT.

CHAPTER 7

Conclusions and future research paths

In what follows, I summarised the main results of each chapter, with a discussion about possible future research directions.

7.1 Dielectric bullseye Bragg grating cavity

In Chapter 4, I:

- presented step by step the method I used to design a bullseye Bragg grating to enhance the collection efficiency and increase the Purcell factor. This method allows me to achieve the highest reported collection efficiency and Purcell factor in the visible wavelength based on the dielectric–based bullseye Bragg grating structure.

- explored the coupling condition between the dipole and the cavity in my design and showed that the collection efficiency remains high because of exploiting a gold layer as a reflector layer.

- calculated the coupling efficiency between the dipole and the cavity based on Equation (4.4). According to this study, I can achieve around 15000 and 6900 times increment in the bullseye structure compared to a reference structure for on– and off–resonant excitations, respectively.

- applied apodization to the grating in the bullseye structure to achieve higher collection efficiency into a fibre. Based on my results, collection efficiency increases before being saturated at higher rings.

One of the significant challenges in the simulation was the simulation resources. As the number of rings increases, the simulation time and space required for each study grow significantly. To solve this, automating part of the simulation is one of the methods that can be considered. Also, it might be possible to collapse the full 3D simulation into a 2D simulation and use effective index mediums or coupled mode theory to take into account the effect of the third dimension [190].

In addition, due to the higher refractive index of TiO_2 compared to SiO_2 and air, a fraction of emitted light from the dipole, after being influenced by the cavity, is transmitted inside the TiO_2 slab (after the last ring). In order to minimise this, it is possible to introduce a second bullseye grating structure at the top of SiO_2 (the

boundary between SiO_2 and TiO_2) [191]. Misalignment between SiO_2 and TiO_2 sidewalls can increase the grating strength and effectively reduce the transmission of the light inside the TiO_2 slab.

For emitters in 2D materials, bullseye Bragg grating can be selected from a broader range of materials. Materials like silicon, gallium phosphide, indium phosphide, and gallium arsenide have a higher refractive index in the visible wavelength [192]. In addition, as emitters in 2D materials positioned on top of the structure, the bandgap of the material chosen for bullseye grating is not as crucial as other wide bandgap materials like Diamond and silicon carbide (SiC).

Bullseye Bragg grating alongside micro–pillar cavities are promising candidates to increase both collection efficiency and the Purcell factor.

7.2 Defect generation in hBN

In Chapter 5, I:

- developed a treatment recipe based on O_2 plasma RIE, N_2 RTA, and O_2 plasma ash. According to this study, a single treatment can create narrow linewidth emitters.

- showed that a combination of strain and treatment could generate reproducible defect centres in hBN. It is noted that this method only worked on the silicon nanostubs sample.

- studied consecutive annealings at medium temperature on a single flake. According to the result, this approach can create ensembles of defects in the crystal lattice.

- investigated single annealing at high temperatures. Based on the result, this method can create narrower linewidth defects compared to the consecutive annealings at medium temperatures. Some of these defects showed power saturation behaviours.

- explored different fluences in the Kr^+ irradiation study and found out fluences higher than 10^{12} cm^{-2} create ensembles of defects, while the spectra of the lower fluence were quite similar to the non–irradiated sample. After annealing, I observed less broad spectra from defect centres in the sample irradiated at 10^{12} cm^{-2}. Therefore, I concluded that the fluence of 10^{12} cm^{-2} is the best choice among other fluences.

- looked into samples with different ion energies. Based on this study, the two irradiated samples with the highest ion energy created single defect–like emit-

ters. After annealing, I observed one sign of a narrow linewidth emitter in the highest energy sample.

- discovered that plasma ash suppresses background fluorescence from the substrate and increases the purity of single photon emission.

- noticed unwanted features in the spectrum, including Raman signals and laser light, in almost all spectra. These sources can affect the purity of defect centres. It is worth mentioning that I observed power saturation behaviour from some centres without any antibunching behaviour in the second–order correlation measurement.

- learned that defect centres in hBN suffer from significant instability, especially after O_2 plasma RIE and irradiation approaches. In the case of etching in RIE, I observed that generated centres bleached quickly in a few seconds, or in some cases, blinked. One way to improve the stability of defect centres is to anneal them. I realised that stability in ensembles is more substantial than a single defect centre; the latter ones disappeared over the course of several hours or days.

Based on my studies, annealing is not a promising method but a necessary step to stabilise and create a wide range of defect centres in hBN. To find the right recipe, the first step should probably be choosing the right equipment. In this work, I utilised RTA capable of annealing up to $\approx 1000\,^{\circ}\mathrm{C}$ in room conditions (ambient pressure, nitrogen environment). In addition, I only used N_2 as the annealing gas. There are many things here to explore; first, furnace tubes can also be investigated; however, some reports suggest annealing in furnace tubes resulted in weak ZPL emission. Second, other gases can be studied. Although N_2 is considered an inert gas, molecular nitrogen (N≡N) will break down into atomic nitrogen (N) at a temperature above $500\,^{\circ}\mathrm{C}$. Therefore, I annealed all samples in an active environment. Another option is to use Argon, as this gas remains inert at high temperatures. Also, some papers report that annealing in oxygen can create single defect centres in the crystal. After choosing the appropriate equipment and gas, annealing conditions can be investigated; I noticed increasing exposure time in plasma etching, annealing and plasma ashing steps would result in defects diffusing too much.

In order to create deterministic defect centres at a particular wavelength, strain following treatment was a promising route. This method's significant advantage is avoiding exfoliated flakes and only working with CVD–grown hBN. This allows me to have better control of the process and have a higher probability of creating emitters deterministically. There are some challenges to address in this approach; first, I could not detect any single photon centres. Modifying the treatment recipe can

be one of the options, but possibly the size of nanostructures is the most critically important factor. To apply higher strain to the lattice, it is mandatory to exploit smaller nanostructures like nanopillars. The disadvantage of this method is the difficulty of coupling created emitters by this approach to the photonic structures, like cavities.

Ion implantation proves to be a promising method to generate defect centres in many materials, including but not limited to Diamond, SiC, Transition–metal dichalcogenide, and hBN. It is possible to create a different range of single emitters by this approach, but also this method can be used to precisely create defects in particular places, such as the centre of a cavity. Although there was no sign of stabilised single defect centre in my work, this study is not a completed work. Going forward, the proper irradiation profile needs to be selected. Next, different annealing conditions should be explored with the correct irradiation recipe. As discussed earlier, based on my observation, defect centres created by irradiation suffer from stability, and annealing is a promising candidate to stabilise these centres. Another research pathway is to test different ion sources.

One of the directions could be a combination of the strain, irradiation, annealing and plasma ash methods. Generated defects by irradiation method proved to suffer from instability. In contrast, emitters under constant stress applied by the nanostructures are prone to instability. Therefore, I can grow/transfer hBN crystal on the nanostubs and then irradiate the sample with ions. After implementing these steps, annealing and plasma ash can be considered the next optional step.

7.3 Coherent control of electron spin of V_B^- in hBN

In Chapter 6, we:

- investigated the electron spin properties of V_B^- centres in ensembles of defects in a C–implanted hBN sample.

- showed that due to the proximity of the defect centres to the MW fields applied by CPW, a higher Rabi frequency could be achieved.

- studied Rabi oscillation and Ramsey interferometry at 90 mT and found out their dephasing times are around 30 and 3 ns, respectively.

- applied a spin–echo sequence to the V_B^- centres and achieved a spin–echo coherence time of 100 ns at 90 mT.

- showed that tilting the sample around one axis resulted in degrading spin–echo coherence time by more than half of the value reported for the non–tilted case.

Going forward, we studied one of the dynamic decoupling techniques to increase the electron spin coherence time in V_B^-. In this research, we exploited the continuous concatenated driving (CCD) to protect the spin qubit basis, allowing us to extend the Rabi dephasing time to 4 µs. In addition, we demonstrated full control of the protected qubit with a coherence time of about 800-1000 ns. Applying a feedback mechanism to stabilise the environment can be considered the next step.

In this work, we studied ensembles of defects comprising mainly V_B^- centres. The interaction of many–electron spins with a stubborn environment through hyperfine interactions is quite strong in this type of defect, resulting in a short coherence time. Instead, by studying a single defect centre, it is most likely to observe less intense interaction between nuclei and a single electron spin. It can be expected that the limiting factor for the electron spin in such a scenario would be the Larmor frequency imposed by the surrounding nuclei. If this condition is met, one can expect to detect spin coherence time of the order of milliseconds at room temperature. On the other side, it is evident that ensembles of V_B^- defects with millions of count rates have a small contrast; therefore, we can expect that the contrast of a single V_B^- defect is very small; however, this issue can be addressed by coupling this centre to a photonic structure to increase collection efficiency. Recently two other spin defects have been reported recently, both identified as single defect centres in contrast to V_B^- centres. These optically addressable single spin centres are possibly better candidates for solid–state spin platforms. In addition, I showed that by using treatment, strain, annealing and irradiation, it is possible to create a wide range of defects. Unravelling the ODMR signature of these defects can also be an exciting path to explore.

7.4 Connecting the dots

As discussed in Chapter 2, I discussed the criteria for realising quantum computing and quantum information. To achieve them, I investigated different methods to generate defect centres in hBN, designed a bullseye cavity structure, and studied the spin properties of a defect centre in hBN. Combining all this research will allow the reader to become at least one step closer to the target discussed earlier in this thesis. The methods and steps presented in this work are not limited to hBN.

APPENDIX A

Magnetisation dynamics

The precessional motion of a magnetic (dipole) moment (like the spin angular moment of electron and nucleus) in the presence of damping can be described by the Landau–Lifshitz–Gilbert (LLG) equation [193]:

$$\frac{\partial \boldsymbol{m}}{\partial t} = \underbrace{-\frac{|\gamma|}{1+\alpha^2}\ \boldsymbol{m} \times \mathbf{H}_{\text{eff}}}_{\text{gyromagnetic precession}} - \underbrace{\frac{|\gamma|\alpha}{(1+\alpha^2)|\boldsymbol{m}|}\ \boldsymbol{m} \times (\boldsymbol{m} \times \mathbf{H}_{\text{eff}})}_{\text{damping}}, \qquad \gamma = \frac{g\mu_B}{\hbar} \quad \text{(A.1)}$$

where $\boldsymbol{m}$ and $|\boldsymbol{m}|$ are the magnetic (dipole) moment and the norm of the magnetic (dipole) moment, respectively[1]. α is a phenomenological damping parameter (Gilbert damping constant), and γ is the gyromagnetic ratio. The first and the second terms are on the right–hand side of Equation (A.1) describing gyromagnetic precession and damping, respectively. In this formula, $\mathbf{H}_{\text{eff}}$ has contributions from exchange interaction, (crystal) anisotropy, dipolar field and the external field. The magnetisation is associated with the spin angular momentum through [195, 196]:

$$\boldsymbol{m} = \gamma \langle \boldsymbol{S} \rangle = \frac{g\mu_B}{\hbar} \langle \boldsymbol{S} \rangle \quad \text{(A.2)}$$

where $\boldsymbol{S}$ is the expectation of the spin operator. By defining the spin as the unit magnetisation vector:

$$\boldsymbol{S}(t) = \frac{\boldsymbol{m}(t)}{|\boldsymbol{m}(t)|}, \qquad \boldsymbol{S}^2 = 1 \qquad \textit{and} \qquad \boldsymbol{S} = (S_x, S_y, S_z) \quad \text{(A.3)}$$

Equation (A.1) can be simplified to the spin equation of motion:

$$\frac{\partial \boldsymbol{S}}{\partial t} = -\frac{|\gamma|}{1+\alpha^2}(1 + \alpha \boldsymbol{S})(\boldsymbol{S} \times \mathbf{H}_{\text{eff}}) \quad \text{(A.4)}$$

I can interpret these formulas as follows: at static equilibrium (without an external microwave field), the magnetic moment is held in its position by $\mathbf{H}_{\text{eff}}$. In the presence of a (weak and short) MW field, this pumping field exerts a small perturbative torque on the magnetic moment, resulting in a tilting magnetisation vector by a slight angle. In consequence, the effective local field will exert a restoring torque $\boldsymbol{m} \times \mathbf{H}_{\text{eff}}$. Instead of realigning into its equilibrium direction, magnetic moment precesses around the

[1] Another relevant term in this context is $\boldsymbol{M}$ which is the magnetisation per unit volume. In some textbooks, the LLG equation is developed based on this parameter [193, 194].

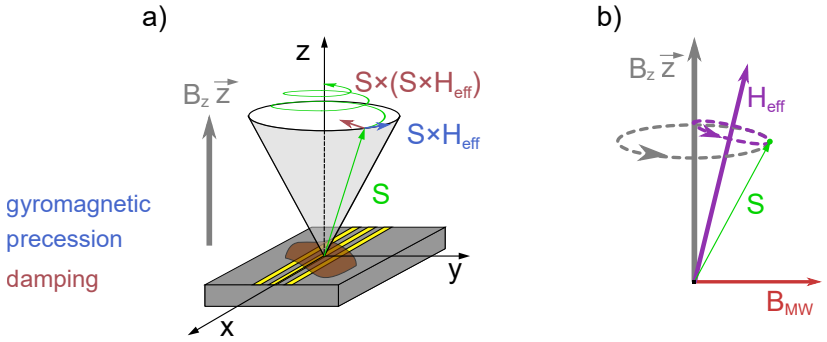

Figure A.1: Spin magnetisation trajectory. a) Magnetisation precession in the absence and presence of damping. The gyromagnetic precession and damping terms are shown in blue and red. The green vector shows the spin angular momentum (magnetisation vector), and the green spiral illustrates the trajectory of the spin vector. $\mathbf{B}_z$ is the external static magnetic field. This figure assumes that $\mathbf{H}_{\text{eff}}$ is in the same direction as $\mathbf{B}_z$. b) Precession of the spin angular momentum when $\mathbf{H}_{\text{eff}}$ is slightly off from the z–axis. The purple dashed line indicates the precession around the new local effective magnetic field. When the MW field switches off, and the local effective magnetic field returns to the $\vec{z}$ direction, the spin magnetisation vector either stays motionless (if it is already on the z–axis or starts precess around the new local effective magnetic field. In this figure, damping is not shown.

effective local field. After short MW excitation and because of the damping in the system, the magnetic moment spirals out toward its equilibrium direction after some revolutions [194]. Figure A.1.a depicts the spin angular motion in the absence and the presence of damping. This figure assumes that the effective local field ($\mathbf{H}_{\text{eff}}$) is in the same direction as the external static magnetic field. The spin spiral in this figure shows the spin trajectory toward its equilibrium direction. If the new effective local field acquires a new direction after MW pulse excitation, like purple $\mathbf{H}_{\text{eff}}$ in Figure A.1.b, the spin magnetisation vector starts precess around it (purple dashed line). When the MW pulse switches off, those spin vectors not in their equilibrium directions start precess around the equilibrium effective local field (grey dashed line) [193]. For simplicity reasons, damping is eliminated in Figure A.1.b.

APPENDIX B

Relaxation mechanisms

As shown in Chapter A, Equation (A.1) gives a good idea about magnetic moment evolution in the magnetic fields; however, it has two limitations; first, it does not explain the relaxation of magnetic moment, and second, it cannot be applied when damping does not conserve $|\boldsymbol{m}|$. To address these two limitations, one can use the Bloch–Bloembergen equation[1] [198]:

$$\frac{\partial \boldsymbol{m}_{[x,y,z]}}{\partial t} = \gamma \ (\boldsymbol{m} \times \mathbf{H}_{\text{eff}})_{[x,y,z]} - \frac{\gamma}{T} \ (\boldsymbol{m}_{[x,y,z]} - \boldsymbol{m}_{0,z}) \tag{B.1}$$

where $T = (T_2^*, T_2^*, T_1)$ represents both transverse (M_x and M_y) and the longitudinal (M_z) relaxation times of the magnetic moment. In Equation (B.1), $\boldsymbol{m}_{0,z}$ is the static saturation magnetisation which is assumed to be in the z–direction.

Interactions between the spin system and the lattice vibrations determine the quantity of T_1, and magnetic and exchange interactions within the spins system determine T_2^*. Because of this explanation, T_1 and T_2^* are also called spin relaxation and spin coherence times [199, 200]. The main difference between T_1 and T_2^* is that the former is the process in which spins reach thermal equilibrium in the z–direction whereas the latter is related to the process by which spins attain a uniform phase distribution in the transverse plane. If spontaneous relaxation is prolonged, spin–lattice relaxation is typically stimulated by the local magnetic field fluctuations that precess at Larmor frequency (and different mathematical forms of Larmor frequency between spins[2]) [201]. This frequency can be formulated as follow:

$$\omega_L = 2\pi f_L = \gamma \mathbf{B} \tag{B.2}$$

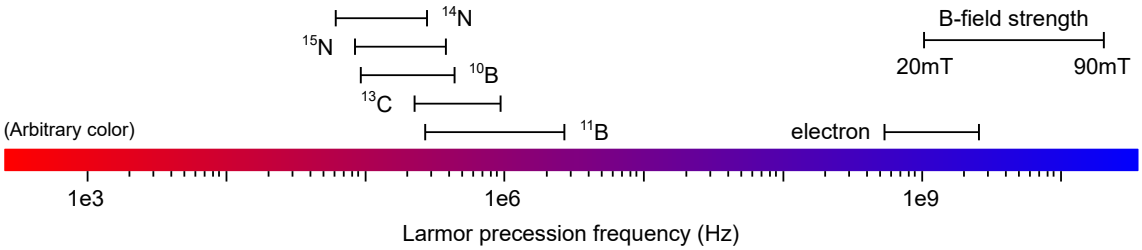

Figure B.1: Larmor precession frequency for electron and abundant nuclei in hBN. Each horizontal line represents B–field strength ranging from 20 mT to 90 mT.

[1] or Bloch equation [197].

[2] Two spins that are precessing at their Larmor frequencies, provide local on–resonant pulse to each other and the environment.

where f_L is the Larmor frequency, it identifies the magnetic moment precession frequency around the external magnetic field. The gyromagnetic ratio is inversely proportional to the particle mass, and for the case of the electron, $|\gamma_e/2\pi| \approx 28\,\mathrm{MHz\,mT^{-1}}$. Larmor precession frequency for the electron and abundant isotopes in hBN is shown in Figure B.1.

APPENDIX C

Time–dependent Schrödinger equation

The general solution of the time–dependent Schrödinger equation under the oscillatory external field after an evolution τ is [202]:

$$c_{|0\rangle}(\tau) = \left[e^{-i\delta\tau/2}\left(\cos\frac{\Omega\tau}{2}+\frac{i\delta}{\Omega}\sin\frac{\Omega\tau}{2}\right)\right]c_{|0\rangle}(0)+\left[e^{-i\delta\tau/2}\left(\frac{i\Omega_R^*}{\Omega}\sin\frac{\Omega\tau}{2}\right)\right]c_{|1\rangle}(0) \quad \text{(C.1)}$$

$$c_{|1\rangle}(\tau) = \left[e^{-i\delta\tau/2}\left(\frac{i\Omega_R}{\Omega}\sin\frac{\Omega\tau}{2}\right)\right]c_{|0\rangle}(0)+\left[e^{-i\delta\tau/2}\left(\cos\frac{\Omega\tau}{2}-\frac{i\delta}{\Omega}\sin\frac{\Omega\tau}{2}\right)\right]c_{|1\rangle}(0) \quad \text{(C.2)}$$

where $c_{|0\rangle}$ and $c_{|1\rangle}$ are the probability amplitude of state $|0\rangle$ and $|1\rangle$, respectively. In the above equations, it is assumed that the electron spin is first initialised in the $|0\rangle$ state. It is noted that if monochromatic plane wave generated by MW field is constant along its field polarisation vector, Rabi oscillation can be taken to be a purely real number; therefore $\Omega_R = \Omega_R^*$. Under proper spin initialisation in which $c_{|0\rangle}(0) = 1$ and $c_{|1\rangle}(0) = 0$, Equation (C.1) and Equation (C.2) are simplified to:

$$c_{|0\rangle}(\tau) = e^{-i\delta\tau/2}\left(\cos\frac{\Omega\tau}{2}+\frac{i\delta}{\Omega}\sin\frac{\Omega\tau}{2}\right) \quad \text{(C.3)}$$

$$c_{|1\rangle}(\tau) = e^{-i\delta\tau/2}\left(\frac{i\Omega_R}{\Omega}\sin\frac{\Omega\tau}{2}\right) \quad \text{(C.4)}$$

$$|\Omega| = \sqrt{\delta^2+\Omega_R^2} \quad \text{(C.5)}$$

The amplitude of Rabi angular frequency in Equation (C.5) describes the coupling strength of the electron spins to the MW field ($\Omega_R = 2\pi f_R V_{MW}$) [203, 204].

Bibliography

[1] R. P. Feynman, "Simulating physics with computers," *International Journal of Theoretical Physics*, vol. 21, no. 6-7, pp. 467–488, 1982. DOI: 10.1007/BF02650179.

[2] J. Preskill, *Lecture Notes for Physics 229: Quantum Information and Computation*. California Institute of Technology, 1998.

[3] D. P. DiVincenzo, "The physical implementation of quantum computation," *arxiv*, vol. 48, no. 9-11, pp. 771–783, 2000. DOI: 10.1002/1521-3978(200009)48:9/11<771::AID-PROP771>3.0.CO;2-E.

[4] G. Zhang, Y. Cheng, J. P. Chou, and A. Gali, "Material platforms for defect qubits and single-photon emitters," *Applied Physics Reviews*, vol. 7, no. 3, 2020. DOI: 10.1063/5.0006075.

[5] S. Buckley, K. Rivoire, and J. Vučković, "Engineered quantum dot single-photon sources," *Reports on Progress in Physics*, vol. 75, no. 12, 2012. DOI: 10.1088/0034-4885/75/12/126503.

[6] M. Atatüre, D. R. Englund, N. Vamivakas, S. Y. Lee, and J. Wrachtrup, "Material platforms for spin-based photonic quantum technologies," *Nature Reviews Materials*, vol. 3, no. 5, pp. 38–51, 2018. DOI: 10.1038/s41578-018-0008-9.

[7] E. Waks, A. Zeevi, and Y. Yamamoto, "Security of quantum key distribution with entangled photons against individual attacks," *Physical Review A - Atomic, Molecular, and Optical Physics*, vol. 65, no. 5, p. 16, 2002. DOI: 10.1103/PhysRevA.65.052310.

[8] P. A. Hiskett *et al.*, "Long-distance quantum key distribution in optical fibre," *New Journal of Physics*, vol. 8, Sep. 2006. DOI: 10.1088/1367-2630/8/9/193.

[9] V. Krutyanskiy, M. Meraner, J. Schupp, V. Krcmarsky, H. Hainzer, and B. P. Lanyon, "Light-matter entanglement over 50 km of optical fibre," *npj Quantum Information*, vol. 5, no. 1, Dec. 2019. DOI: 10.1038/s41534-019-0186-3.

[10] A. Dréau, A. Tcheborateva, A. E. Mahdaoui, C. Bonato, and R. Hanson, "Quantum Frequency Conversion of Single Photons from a Nitrogen-Vacancy Center in Diamond to Telecommunication Wavelengths," *Physical Review Applied*, vol. 9, no. 6, Jun. 2018. DOI: 10.1103/PhysRevApplied.9.064031.

[11] B. Hensen *et al.*, "Loophole-free Bell inequality violation using electron spins separated by 1.3 kilometres," *Nature*, vol. 526, no. 7575, pp. 682–686, 2015. DOI: 10.1038/nature15759.

[12] T. Ruster, C. T. Schmiegelow, H. Kaufmann, C. Warschburger, F. Schmidt-Kaler, and U. G. Poschinger, "A long-lived Zeeman trapped-ion qubit," *arxiv*, Jun. 2016. DOI: 10.1007/s00340-016-6527-4.

[13] C. D. Bruzewicz, J. Chiaverini, R. McConnell, and J. M. Sage, "Trapped-ion quantum computing: Progress and challenges," *Applied Physics Reviews*, vol. 6, no. 2, 2019. DOI: 10.1063/1.5088164.

[14] C. H. Bennett and D. P. DiVincenzo, "Quantum Information and Computation," *Nature*, vol. 404, 2000. DOI: 10.1088/0305-4470/34/35/001.

[15] S. Majety, P. Saha, V. A. Norman, and M. Radulaski, "Quantum information processing with integrated silicon carbide photonics," *Journal of Applied Physics*, vol. 131, no. 13, 2022. DOI: 10.1063/5.0077045.

[16] J. Kim, O. Benson, H. Kan, and Y. Yamamoto, "A single-photon turnstile device," *Nature*, vol. 397, no. 6719, pp. 500–503, Feb. 1999. DOI: 10.1038/17295.

[17] P. Michler *et al.*, "A quantum dot single-photon turnstile device," *Science*, vol. 290, no. 5500, pp. 2282–2285, 2000. DOI: 10.1126/science.290.5500.2282.

[18] R. M. Stevenson, R. J. Young, P. Atkinson, K. Cooper, D. A. Ritchie, and A. J. Shields, "A semiconductor source of triggered entangled photon pairs," *Nature*, vol. 439, no. 7073, pp. 178–182, 2006. DOI: 10.1038/nature04446.

[19] D. D. Awschalom, D. Loss, and N. Smarth, *Semiconductor Spintronics and Quantum Computation*. Springer, 2002, ISBN: 978-3-642-08445-4.

[20] E. Meyer-Scott, C. Silberhorn, and A. Migdall, "Single-photon sources: Approaching the ideal through multiplexing," *Review of Scientific Instruments*, vol. 91, no. 4, p. 041 101, 2020. DOI: 10.1063/5.0003320.

[21] P. Senellart, G. Solomon, and A. White, "High-performance semiconductor quantum-dot single-photon sources," *Nature Nanotechnology*, vol. 12, no. 11, pp. 1026–1039, 2017. DOI: 10.1038/nnano.2017.218.

[22] K. G. Fehler *et al.*, "Hybrid quantum photonics based on artificial atoms placed inside one hole of a photonic crystal cavity," *arxiv*, pp. 1–8, 2020.

[23] F. Peyskens, C. Chakraborty, M. Muneeb, D. Van Thourhout, and D. R. Englund, "Integration of single photon emitters in 2D layered materials with a silicon nitride photonic chip," *Nature Communications*, vol. 10, no. 1, pp. 1–18, 2019. DOI: 10.1038/s41467-019-12421-0.

[24] J. R. Weber *et al.*, "Quantum computing with defects," *Proceedings of the National Academy of Sciences of the United States of America*, vol. 107, no. 19, pp. 8513–8518, 2010. DOI: 10.1073/pnas.1003052107.

[25] L. Dusanowski *et al.*, "Optical charge injection and coherent control of a quantum-dot spin-qubit emitting at telecom wavelengths," *Nature Communications*, pp. 1–8, 2022. DOI: 10.1038/s41467-022-28328-2.

[26] D. D. Awschalom, R. Hanson, J. Wrachtrup, and B. B. Zhou, "Quantum technologies with optically interfaced solid-state spins," *Nature Photonics*, vol. 12, no. 9, pp. 516–527, 2018. DOI: 10.1038/s41566-018-0232-2.

[27] A. J. Ramsay, "A review of the coherent optical control of the exciton and spin states of semiconductor quantum dots," *Semiconductor Science and Technology*, vol. 25, no. 10, 2010. DOI: 10.1088/0268-1242/25/10/103001.

[28] W. Yao, R. B. Liu, and L. J. Sham, "Theory of control of the spin-photon interface for quantum networks," *Physical Review Letters*, vol. 95, no. 3, pp. 1–4, 2005. DOI: 10.1103/PhysRevLett.95.030504.

[29] T. Wilk, S. C. Webster, A. Kuhn, and G. Rempe, "Single-Atom Single-Photon Quantum Interface," *Science*, vol. 317, no. July, 2007.

[30] M. Ruf, N. H. Wan, H. Choi, D. R. Englund, and R. Hanson, "Quantum networks based on color centers in diamond," *arxiv*, 2021.

[31] R. J. Warburton *et al.*, "Optical emission from a charge-tunable quantum ring," *Nature*, vol. 405, no. 6789, pp. 926–929, Jun. 2000. DOI: 10.1038/35016030.

[32] E. Janitz, M. K. Bhaskar, and L. Childress, "Cavity quantum electrodynamics with color centers in diamond," *Optica*, vol. 7, no. 10, p. 1232, Oct. 2020. DOI: 10.1364/OPTICA.398628.

[33] E. Togan *et al.*, "Quantum entanglement between an optical photon and a solid-state spin qubit," *Nature*, vol. 466, no. 7307, pp. 730–734, 2010. DOI: 10.1038/nature09256.

[34] I. P. Radko *et al.*, "Determining the internal quantum efficiency of shallow-implanted nitrogen-vacancy defects in bulk diamond," *Optics Express*, vol. 24, no. 24, pp. 644–647, 2016.

[35] R. Nagy *et al.*, "Quantum Properties of Dichroic Silicon Vacancies in Silicon Carbide," *Physical Review Applied*, vol. 9, no. 3, pp. 25–27, 2018. DOI: 10.1103/PhysRevApplied.9.034022.

[36] N. Nikolay *et al.*, "Direct measurement of quantum efficiency of single-photon emitters in hexagonal boron nitride," *Optica*, vol. 6, no. 8, p. 1084, 2019. DOI: 10.1364/optica.6.001084.

[37] A. Dietrich, M. W. Doherty, I. Aharonovich, and A. Kubanek, "Solid-state single photon source with Fourier transform limited lines at room temperature," *Physical Review B*, vol. 101, no. 8, pp. 1–6, 2020. DOI: 10.1103/PhysRevB.101.081401.

[38] A. Jarmola, V. M. Acosta, K. Jensen, S. Chemerisov, and D. Budker, "Temperature- and magnetic-field-dependent longitudinal spin relaxation in nitrogen-vacancy ensembles in diamond," *Physical Review Letters*, vol. 108, no. 19, pp. 1–5, 2012. DOI: 10.1103/PhysRevLett.108.197601.

[39] A. Bechtold *et al.*, "Three-stage decoherence dynamics of an electron spin qubit in an optically active quantum dot," *Nature Physics*, vol. 11, no. 12, pp. 1005–1008, 2015. DOI: 10.1038/nphys3470.

[40] R. Stockill *et al.*, "Quantum dot spin coherence governed by a strained nuclear environment," *Nature Communications*, vol. 7, no. May, pp. 1–7, 2016. DOI: 10.1038/ncomms12745.

[41] C. E. Bradley *et al.*, "Robust quantum-network memory based on spin qubits in isotopically engineered diamond," *npj Quantum Information*, 2022. DOI: 10.1038/s41534-022-00637-w.

[42] C. P. Anderson *et al.*, "Five-second coherence of a single spin with single-shot readout in silicon carbide," *Science Advances*, vol. 5912, no. February, 2022.

[43] A. Gottscholl *et al.*, "Room temperature coherent control of spin defects in hexagonal boron nitride," *Science Advances*, 2021. DOI: 10.1126/sciadv.abf3630.

[44] A. J. Ramsay *et al.*, "Coherence protection of spin qubits in hexagonal boron nitride," *Nature Communications*, vol. 14, no. 1, p. 461, Jan. 2023. DOI: 10.1038/s41467-023-36196-7.

[45] M. E. Reimer and C. Cher, "The quest for a perfect single-photon source," *Nature Photonics*, vol. 13, no. 11, pp. 734–736, 2019. DOI: 10.1038/s41566-019-0544-x.

[46] E. M. Purcell, "Spontaneous emission probabilities at radio frequencies," *Phys. Rev*, vol. 69, p. 681, 1946. DOI: 10.1007/978-1-4899-3805-3{_}30.

[47] K. Kozdon, I. T. Durham, and A. Dragan, "Measuring acceleration using the purcell effect," *Quantum*, vol. 2, Aug. 2018. DOI: 10.22331/q-2018-08-18-83.

[48] M. Fox, *Quantum Optics - An Introduction*. Oxford University Press, 2006, ISBN: 9780198566731.

[49] W. L. Barnes *et al.*, "Solid-state single photon sources : light collection strategies," *The european physical journal D*, vol. 210, pp. 197–210, 2002. DOI: 10.1140/epjd/e20020024.

[50] O. Gazzano *et al.*, "Bright solid-state sources of indistinguishable single photons," *Nature Communications*, vol. 4, 2013. DOI: 10.1038/ncomms2434.

[51] H. Wang *et al.*, "Towards optimal single-photon sources from polarized microcavities," *Nature Photonics*, vol. 13, no. 11, pp. 770–775, 2019. DOI: 10.1038/s41566-019-0494-3.

[52] J. Zheng, A. C. Liapis, E. H. Chen, C. T. Black, and D. R. Englund, "Chirped circular dielectric gratings for near-unity collection efficiency from quantum emitters in bulk diamond," *Optics Express*, vol. 89, no. 3, 2017. DOI: 10.1103/RevModPhys.89.035002.

[53] D. Komisar, S. Kumar, Y. Kan, C. Wu, and S. I. Bozhevolnyi, "Generation of Radially Polarized Single Photons with Plasmonic Bullseye Antennas," *ACS Photonics*, 2021. DOI: 10.1021/acsphotonics.1c00459.

[54] N. M. H. Duong *et al.*, "Enhanced Emission from WSe2 Monolayers Coupled to Circular Bragg Gratings," *ACS Photonics*, vol. 5, no. 10, pp. 3950–3955, 2018. DOI: 10.1021/acsphotonics.8b00865.

[55] O. Mey *et al.*, "Enhancement of the Monolayer Tungsten Disulfide Exciton Photoluminescence with a Two-Dimensional Material/Air/Gallium Phosphide In-Plane Microcavity," *ACS Nano*, vol. 13, no. 5, pp. 5259–5267, May 2019. DOI: 10.1021/acsnano.8b09659.

[56] B. Chen *et al.*, "Simultaneously enhanced linear and nonlinear photon generations from WS2by using dielectric circular Bragg resonators," *Nanophotonics*, vol. 9, no. 8, pp. 2587–2592, Aug. 2020. DOI: 10.1515/nanoph-2020-0143.

[57] N. Bernhardt *et al.*, "Large few-layer hexagonal boron nitride flakes for nonlinear optics," *arxiv*, no. 2, pp. 1–13, 2020.

[58] O. Iff *et al.*, "Purcell-Enhanced Single Photon Source Based on a Deterministically Placed WSe2 Monolayer Quantum Dot in a Circular Bragg Grating Cavity," *Nano Letters*, 2021. DOI: 10.1021/acs.nanolett.1c00978.

[59] O. Iff *et al.*, "Hyperspectral study of the coupling between trions in WSe2 monolayers to a circular Bragg grating cavity," *Comptes Rendus Physique*, 2021.

[60] S. Ren, Q. Tan, and J. Zhang, "Review on the quantum emitters in two-dimensional materials," *Journal of Semiconductors*, vol. 40, no. 7, 2019. DOI: 10.1088/1674-4926/40/7/071903.

[61] W. Liu *et al.*, "Spin-active defects in hexagonal boron nitride," *Materials for Quantum Technology*, vol. 2, no. 3, p. 032 002, Sep. 2022. DOI: 10.1088/2633-4356/ac7e9f.

[62] M. Abdi, J. P. Chou, A. Gali, and M. B. Plenio, "Color Centers in Hexagonal Boron Nitride Monolayers: A Group Theory and Ab Initio Analysis," *ACS Photonics*, vol. 5, no. 5, pp. 1967–1976, May 2018. DOI: 10.1021/acsphotonics.7b01442.

[63] V. Ivády *et al.*, "Ab initio theory of the negatively charged boron vacancy qubit in hexagonal boron nitride," *npj Computational Materials*, vol. 6, no. 1, pp. 1–6, 2020. DOI: 10.1038/s41524-020-0305-x.

[64] L. Weston, D. Wickramaratne, M. Mackoit, A. Alkauskas, and C. G. Van De Walle, "Native point defects and impurities in hexagonal boron nitride," *Physical Review B*, vol. 97, no. 21, Jun. 2018. DOI: 10.1103/PhysRevB.97.214104.

[65] F. Wu, A. Galatas, R. Sundararaman, D. Rocca, and Y. Ping, "First-principles engineering of charged defects for two-dimensional quantum technologies," *Physical Review Materials*, vol. 1, no. 7, Dec. 2017. DOI: 10.1103/PhysRevMaterials.1.071001.

[66] A. Sajid, J. R. Reimers, R. Kobayashi, and M. J. Ford, "Theoretical spectroscopy of the VNNB defect in hexagonal boron nitride," *Physical Review B*, vol. 102, no. 14, Oct. 2020. DOI: 10.1103/PhysRevB.102.144104.

[67] P. Auburger and A. Gali, "Towards ab initio identification of paramagnetic substitutional carbon defects in hexagonal boron nitride acting as quantum bits," *Physical Review B*, vol. 104, no. 7, Aug. 2021. DOI: 10.1103/PhysRevB.104.075410.

[68] M. MacKoit-Sinkevičiene, M. MacIaszek, C. G. Van De Walle, and A. Alkauskas, "Carbon dimer defect as a source of the 4.1 eV luminescence in hexagonal boron nitride," *Applied Physics Letters*, vol. 115, no. 21, 2019. DOI: 10.1063/1.5124153.

[69] A. Sajid, J. R. Reimers, and M. J. Ford, "Defect states in hexagonal boron nitride: Assignments of observed properties and prediction of properties relevant to quantum computation," *Physical Review B*, vol. 97, no. 6, pp. 1–9, 2018. DOI: 10.1103/PhysRevB.97.064101.

[70] N. Mendelson *et al.*, "Identifying Carbon as the Source of Visible Single Photon Emission from Hexagonal Boron Nitride," *Nature Materials*, 2020. DOI: 10.1038/s41563-020-00850-y.

[71] L. J. Martínez *et al.*, "Efficient single photon emission from a high-purity hexagonal boron nitride crystal," *Physical Review B*, vol. 94, no. 12, pp. 1–5, 2016. DOI: 10.1103/PhysRevB.94.121405.

[72] Z. Q. Xu *et al.*, "Single photon emission from plasma treated 2D hexagonal boron nitride," *Nanoscale*, vol. 10, no. 17, pp. 7957–7965, 2018. DOI: 10.1039/c7nr08222c.

[73] N. Mendelson *et al.*, "Engineering and Tuning of Quantum Emitters in Few-Layer Hexagonal Boron Nitride," *ACS Nano*, vol. 13, no. 3, pp. 3132–3140, 2019. DOI: 10.1021/acsnano.8b08511.

[74] J. Comtet *et al.*, "Wide-Field Spectral Super-Resolution Mapping of Optically Active Defects in Hexagonal Boron Nitride," *Nano Letters*, vol. 19, no. 4, pp. 2516–2523, 2019. DOI: 10.1021/acs.nanolett.9b00178.

[75] H. L. Stern *et al.*, "Spectrally Resolved Photodynamics of Individual Emitters in Large-Area Monolayers of Hexagonal Boron Nitride," *ACS Nano*, vol. 13, no. 4, pp. 4538–4547, 2019. DOI: 10.1021/acsnano.9b00274.

[76] T. Vogl, G. Campbell, B. C. Buchler, Y. Lu, and P. K. Lam, "Fabrication and Deterministic Transfer of High-Quality Quantum Emitters in Hexagonal Boron Nitride," *ACS Photonics*, vol. 5, no. 6, pp. 2305–2312, 2018. DOI: 10.1021/acsphotonics.8b00127.

[77] T. Vogl, M. W. Doherty, B. C. Buchler, Y. Lu, and P. K. Lam, "Atomic localization of quantum emitters in multilayer hexagonal boron nitride," *Nanoscale*, vol. 11, no. 30, pp. 14 362–14 371, 2019. DOI: 10.1039/c9nr04269e.

[78] C. Li, Z. Q. Xu, N. Mendelson, M. Kianinia, M. Toth, and I. Aharonovich, "Purification of single-photon emission from hBN using post-processing treatments," *Nanophotonics*, vol. 8, no. 11, pp. 2049–2055, 2019. DOI: 10.1515/nanoph-2019-0099.

[79] Y. Chen *et al.*, "Generation of High-Density Quantum Emitters in High-Quality, Exfoliated Hexagonal Boron Nitride," *ACS Applied Materials and Interfaces*, no. i, 2021. DOI: 10.1021/acsami.1c14863.

[80] C. Chakraborty, N. Vamivakas, and D. R. Englund, "Advances in quantum light emission from 2D materials," *Nanophotonics*, vol. 8, no. 11, pp. 2017–2032, 2019. DOI: 10.1515/nanoph-2019-0140.

[81] M. Turunen *et al.*, "Quantum photonics with layered 2D materials," *Nature Reviews Physics*, 2022. DOI: 10.1038/s42254-021-00408-0.

[82] I. Aharonovich, D. R. Englund, and M. Toth, "Solid-state single-photon emitters," *Nature Photonics*, vol. 10, no. 10, pp. 631–641, 2016. DOI: 10.1038/nphoton.2016.186.

[83] C. Bradac, W. Gao, J. Forneris, M. E. Trusheim, and I. Aharonovich, "Quantum nanophotonics with group IV defects in diamond," *Nature Communications*, vol. 10, no. 1, pp. 1–13, 2019. DOI: 10.1038/s41467-019-13332-w.

[84] L. C. Bassett, A. Alkauskas, A. L. Exarhos, and K.-M. C. Fu, "Quantum defects by design," *Nanophotonics*, vol. 8, no. 11, pp. 1867–1888, 2019. DOI: 10.1515/nanoph-2019-0211.

[85] N. V. Proscia *et al.*, "Near-deterministic activation of room-temperature quantum emitters in hexagonal boron nitride," *Optica*, vol. 5, no. 9, p. 1128, 2018. DOI: 10.1364/optica.5.001128.

[86] C. Li *et al.*, "Scalable and Deterministic Fabrication of Quantum Emitter Arrays from Hexagonal Boron Nitride," *Nano Letters*, vol. 21, no. 8, pp. 3626–3632, 2021. DOI: 10.1021/acs.nanolett.1c00685.

[87] S. B. Van Dam *et al.*, "Optical coherence of diamond nitrogen-vacancy centers formed by ion implantation and annealing," *Physical Review B*, vol. 99, no. 16, p. 161 203, 2019. DOI: 10.1103/PhysRevB.99.161203.

[88] E. Hunt, A. Opsvig, and C. Moore, "NV Formation through Repeated Annealing," *arxiv*, pp. 1–9, 2020.

[89] T. T. Tran, K. Bray, M. J. Ford, M. Toth, and I. Aharonovich, "Quantum emission from hexagonal boron nitride monolayers," *Nature Nanotechnology*, vol. 11, no. 1, pp. 37–41, 2016. DOI: 10.1038/nnano.2015.242.

[90] T. T. Tran *et al.*, "Robust multicolor single photon emission from point defects in hexagonal boron nitride," *ACS Nano*, vol. 10, 2016. DOI: 10.1021/acsnano.6b03602.

[91] C. Lyu *et al.*, "Single-photon emission from two-dimensional hexagonal boron nitride annealed in a carbon-rich environment," *Applied Physics Letters*, vol. 117, no. 24, p. 244 002, 2020. DOI: 10.1063/5.0025792.

[92] N. Chejanovsky *et al.*, "Structural Attributes and Photodynamics of Visible Spectrum Quantum Emitters in Hexagonal Boron Nitride," *Nano Letters*, vol. 16, no. 11, pp. 7037–7045, 2016. DOI: 10.1021/acs.nanolett.6b03268.

[93] S. Choi *et al.*, "Engineering and Localization of Quantum Emitters in Large Hexagonal Boron Nitride Layers," *ACS Applied Materials and Interfaces*, vol. 8, no. 43, pp. 29 642–29 648, 2016. DOI: 10.1021/acsami.6b09875.

[94] G. Grosso *et al.*, "Tunable and high-purity room temperature single-photon emission from atomic defects in hexagonal boron nitride," *Nature Communications*, vol. 8, no. 1, 2017. DOI: 10.1038/s41467-017-00810-2.

[95] N. M. H. Duong *et al.*, "Effects of High-Energy Electron Irradiation on Quantum Emitters in Hexagonal Boron Nitride," *ACS Applied Materials and Interfaces*, vol. 10, no. 29, pp. 24 886–24 891, 2018. DOI: 10.1021/acsami.8b07506.

[96] A. Gottscholl *et al.*, "Initialization and read-out of intrinsic spin defects in a van der Waals crystal at room temperature," *Nature Materials*, vol. 19, no. 5, pp. 540–545, 2020. DOI: 10.1038/s41563-020-0619-6.

[97] N. Chejanovsky *et al.*, "Single-spin resonance in a van der Waals embedded paramagnetic defect," *Nature Materials*, vol. 20, no. 8, pp. 1079–1084, 2021. DOI: 10.1038/s41563-021-00979-4.

[98] M. Kianinia, S. White, J. E. Fröch, C. Bradac, and I. Aharonovich, "Generation of Spin Defects in Hexagonal Boron Nitride," *ACS Photonics*, vol. 7, no. 8, pp. 2147–2152, 2020. DOI: 10.1021/acsphotonics.0c00614.

[99] P. Kehayias *et al.*, "Microwave saturation spectroscopy of nitrogen-vacancy ensembles in diamond," *Physical Review B*, vol. 245202, pp. 1–8, 2014. DOI: 10.1103/PhysRevB.89.245202.

[100] S. Baber *et al.*, "Excited State Spectroscopy of Boron Vacancy Defects in Hexagonal Boron Nitride Using Time-Resolved Optically Detected Magnetic Resonance," *Nano Letters*, vol. 22, no. 1, pp. 461–467, 2021. DOI: 10.1021/acs.nanolett.1c04366.

[101] R. H. Brown and R. Twiss, "LXXIV. A new type of interferometer for use in radio astronomy," *The London, Edinburgh, and Dublin Philosophical Magazine and Journal of Science*, vol. 45, no. 366, pp. 663–682, 1954.

[102] K. S. Yee, "Numerical Solution of Initial Boundary Value Problems Involving Maxwell's Equations in Isotropic Media," *IEEE Transactions on Antennas and Propagation*, 1966. DOI: 10.1109/TAP.1966.1138693.

[103] D. C. Unitt, A. J. Bennett, P. Atkinson, D. A. Ritchie, and A. J. Shields, "Polarization control of quantum dot single-photon sources via a dipole-dependent Purcell effect," *Physical Review B - Condensed Matter and Materials Physics*, vol. 72, no. 3, Jul. 2005. DOI: 10.1103/PhysRevB.72.033318.

[104] A. Castellanos-Gomez *et al.*, "Deterministic transfer of two-dimensional materials by all-dry viscoelastic stamping," *2D Materials*, vol. 1, no. 1, Jun. 2014. DOI: 10.1088/2053-1583/1/1/011002.

[105] M. M. Benameur, B. Radisavljevic, J. S. Héron, S. Sahoo, H. Berger, and A. Kis, "Visibility of dichalcogenide nanolayers," *Nanotechnology*, vol. 22, no. 12, Mar. 2011. DOI: 10.1088/0957-4484/22/12/125706.

[106] P. Blake *et al.*, "Making graphene visible," *Applied Physics Letters*, vol. 91, no. 6, 2007. DOI: 10.1063/1.2768624.

[107] M. E. Levinshteĭn, S. L. Rumyantsev, and M. Shur, *Properties of Advanced Semiconductor Materials: GaN, AlN, InN, BN, SiC, SiGe*. 2001, ISBN: 978-0-471-35827-5.

[108] M. Auge, F. Junge, and H. Hofsäss, "Laterally controlled ultra-low energy ion implantation using electrostatic masking," *Nuclear Instruments and Methods in Physics Research, Section B: Beam Interactions with Materials and Atoms*, vol. 512, pp. 96–101, Feb. 2022. DOI: 10.1016/j.nimb.2021.12.001.

[109] S. P. Adiga *et al.*, *Ultrananocrystalline Diamond: Synthesis, Properties, and Applications*, second, O. A. Shenderova and D. M. Gruen, Eds. 2012, ISBN: 9781437734652. DOI: 10.1016/B978-1-4377-3465-2.00010-4.

[110] J. R. Reimers *et al.*, "Photoluminescence, photophysics, and photochemistry of the VB- defect in hexagonal boron nitride," *Physical Review B*, vol. 102, no. 14, p. 144 105, 2020. DOI: 10.1103/PhysRevB.102.144105.

[111] F. F. Murzakhanov *et al.*, "Electron-nuclear coherent coupling and nuclear spin readout through optically polarised VB- spin states in hBN," *Nano Letters*, 2022. DOI: 10.1021/acs.nanolett.1c04610.

[112] P. V. Klimov, A. L. Falk, D. J. Christle, V. V. Dobrovitski, and D. D. Awschalom, "Quantum entanglement at ambient conditions in a macroscopic solid-state spin ensemble," *Science Advances*, vol. 1, no. 10, pp. 1–8, 2015. DOI: 10.1126/sciadv.1501015.

[113] J. F. Barry *et al.*, "Sensitivity optimization for NV-diamond magnetometry," *Reviews of Modern Physics*, vol. 92, no. 1, p. 15 004, 2020. DOI: 10.1103/RevModPhys.92.015004.

[114] X. Gao *et al.*, "High-Contrast Plasmonic-Enhanced Shallow Spin Defects in Hexagonal Boron Nitride for Quantum Sensing," *Nano Letters*, 2021. DOI: 10.1021/acs.nanolett.1c02495.

[115] T. Wolf *et al.*, "Subpicotesla diamond magnetometry," *Physical Review X*, vol. 5, no. 4, pp. 1–10, 2015. DOI: 10.1103/PhysRevX.5.041001.

[116] Z. Mu *et al.*, "Excited-State Optically Detected Magnetic Resonance of Spin Defects in Hexagonal Boron Nitride," *Physical Review Letters*, 2022. DOI: 10.1103/PhysRevLett.128.216402.

[117] S. Haroche and J.-M. Raimond, *Exploring the Quantum: Atoms Cavities and Photons*. Oxford University Press, 2006, ISBN: 0198509146.

[118] A. Kuhn and D. Ljunggren, "Cavity-based single-photon sources," *Contemporary Physics*, vol. 51, no. 4, pp. 289–313, 2010. DOI: 10.1080/00107511003602990.

[119] S. K. Andersen *et al.*, "Hybrid Plasmonic Bullseye Antennas for Efficient Photon Collection," *ACS Photonics*, vol. 5, no. 3, pp. 692–698, 2018. DOI: 10.1021/acsphotonics.7b01194.

[120] H. Wang *et al.*, "On-Demand Semiconductor Source of Entangled Photons Which Simultaneously Has High Fidelity, Efficiency, and Indistinguishability," *Physical Review Letters*, vol. 122, no. 11, pp. 1–6, 2019. DOI: 10.1103/PhysRevLett.122.113602.

[121] M. Davanço, M. T. Rakher, D. Schuh, A. Badolato, and K. Srinivasan, "A circular dielectric grating for vertical extraction of single quantum dot emission," *Applied Physics Letters*, vol. 99, no. 4, pp. 4–6, 2011. DOI: 10.1063/1.3615051.

[122] R. Chikkaraddy *et al.*, "Single-molecule strong coupling at room temperature in plasmonic nanocavities," *Nature*, vol. 535, no. 7610, pp. 127–130, 2016. DOI: 10.1038/nature17974.

[123] K. J. Russell, T. L. Liu, S. Cui, and E. L. Hu, "Large spontaneous emission enhancement in plasmonic nanocavities," *Nature Photonics*, vol. 6, no. 7, pp. 459–462, 2012. DOI: 10.1038/nphoton.2012.112.

[124] T. B. Hoang, G. M. Akselrod, and M. H. Mikkelsen, "Ultrafast Room-Temperature Single Photon Emission from Quantum Dots Coupled to Plasmonic Nanocavities," *Nano Letters*, vol. 16, no. 1, pp. 270–275, 2015. DOI: 10.1021/acs.nanolett.5b03724.

[125] H. Abudayyeh *et al.*, "Overcoming the rate-directionality tradeoff: a room-temperature ultrabright quantum light source," *arxiv*, pp. 1–26, 2020.

[126] L. Li, H. Choi, M. Heuck, and D. R. Englund, "Field-based design of a resonant dielectric antenna for coherent spin-photon interfaces," *Optics Express*, vol. 29, no. 11, p. 16 469, 2021. DOI: 10.1364/oe.419773.

[127] L. Sapienza, M. Davanço, A. Badolato, and K. Srinivasan, "Nanoscale optical positioning of single quantum dots for bright and pure single-photon emission," *Nature Communications*, vol. 6, 2015. DOI: 10.1038/ncomms8833.

[128] L. Li *et al.*, "Efficient photon collection from a nitrogen vacancy center in a circular bullseye grating," *Nano Letters*, vol. 15, no. 3, pp. 1493–1497, 2015. DOI: 10.1021/nl503451j.

[129] R. Waltrich *et al.*, "A Robust Coherent Single-Photon Interface for Moderate-NA Optics Based on SiV Center in Nanodiamonds and a Plasmonic Bullseye Antenna," *arxiv*, 2021.

[130] A. Barbiero, J. Huwer, J. Skiba-Szymanska, T. Müller, R. M. Stevenson, and A. J. Shields, "Design study for an efficient semiconductor quantum light source operating in the telecom C-band based on an electrically-driven circular Bragg grating," *Optics Express*, vol. 30, no. 7, p. 10 919, 2022. DOI: 10.1364/oe.452328.

[131] S. Ates, L. Sapienza, M. Davanco, A. Badolato, and K. Srinivasan, "Bright single-photon emission from a quantum dot in a circular bragg grating microcavity," *IEEE Journal on Selected Topics in Quantum Electronics*, vol. 18, no. 6, pp. 1711–1721, 2012. DOI: 10.1109/JSTQE.2012.2193877.

[132] L. Rickert, T. Kupko, S. Rodt, S. Reitzenstein, and T. Heindel, "Optimized designs for telecom-wavelength quantum light sources based on hybrid circular Bragg gratings," *Optics Express*, vol. 27, no. 25, p. 36 824, 2019. DOI: 10.1364/oe.27.036824.

[133] A. E. Krasnok *et al.*, "An antenna model for the Purcell effect," *Scientific Reports*, vol. 5, pp. 1–16, 2015. DOI: 10.1038/srep12956.

[134] A. L. Crook *et al.*, "Purcell enhancement of a single silicon carbide color center with coherent spin control," *Nano Letters*, vol. 20, no. 5, pp. 3427–3434, 2020. DOI: 10.1021/acs.nanolett.0c00339.

[135] B. Gayral and J. M. Gerard, "Strong Purcell eeect for InAs quantum boxes in high-Q wet-etched microdisks," Tech. Rep., 2000, pp. 641–645.

[136] M. Nakadai, T. Asano, and S. Noda, "Electrically controlled on-demand photon transfer between high-Q photonic crystal nanocavities on a silicon chip," *Nature Photonics*, vol. 16, no. February, 2021. DOI: 10.1038/s41566-021-00910-y.

[137] H. Raniwala, S. Krastanov, M. Eichenfield, and D. R. Englund, "A spin-optomechanical quantum interface enabled by an ultrasmall mechanical and optical mode volume cavity," *arxiv*, vol. c, pp. 1–13, 2022.

[138] D. G. Baranov, M. Wersäll, J. Cuadra, T. J. Antosiewicz, and T. Shegai, "Novel Nanostructures and Materials for Strong Light-Matter Interactions," *ACS Photonics*, vol. 5, no. 1, pp. 24–42, 2018. DOI: 10.1021/acsphotonics.7b00674.

[139] L. Sortino *et al.*, "Enhanced light-matter interaction in an atomically thin semiconductor coupled with dielectric nano-antennas," *Nature Communications*, vol. 10, no. 1, 2019. DOI: 10.1038/s41467-019-12963-3.

[140] M. Amani *et al.*, "Near-unity photoluminescence quantum yield in MoS2," *Science*, vol. 350, no. 6264, pp. 1065–1068, Nov. 2015. DOI: 10.1126/science.aad2114.

[141] A. F. Koenderink, "Single-Photon Nanoantennas," *ACS Photonics*, vol. 4, no. 4, pp. 710–722, 2017. DOI: 10.1021/acsphotonics.7b00061.

[142] J. Liu *et al.*, "A solid-state source of strongly entangled photon pairs with high brightness and indistinguishability," *Nature Nanotechnology*, vol. 14, no. 6, pp. 586–593, 2019. DOI: 10.1038/s41565-019-0435-9.

[143] M. Moczaa-Dusanowska *et al.*, "Strain-Tunable Single-Photon Source Based on a Circular Bragg Grating Cavity with Embedded Quantum Dots," *ACS Photonics*, 2020. DOI: 10.1021/acsphotonics.0c01465.

[144] S. Adachi, "Optical dispersion relations for GaP, GaAs, GaSb, InP, InAs, InSb, AlxGa1xAs, and In1xGaxAsyP1-y," *Journal of Applied Physics*, 1998. DOI: 10.1063/1.343580.

[145] S. A. Tawfik *et al.*, "First-principles investigation of quantum emission from hBN defects," *Nanoscale*, vol. 9, no. 36, pp. 13 575–13 582, Sep. 2017. DOI: 10.1039/c7nr04270a.

[146] S. Gao, H. Y. Chen, and M. Bernardi, "Radiative properties of quantum emitters in boron nitride from excited state calculations and Bayesian analysis," *npj Computational Materials*, vol. 7, no. 1, Dec. 2021. DOI: 10.1038/s41524-021-00544-2.

[147] I. Zhigulin *et al.*, "Stark effect of quantum blue emitters in hBN," *arxiv*, vol. 1, pp. 1–6, 2022.

[148] S. Jung *et al.*, "Vibrational Properties of h-BN and h-BN-Graphene Heterostructures Probed by Inelastic Electron Tunneling Spectroscopy," *Scientific Reports*, vol. 5, Nov. 2015. DOI: 10.1038/srep16642.

[149] P. Khatri, R. N. Edward Malein, A. J. Ramsay, and I. J. Luxmoore, "Stimulated Emission Depletion Microscopy with Color Centers in Hexagonal Boron Nitride," *ACS Photonics*, vol. 8, no. 7, pp. 2081–2087, 2021. DOI: 10.1021/acsphotonics.1c00423.

[150] S. Kumar, A. Kaczmarczyk, and B. D. Gerardot, "Strain-Induced Spatial and Spectral Isolation of Quantum Emitters in Mono- and Bilayer WSe2," *Nano Letters*, vol. 15, no. 11, pp. 7567–7573, 2015. DOI: 10.1021/acs.nanolett.5b03312.

[151] C. Palacios-Berraquero *et al.*, "Large-scale quantum-emitter arrays in atomically thin semiconductors," *Nature Communications*, vol. 8, May 2017. DOI: 10.1038/ncomms15093.

[152] T. Lu, J. Ku, S. Dietel, R. Staacke, and J. Meijer, "Charge-State Tuning of Single SnV Centers in Diamond," *ACS Photonics*, 2020. DOI: 10.1021/acsphotonics.0c01123.

[153] D. M. Lukin, M. A. Guidry, and J. Vučković, "Integrated quantum photonics with silicon carbide: challenges and prospects," *PRX QUANTUM*, vol. 020102, pp. 1–19, 2020. DOI: 10.1103/PRXQuantum.1.020102.

[154] T. Tashima, H. Takashima, A. W. Schell, T. T. Tran, I. Aharonovich, and S. Takeuchi, "Hybrid device of hexagonal boron nitride nanoflakes with defect centres and a nano-fibre Bragg cavity," *Scientific Reports*, vol. 12, no. 1, pp. 1–7, 2022. DOI: 10.1038/s41598-021-03703-z.

[155] J. E. Fröch *et al.*, "Purcell enhancement of a cavity-coupled emitter in hexagonal boron nitride," *arxiv*, 2021.

[156] Roushdey Salh, "Defect Related Luminescence in Silicon Dioxide Network: A Review," *Intech*, 2016. DOI: http://dx.doi.org/10.5772/57353.

[157] A. Dietrich *et al.*, "Observation of Fourier transform limited lines in hexagonal boron nitride," *Physical Review B*, vol. 98, no. 8, pp. 2–6, 2018. DOI: 10.1103/PhysRevB.98.081414.

[158] A. L. Exarhos, D. A. Hopper, R. N. Patel, M. W. Doherty, and L. C. Bassett, "Magnetic-field-dependent quantum emission in hexagonal boron nitride at room temperature," *Nature Communications*, vol. 10, no. 1, pp. 1–8, 2019. DOI: 10.1038/s41467-018-08185-8.

[159] H. L. Stern *et al.*, "Room-temperature optically detected magnetic resonance of single defects in hexagonal boron nitride," *Nature Communications*, no. 2022, pp. 1–9, 2022. DOI: 10.1038/s41467-022-28169-z.

[160] N. Mathur *et al.*, "Excited-state spin-resonance spectroscopy of VB- defect centers in hexagonal boron nitride," *Nature Communications*, pp. 1–7, 2022. DOI: 10.1038/s41467-022-30772-z.

[161] A. Gottscholl *et al.*, "Spin defects in hBN as promising temperature, pressure and magnetic field quantum sensors," *Nature Communications*, vol. 12, no. 1, pp. 6–13, 2021. DOI: 10.1038/s41467-021-24725-1.

[162] P. Yu *et al.*, "Excited-state spectroscopy of spin defects in hexagonal boron nitride," *arxiv*, pp. 2–5, 2021.

[163] D. Simin *et al.*, "All-optical dc nanotesla magnetometry using silicon vacancy fine structure in isotopically purified silicon carbide," *Physical Review X*, vol. 6, no. 3, pp. 1–12, 2016. DOI: 10.1103/PhysRevX.6.031014.

[164] D. A. Broadway *et al.*, "Anticrossing Spin Dynamics of Diamond Nitrogen-Vacancy Centers and All-Optical Low-Frequency Magnetometry," *Physical Review Applied*, vol. 6, no. 6, pp. 1–11, 2016. DOI: 10.1103/PhysRevApplied.6.064001.

[165] J. Chen, O. Y. Chen, and H. C. Chang, "Relaxation of a dense ensemble of spins in diamond under a continuous microwave driving field," *Scientific Reports*, vol. 11, no. 1, pp. 1–12, 2021. DOI: 10.1038/s41598-021-95722-z.

[166] L. Busaite, R. Lazda, A. Berzins, M. Auzinsh, R. Ferber, and F. Gahbauer, "Dynamic N14 nuclear spin polarization in nitrogen-vacancy centers in diamond," *Physical Review B*, vol. 102, no. 22, pp. 1–8, 2020. DOI: 10.1103/PhysRevB.102.224101.

[167] C. W. Huang and X. Hu, "Theoretical study of nuclear spin polarization and depolarization in self-assembled quantum dots," *Physical Review B*, vol. 81, no. 20, pp. 1–13, 2010. DOI: 10.1103/PhysRevB.81.205304.

[168] D. Kienzler, V. Negnevitsky, C. Fl¨uhmann, M. Marinelli, and J. P. Home, "Quantum harmonic oscillator state control in a squeezed Fock basis," *arxiv*, pp. 1–7, 2017.

[169] A. Högele *et al.*, "Dynamic nuclear spin polarization in the resonant laser excitation of an InGaAs quantum dot," *Physical Review Letters*, vol. 108, no. 19, pp. 1–5, 2012. DOI: 10.1103/PhysRevLett.108.197403.

[170] D. A. Gangloff *et al.*, "Quantum interface of an electron and a nuclear ensemble," *Science*, 2019. DOI: 10.1126/science.aaw2906.

[171] J. Yoneda *et al.*, "Fast Electrical Control of Single Electron Spins in Quantum Dots with Vanishing Influence from Nuclear Spins," *arxiv*, 2014.

[172] K. Takeda *et al.*, "A fault-tolerant addressable spin qubit in a natural silicon quantum dot," *Science Advances*, vol. 2, no. 8, pp. 1–7, 2016. DOI: 10.1126/sciadv.1600694.

[173] J. Yoneda *et al.*, "A quantum-dot spin qubit with coherence limited by charge noise and fidelity higher than 99.9 %," *Nature Nanotechnology*, vol. 13, no. February, pp. 9–14, 2018. DOI: 10.1038/s41565-017-0014-x.

[174] J. H. Bodey *et al.*, "Optical spin locking of a solid-state qubit," *npj Quantum Information*, vol. 5, no. 1, pp. 1–6, 2019. DOI: 10.1038/s41534-019-0206-3.

[175] A. Haykal *et al.*, "Decoherence of VB- spin defects in monoisotopic hexagonal boron nitride," *Nature Communications*, pp. 1–7, 2022. DOI: 10.1038/s41467-022-31743-0.

[176] R. Hanson, F. M. Mendoza, R. J. Epstein, and D. D. Awschalom, "Polarization and readout of coupled single spins in diamond," *Physical Review Letters*, vol. 97, no. 8, pp. 1–4, 2006. DOI: 10.1103/PhysRevLett.97.087601.

[177] S. V. Anishchik and K. L. Ivanov, "Sensitive detection of level anticrossing spectra of nitrogen vacancy centers in diamond," *Physical Review B*, vol. 96, no. 11, pp. 1–10, 2017. DOI: 10.1103/PhysRevB.96.115142.

[178] N. J. Guo *et al.*, "Generation of Spin Defects by Ion Implantation in Hexagonal Boron Nitride," *ACS Omega*, vol. 7, no. 2, pp. 1733–1739, Jan. 2022. DOI: 10.1021/acsomega.1c04564.

[179] G. Wolfowicz *et al.*, "Quantum guidelines for solid-state spin defects," *Nature Reviews Materials*, vol. 0123456789, 2021. DOI: 10.1038/s41578-021-00306-y.

[180] A. Schweiger and G. Jeschke, *Principles of Pulse Electron Paramagnetic Resonance*. Oxford University Press, 2005, ISBN: 978-0198506348.

[181] Y. Chen and S. Y. Quek, "Photophysical Characteristics of Boron Vacancy-Derived Defect Centers in Hexagonal Boron Nitride," *Journal of Physical Chemistry C*, vol. 125, no. 39, pp. 21 791–21 802, 2021. DOI: 10.1021/acs.jpcc.1c07729.

[182] I. Lovchinsky *et al.*, "Magnetic resonance spectroscopy of an atomically thin material using a single-spin qubit," *Science*, vol. 355, no. 6324, pp. 503–507, 2017. DOI: 10.1126/science.aal2538.

[183] V. Ivády *et al.*, "Photoluminescence at the ground-state level anticrossing of the nitrogen-vacancy center in diamond: A comprehensive study," *Physical Review B*, vol. 103, no. 3, pp. 1–13, 2021. DOI: 10.1103/PhysRevB.103.035307.

[184] M. H. Levitt, *Spin dynamics: Basics of nuclear magnetic resonance*. John Wiley & Sons, 2009, ISBN: 978-1-118-68184-8.

[185] L. I. Childress *et al.*, "Coherent dynamics of coupled electron and nuclear spin qubits in diamond," *Science*, vol. 314, no. 5797, pp. 281–285, 2006. DOI: 10.1126/science.1131871.

[186] E. L. Hahn, "Spin echoes," *Phys Rev Lett*, vol. 80, no. 4, pp. 580–594, 1950. DOI: 10.1103/PhysRev.80.580.

[187] B. Herzog and E. L. Hahn, "Transient nuclear induction and double nuclear resonance in solids," *Physical Review*, vol. 103, no. 1, pp. 148–166, 1956. DOI: 10.1103/PhysRev.103.148.

[188] R. Rubinas *et al.*, "Spin properties of NV centers in high-pressure, high-temperature grown diamond," *Journal of Physics Communications*, vol. 2, no. 11, 2018. DOI: 10.1088/2399-6528/aae992.

[189] F. Reinhard *et al.*, "Tuning a spin bath through the quantum-classical transition," *Physical Review Letters*, vol. 108, no. 20, pp. 1–5, 2012. DOI: 10.1103/PhysRevLett.108.200402.

[190] D. A. Bykov and L. L. Doskolovich, "Spatiotemporal coupled-mode theory of guided-mode resonant gratings," *Optics Express*, vol. 23, no. 15, p. 19 234, 2015. DOI: 10.1364/oe.23.019234.

[191] X. Wang *et al.*, "Precise control of the coupling coefficient through destructive interference in silicon waveguide Bragg gratings," *Optics Letters*, vol. 39, no. 19, p. 5519, 2014. DOI: 10.1364/ol.39.005519.

[192] D. G. Baranov *et al.*, "All-dielectric nanophotonics: the quest for better materials and fabrication techniques," *Optica*, vol. 4, no. 7, p. 814, 2017. DOI: 10.1364/optica.4.000814.

[193] B. Hillebrands and K. Ounadjela, *Spin Dynamics in Confined Magnetic Structures II*. 2003, ISBN: 3540440844. DOI: 10.1007/b12462.

[194] B. Hillebrands and K. Ounadjela, *Spin Dynamics in Confined Magnetic structure I*. Springer, 2002, ISBN: 3540411917. DOI: 10.1007/3-540-40907-6.

[195] T. L. Gilbert, "A phenomenological theory of damping in ferromagnetic materials," *IEEE Transactions on Magnetics*, vol. 40, no. 6, pp. 3443–3449, 2004. DOI: 10.1109/TMAG.2004.836740.

[196] M. Lakshmanan, "The fascinating world of the Landau-Lifshitz-Gilbert equation: An overview," *Philosophical Transactions of the Royal Society A*, vol. 369, no. 1939, pp. 1280–1300, 2011. DOI: 10.1098/rsta.2010.0319.

[197] F. Bloch, "Nuclear induction," *Physical Review*, vol. 70, no. 7-8, pp. 460–474, 1946. DOI: 10.1103/PhysRev.70.460.

[198] O. Yalçın, "Ferromagnetic Resonance," *Intech*, p. 13, 2013. DOI: 10.5772/56134.

[199] N. Bloembergen, "On the ferromagnetic resonance in nickel and supermalloy," *Physical Review*, vol. 78, no. 5, pp. 572–580, 1950. DOI: 10.1103/PhysRev.78.572.

[200] A. G. Flores, L. Torres, V. Raposo, L. López-Díaz, M. Zazo, and J. Iñiguez, "Analysis of the theoretical expressions used for the computation of the ferromagnetic resonance linewidths in ferrites," *Physica Status Solidi (A) Applied Research*, vol. 171, no. 2, pp. 549–553, 1999. DOI: 10.1002/(SICI)1521-396X(199902)171:2<549::AID-PSSA549>3.0.CO;2-4.

[201] M. P. Williamson, "Drawing single NMR spins and understanding relaxation," *Natural Product Communications*, vol. 14, no. 5, 2019. DOI: 10.1177/1934578X19849790.

[202] P. W. Millonni and J. H. Eberly, *Laser Physics*. 2010, ISBN: 9780470409718. DOI: 10.1002/9780470409718.

[203] C. Cohen-Tannoudji and D. Guéry-Odelin, *Advances in Atomic Physics*. 2011. DOI: 10.1142/9789812774989.

[204] F. H. L. Koppens *et al.*, "Driven coherent oscillations of a single electron spin in a quantum dot," *Nature*, vol. 442, no. August, 2006. DOI: 10.1038/nature05065.